POLITECNICO DI TORINO

Collegio di Ingegneria Chimica e dei Materiali

Master of Science Course
in Materials Engineering

Master of Science Thesis

Influence of Directed Energy Deposition (DED) parameters on microstructural features of AISI 316L steel

Tutors

Prof. Daniele Ugues
Prof.ssa Mariangela Lombardi

Candidate

Arianna Gennari

December 2017

A GAIA,
motore di ogni mio successo,
passato, presente e futuro.

Sommario

Introduzione

Le tecnologie di produzione additiva (Additive Manufacturing – AM) possono essere definite come quei processi tecnologici, aventi lo scopo di produrre componenti mediante sovrapposizione di strati, a partire da file CAD 3D, in opposizione alle tecniche di produzione sottrattiva. Da un punto di vista tecnologico, non si tratta di un'innovazione recente (la "stampa 3D" si utilizza da metà anni '80 dello scorso secolo come prototipazione rapida), ma negli ultimi decenni le opportunità di utilizzo di questa tecnologia si sono ampliate notevolmente grazie alla possibilità di realizzare oggetti di maggiori dimensioni, in una gamma assai più ampia di materiali (metalli, ceramici, polimeri, materiali compositi, ecc.) e con tempi di produzione decisamente ridotti. Due caratteristiche della produzione additiva risultano essere centrali per comprenderne le potenzialità di sviluppo:

1) consentire la produzione di oggetti con geometrie complesse non altrimenti realizzabili in un pezzo unico con tecniche tradizionali, con un minore impiego di materie prime, maggiori prestazioni ed utilizzando eventualmente materiali diversi;
2) far sì che i costi di realizzazione di varianti rispetto ad un modello base siano sostanzialmente nulli, conferendo così grande flessibilità e versatilità al processo.

Nell'ambito della produzione additiva di materiali metallici, la presente tesi si è concentrata su uno dei processi più conosciuti e affermati è la tecnica *Directed Energy Deposition* (DED). Questo processo prevede la deposizione di polvere metallica su un substrato mobile attraverso un ugello e la sua simultanea fusione tramite un fascio laser focalizzato, in modo tale da realizzare un legame metallurgico tra i vari strati di materiale. Quando le polveri sono depositate, il fascio laser fornisce un'energia termica sufficiente per fondere le particelle, creando così una pozza di metallo fuso (melt pool). Una volta completata la deposizione del primo strato, il substrato si muove verso la testa di deposizione per mezzo di una macchina a controllo numerico (CNC) e il processo si ripete.

Il presente lavoro di tesi si propone in particolare di valutare l'influenza che i parametri del processo DED hanno sulle caratteristiche microstrutturali di campioni in acciaio inossidabile AISI 316L realizzati con tale tecnica. In particolare, l'attenzione è stata rivolta all'analisi della microstruttura e della geometria, alla valutazione degli effetti termici su di esse e allo studio del comportamento meccanico in termini di micro- e nano-durezza. Inoltre, le analisi sono state condotte non solo sui campioni, ma anche sulle polveri metalliche nuove e su quelle residue da un ciclo DED. In questo modo è stato possibile valutare se queste ultime presentassero ancora caratteristiche microstrutturali e composizionali idonee per essere utilizzate per un nuovo processo additivo.

Le analisi effettuate in questo lavoro sono parte di un progetto Europeo chiamato *Borealis,* coordinato da Prima Industrie in collaborazione con un ampio gruppo di aziende. Il progetto si propone di combinare diverse tecnologie additive e sottrattive basate su laser in una singola macchina per fornire prodotti "net-shape" attraverso un processo costituito da un'unica fase di lavoro, caratterizzata da un'efficienza di utilizzo dei materiali e un'efficienza energetica senza precedenti. La macchina sarà dotata di un'innovativa testa flessibile a revolver che consentirà di miscelare più polveri di diversi materiali e con diverse dimensioni di particelle (micro e nano polveri). In questo modo, Borealis consentirà l'integrazione di più tecnologie additive in un'unica macchina, per combinare l'alternativa più produttiva con quella più precisa con zero tempi di set-up e zero spreco di materiale.

Le polveri di acciaio inossidabile AISI 316L, la cui composizione chimica è riportata in Tabella 1, utilizzate per la realizzazione dei campioni, sono state ottenute attraverso un processo di atomizzazione in gas e fornite da LPW Technology Ltd. La Figura 1 mostra le micrografie SEM della polvere a diversi

ingrandimenti. Come mostra la Figura 1, le particelle presentano una forma approssimativamente sferica, con qualche satellite sulla superficie.

Tabella 1: Composizione chimica della polvere di AISI 316L.

Element	C	Cr	Cu	Fe	Mn	Mo	Ni	P	S	Si
wt %	< 0.03	17.5 – 18.0	< 0.50	Bal.	< 2.0	2.25 – 2.50	12.5 – 13.0	< 0.025	< 0.01	< 0.75

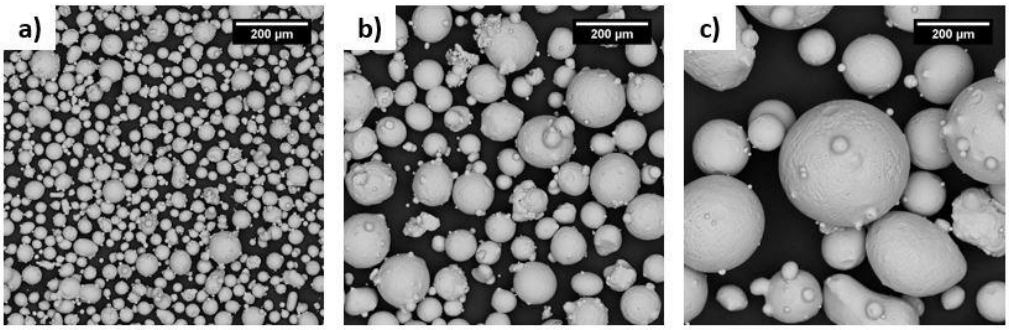

Figura 1: Micrografie SEM della polvere di AISI 316L a) 300 X, b) 800 X e c) 2000 X.

I campioni in acciaio inossidabile AISI 316L analizzati in questo lavoro di tesi sono stati realizzati nel laboratorio (ARM lab – DTI) di SUPSI (Scuola Universitaria Professionale della Svizzera Italiana) con un sistema Laserdyne 430. È stata utilizzata una sorgente laser Convergent Photonics CF1000 con una potenza massima di 1000 W e una lunghezza d'onda di 1070 nm. La testa di deposizione è una Optomec con 4 ugelli. Anche l'alimentatore di polvere utilizzato è prodotto dalla Optomec. Tutti i campioni sono stati fabbricati utilizzando Argon di purezza 4.6 come gas protettivo e di trasporto, con un flusso di trasporto di massa di 4 l/min.

I campioni sono stati realizzati su piattaforme rettangolari di AISI 316L di dimensioni 150x80x8 mm e presentano due geometrie differenti:

- cerchi: cerchi concentrici con un diametro di 3, 9 e 15 mm (larghezza e altezza variabili) su Piattaforme 5 e 6 (Figura 2).
- spirali: cerchi concentrici con diverse percentuali di overlap: 30, 50 e 70 % (larghezza e altezza variabili) su Piattaforma 3 e 4 (Figura 3).

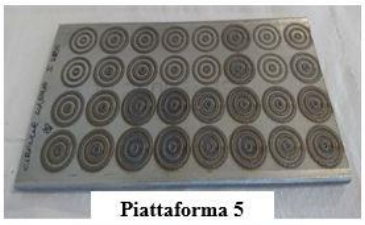

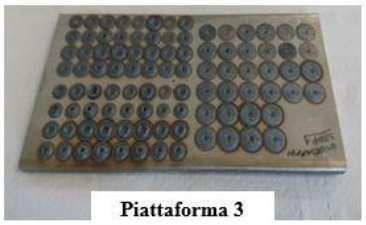

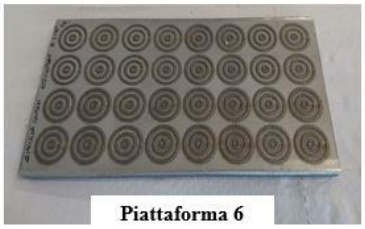

Figura 2: Piattaforme 5 e 6 con cerchi. **Figura 3:** Piattaforme 3 e 4 con spirali.

Per quanto riguarda le spirali, sono stati realizzati cinque cerchi concentrici variando la potenza (*P),* la velocità (*F*), la percentuale di overlap e la strategia di scanning, mentre nel caso dei cerchi, sono stati ottenuti tre cerchi concentrici non sovrapposti con potenze, velocità e strategie diverse. In particolare, la strategia S1 prevede la realizzazione dello scan interno per poi muoversi verso quello esterno, mentre la strategia S2 parte dal cerchio esterno e si muove verso quello interno. Tra tutti i campioni presenti sulle piattaforme, sono stati selezionati quelli che presentano le combinazioni dei parametri di processo più adatte a valutare l'effetto dell'accumulo di calore e la relazione tra i parametri di processo e la microstruttura ottenuta. I parametri di processo utilizzati per la realizzazione dei campioni selezionati sono riportati in Tabella 2 e 3, per i cerchi e le spirali, rispettivamente.

Tabella 2: Parametri di processo utilizzati per i cerchi.

n.	P [W]	F [mm/min]	G [g/s]	Strategy
P5_1	300	450	0.0415	S1
P5_2	300	450	0.0415	S2
P5_3	600	450	0.0415	S1
P5_4	600	450	0.0415	S2
P6_1	150	200	0.0415	S1
P6_2	150	200	0.0415	S2
P6_3	350	500	0.0415	S1
P6_4	350	500	0.0415	S2

Tabella 3: Parametri di processo utilizzati per le spirali.

n.	P [W]	F [mm/min]	G [g/s]	Strategy	Overlap
P3_1	300	450	0.0415	S1	50 %
P3_2	300	450	0.0415	S2	50 %
P3_3	600	450	0.0415	S1	50 %
P3_4	600	450	0.0415	S2	50 %
P3_5	300	450	0.0415	S1	70 %
P3_6	300	450	0.0415	S2	70 %
P3_7	600	450	0.0415	S1	70 %
P3_8	600	450	0.0415	S2	70 %
P4_1	300	450	0.0415	S1	30 %
P4_2	300	450	0.0415	S2	30 %
P4_3	600	450	0.0415	S1	30 %
P4_4	600	450	0.0415	S2	30 %
P4_5	150	200	0.0415	S1	30 %
P4_6	150	200	0.0415	S2	30 %
P4_7	350	500	0.0415	S1	30 %
P4_8	350	500	0.0415	S2	30 %

Per analizzarne la microstruttura, i campioni sono stati tagliati lungo il piano XZ e sono stati inglobati usando la resina ClaroCit e lucidati fino ad 1 µm. Successivamente sono stati attaccati chimicamente con diversi reagenti in modo da individuare il reagente chimico che evidenziasse al meglio la microstruttura. Sono stati utilizzati i seguenti reagenti:

- Aqua regia (15 ml HCl, 5 ml HNO_3, 100 ml H_2O), immersione per 60 s e 120 s;
- Aqua regia modificata (HCl, HNO_3, CH_3COOH), immersione per 5 s, goccia per 10 s, tampone per 10 s;

- Attacco elettrolitico (H_3PO_4, 6V);
- Kalling No.2 (HCl, $CuCl_2$, CH_3CH_2OH).

Dopo diversi tentativi, il Kalling No.2 è stato scelto come reagente chimico per attaccare le polveri di 316L e i campioni con tempi di immersione di 10 e 15 secondi, rispettivamente.

Il software Image J è stato utilizzato per calcolare la porosità delle polveri, la distribuzione granulometrica delle particelle di polvere nuova e usata mediante il metodo di analisi di immagine e le grandezze geometriche dei melt pool dei campioni.

In questo lavoro sono state utilizzate due tipologie di microscopi:

- Microscopio Ottico Leica DMI 500, per analizzare le sezioni delle polveri nuove ed usate, la dimensione e la geometria dei melt pool dei campioni e l'effetto dell'attacco chimico sulla microstruttura;
- Microscopio Elettronico a Scansione (SEM) Phenon XL equipaggiato con una spettroscopia dispersiva elettronica (EDS) completamente integrata, per analizzare la microstruttura della polvere e dei campioni e la loro composizione chimica tramite EDS.

Le analisi di diffrazione di Raggi X (XRD) sono state eseguite sulla polvere nuova ed usata utilizzando il sistema PANalytical Xpert^3 in una configurazione Bragg Brentano in un intervallo 2θ tra 20 e 100° (operando a 40 kV e 40 mA con un intervallo di 0.013° e 30 s per intervallo).

Per quanto riguarda le prove meccaniche, la microdurezza Vickers è stata misurata per mezzo dell'indentatore micro-Vickers Leica VMHT con un carico di 100 gf applicato per 15 s. Le misure sono state effettuate sulla sezione dei campioni inglobati nella resina a freddo, concentrandosi sull'area del melt pool e realizzando le indentazioni lungo gli assi X e Z della sezione. Le impronte Vickers sono state poi misurate utilizzando il software Image J.

Infine, il nanoindentatore TI950 Nanoindenter (Hysitron) è stato utilizzato per analizzare la durezza dei campioni su scala nanometrica. Per il test sono state impiegate una punta diamantata Berkovich e un carico controllato di 2500 μN e l'analisi è stata condotta applicando e rimuovendo il carico dai campioni. In questo modo è stata realizzata una griglia 11 x 11 con una distanza di 10 μm tra un'impronta e l'altra in diverse zone del melt pool dello scan del campione.

Risultati

Per quanto riguarda le polveri, l'obiettivo principale è stato quello di verificare se la polvere di AISI 316L residua dopo l'esecuzione di un ciclo DED conservasse o meno ancora la morfologia, le proprietà microstrutturali, composizionali e meccaniche e, quindi, potesse essere riutilizzata per un nuovo processo additivo. Per questo motivo entrambe le polveri, nuova ed usata, sono state sottoposte ad analisi al fine di confrontarne le caratteristiche.

Inizialmente le polveri sono state osservate al SEM a diversi ingrandimenti (Figura 4 e 5). Come illustrato in Figura 4, le particelle di polvere nuova presentano una forma sferica e satelliti in superficie, mentre nella polvere usata la maggior parte delle particelle ha una forma irregolare in quanto, dopo esser state fuse durante il processo DED, esse tendono a rifondere insieme assumendo una forma irregolare (Figura 5). Inoltre, da queste micrografie si può notare che nella polvere usata non è presente una grande quantità di particelle fini che, invece, sono caratteristiche della polvere nuova. Pertanto, si può affermare che la dimensione media delle particelle della polvere nuova è inferiore a quella delle particelle che hanno già subito il processo DED.

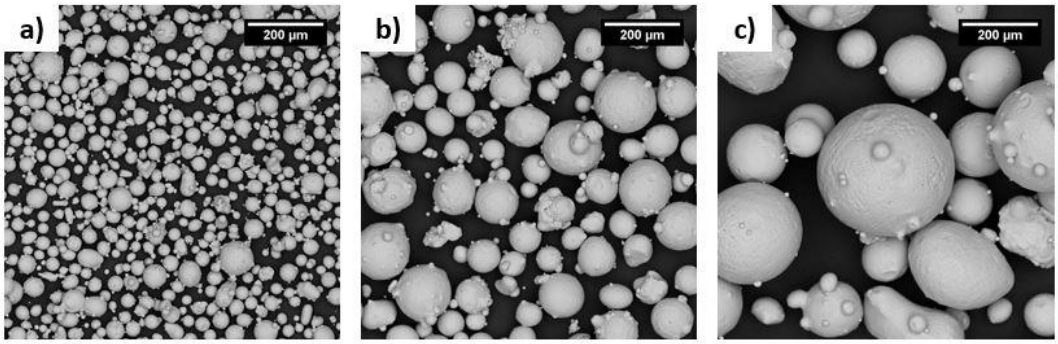

Figura 4: Micrografie SEM della polvere nuova di 316L a) 300 X, b) 800 X e c) 2000 X.

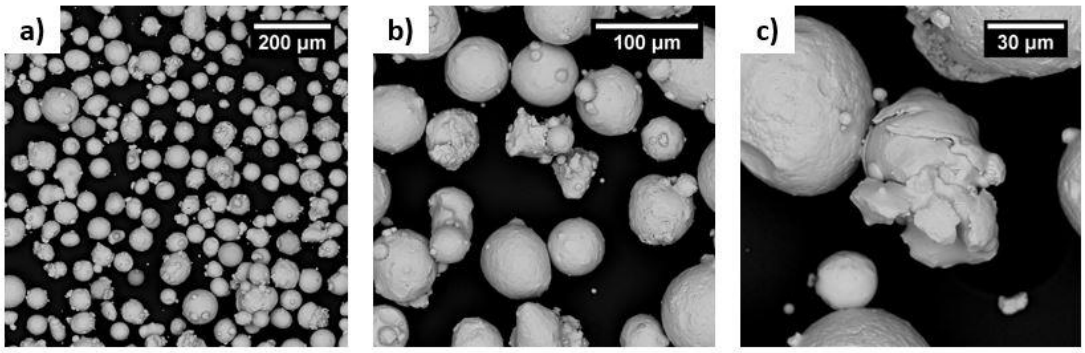

Figura 5: Micrografie SEM della polvere usata di 316L a) 300 X, b) 800 X e c) 2000 X.

Questa considerazione è stata confermata dal calcolo della distribuzione granulometrica delle particelle di entrambe le polveri attraverso il metodo di analisi d'immagine (in numero) e la tecnica di granulometria laser (in volume). La distribuzione granulometrica ottenuta con il metodo di analisi d'immagine è riportata in Figura 6 a). Come illustrato in Figura 6 a), questa analisi in numero fornisce una distribuzione della dimensione delle particelle in cui i diametri delle particelle di polvere nuova si trovano nell'intervallo 10-50 µm, mentre i diametri delle particelle di polvere usata hanno valori compresi tra i 30 e i 75 µm. Anche la granulometria laser conferma che la polvere usata presenta particelle di dimensioni maggiori. Infatti, come è illustrato in Figura 6 b), la distribuzione ottenuta con la tecnica laser è caratterizzata da un picco intorno ai 95 µm relativo alle particelle di polvere usata, mentre il picco riferito al diametro delle particelle di polvere nuova è spostato verso valori inferiori, intorno ai 45 µm. Inoltre la distribuzione delle polveri nuove risulta bimodale con un picco più pronunciato riferibile a particelle fini, mentre la polvere usata assume una distribuzione a unico picco spostato verso le particelle più grossolane.

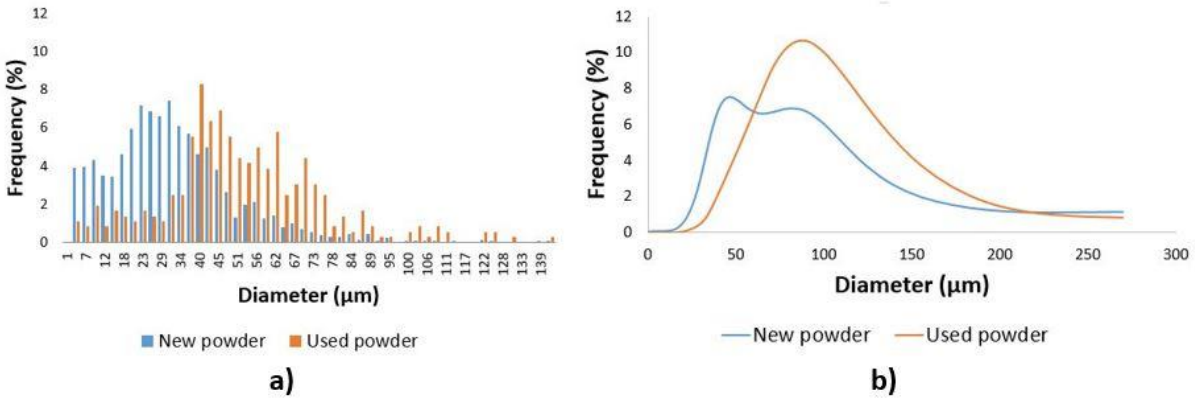

Figura 6: Distribuzione granulometrica ottenuta con a) il metodo di analisi di immagine (in volume) e b) la tecnica di granulometria laser (in volume).

Oltre alla dimensione delle particelle, un altro parametro che distingue la polvere nuova da quella usata è la porosità (calcolata tramite analisi di immagine delle micrografie dei campioni inglobati). Infatti, le particelle di polvere nuova presentano una porosità di circa 0.03 %, mentre le particelle residue dal processo DED hanno una porosità che è quasi dieci volte superiore di quella delle particelle di partenza, ossia 0.2 %. I pori sferici individuati nella polvere nuova sono stati causati da gas intrappolato durante il processo di atomizzazione, mentre la porosità della polvere usata è caratterizzata da grandi cavità di forma irregolare, dovute al processo DED, e ascrivibili a meccanismi di parziale fusione e risolidificazione con conseguenti ritiri e ulteriore intrappolamento di gas (Figura 7).

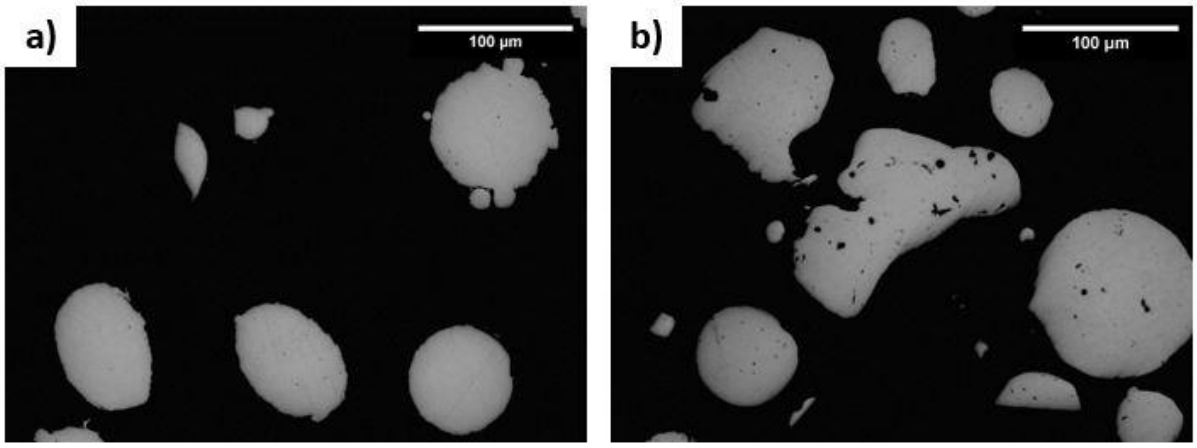

Figura 7: Micrografie OM della a) polvere nuova di 316L e della b) polvere usata di 316L a 200 X.

Dopo aver analizzato la forma, dimensione e porosità delle particelle, un'ulteriore differenza tra la polvere nuova e quella usata risiede nella microstruttura, in particolare nelle fasi presenti. Lo spettro XRD riportato in Figura 8 mostra che entrambe le polveri sono costituite principalmente da fase austenitica, ma la polvere usata presenta un picco aggiuntivo, caratteristico della delta ferrite. Questo risultato è stato confermato da diversi studi in letteratura sul 316L ottenuto da processi additivi [1]–[3] e dall'analisi del diagramma Schaeffler [2] in cui la composizione dell'acciaio in esame è collocata all'interno dell'area ferrite-austenite prevedendo un contenuto di fase ferritica compreso tra lo 0 e il 5 %wt.

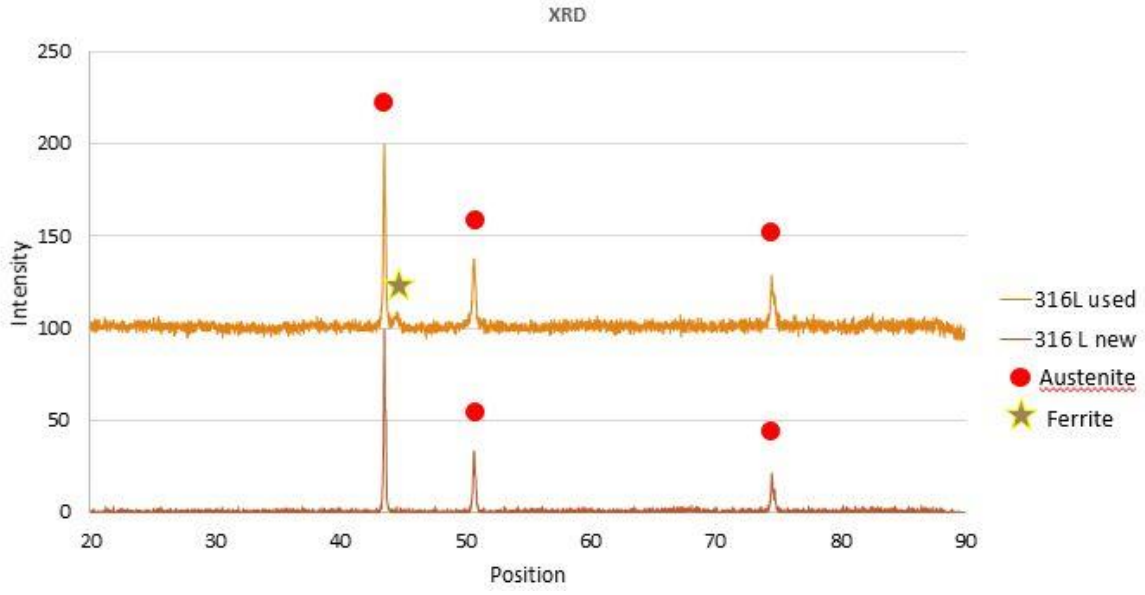

Figura 8: Spettro XRD della polvere nuova ed usata.

Analizzando la microstruttura di entrambe le polveri, sono state rilevati dei particolari sub-micrometrici dispersi sulla superficie delle particelle (Figura 9). Per individuare la natura composizionale di queste aree, sono state condotte delle analisi EDS puntuali, lineari e mappe EDS. È importante sottolineare che questa indagine è stata condotta solo sulle particelle di polvere usata, perché la polvere nuova non presentava una grande quantità di tali particolari. I risultati delle analisi EDS hanno rivelato che questi particolari sono ricchi in O, Mn e Si, mentre la quantità di Fe, Ni e Cr diminuisce (Figura 10). A seguito di queste analisi, tali particelle sono state identificate come ossidi degli elementi presenti in composizione, con la maggiore affinità con l'ossigeno. Poiché questi ossidi sono stati rilevati principalmente nelle particelle di polvere usata, la loro formazione potrebbe essere dovuta all'esposizione della polvere all'atmosfera del processo DED. Questo è credibile in quanto la camera del processo DED utilizzata per la fabbricazione dei campioni non presenta un'atmosfera controllata. Inoltre, come evidenziato nel risultato dell'analisi EDS di linea riportato in Figura 10, non tutti questi particolari circolari presentano la composizione sopra citata. Pertanto, alcune di queste aree che potrebbero sembrare costituite principalmente da O, Si e Mn da una prima osservazione al SEM, in realtà potrebbero essere dei micropori dovuti al distacco di ossido durante la preparazione del campione. Comunque la determinazione della natura e della causa di queste caratteristiche necessita ulteriori approfondimenti.

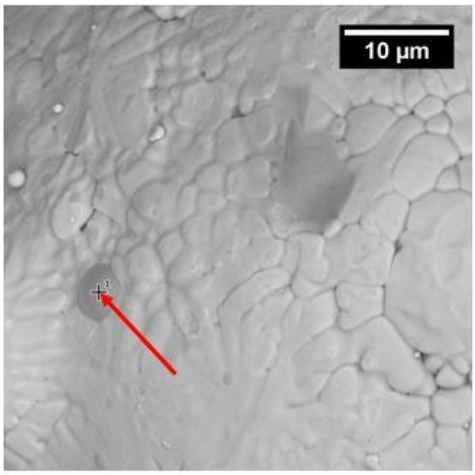

Figura 9: Micrografia SEM di una caratteristica submicrometrica sulla superficie di una particella di polvere usata.

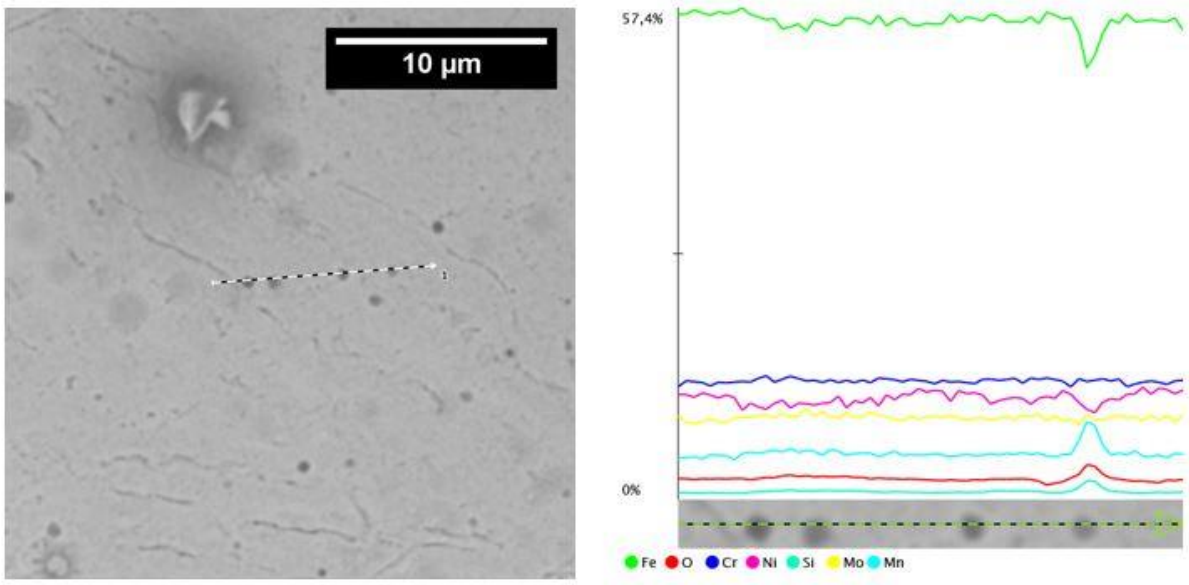

Figura 10: Analisi EDS di linea e concentrazione di Fe, O, Cr, Ni, Si, Mo e Mn.

La microstruttura delle polveri è stata meglio analizzata attaccando chimicamente le particelle con la soluzione Kalling No.2 con un'immersione di 10 secondi. Come illustrato in Figura 11 e 12, la microstruttura è fine in entrambe le polveri (nuova e usata) grazie all'elevata velocità di raffreddamento e non sono presenti disomogeneità all'interno della stessa particella, quindi non ci sono aree che presentano una microstruttura diversa. La Figura 12 a) mostra come alcune particelle di polvere usata siano state attaccate in maniera più aggressiva rispetto alla particelle che non hanno subito il processo DED. Per questo motivo, si può assumere che queste particelle avranno un diverso comportamento di fusione perché potrebbero aver perso degli elementi in lega o potrebbero essersi formati alcuni precipitati, che possono assorbire di più o di meno il fascio laser.

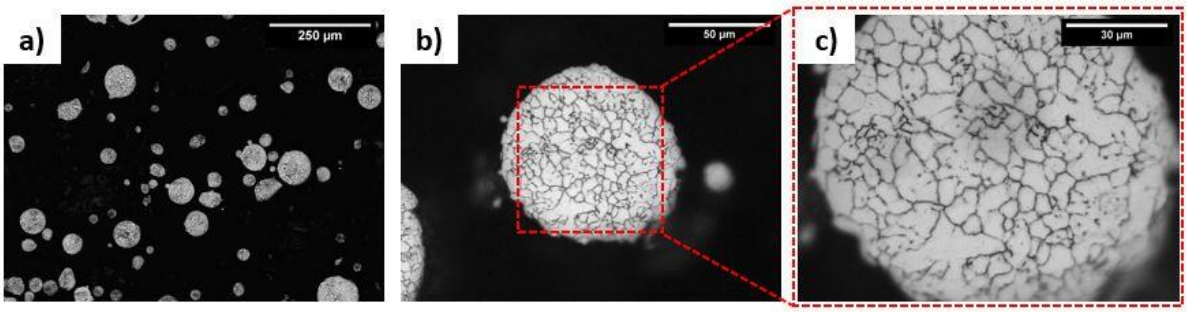

Figura 11: Micrografie OM di: a) polvere nuova attaccata chimicamente, 100 X, b) particella di polvere nuova attaccata, 500 X, c) dettaglio della microstruttura della particella attaccata, 1000 X.

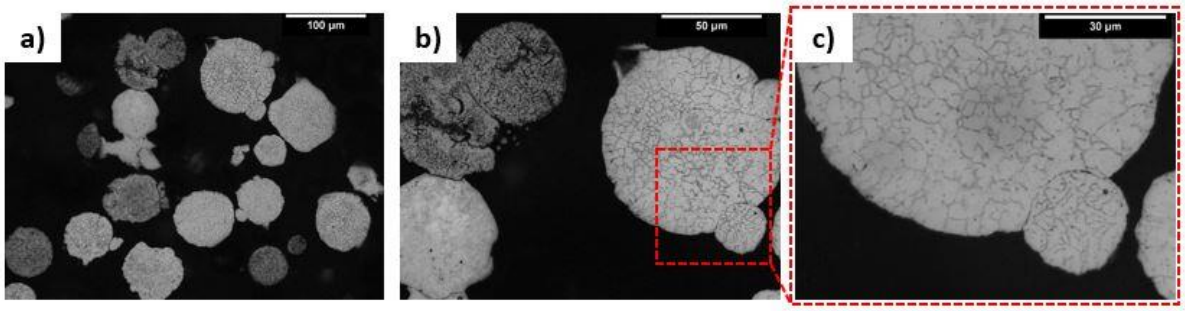

Figura 12: Micrografie OM di: a) polvere usata attaccata chimicamente, 100 X, b) particella di polvere usata attaccata, 500 X, c) dettaglio della microstruttura della particella attaccata, 1000 X.

Infine, per capire se le proprietà meccaniche fossero state influenzate dal processo DED, entrambe le polveri sono state sottoposte a prove di durezza Micro-Vickers, con un carico di 100 gf applicato per 15 s. Sono state realizzate misure di microdurezza su dieci particelle per entrambe le tipologie di polvere (Figura 13) e in seguito è stata calcolata una media del valore di microdurezza Vickers. Il valore medio di microdurezza Vickers della polvera nuova è 202 HV, che è circa il 15 % in più del valore di microdurezza Vickers della polvere usata (175 HV). Questo risultato conferma ancora una volta che la microstruttura delle particelle cambia dopo esser state sottoposte al processo DED e questo aspetto deve essere preso in attenta considerazione se la polvere che ha già subito un ciclo DED deve essere utilizzata per un nuovo processo additivo. Questo aspetto è particolarmente importante nella definizione del grado di maturazione della tecnologia di processo (Manufacturing Readiness Level, MRL), essenziale per pervenire alla certificazione del processo a livello industriale.

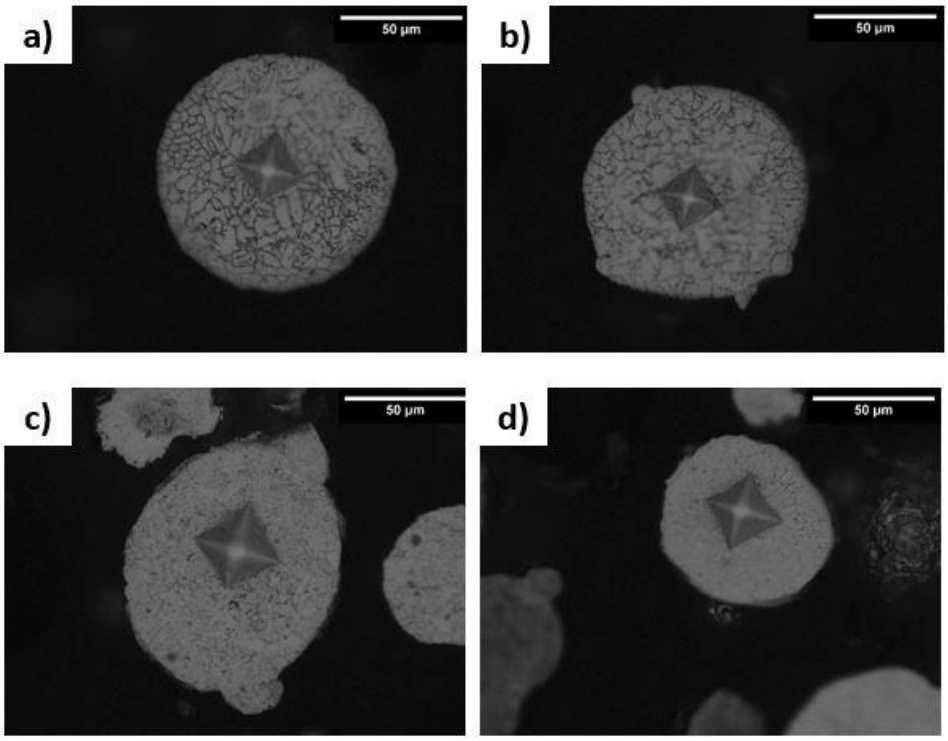

Figura 13: Micrografie OM delle indentazioni Micro-Vickers sulle particelle di polvere nuova, a) e b), a 500 X e sulle particelle di polvere usata, c) e d), a 500 X.

Una volta completata l'analisi sulle polveri, l'attenzione è stata rivolta allo studio dell'effetto dei parametri del processo DED, come potenza del laser e strategia di scansione, sulla microstruttura dell'acciaio AISI 316L fabbricato. Per questo motivo, i campioni selezionati sono stati sottoposti ad un attacco chimico per immersione di 15 s per mezzo della soluzione Kalling No.2 e poi osservati al microscopio ottico e al SEM.

La microstruttura dei campioni appare densa, priva di pori, cricche o particelle non fuse ed è caratterizzata dalla presenza di regioni con una microstruttura differente, dovute alla variazione della velocità di raffreddamento che si riscontra lungo il volume del melt pool. Nella parte superiore degli scan si osserva una struttura a grani fini (Figura 14 b)) in quanto, in questa area, la velocità di raffreddamento è particolarmente elevata a causa della sostanziale perdita di calore per radiazione/convezione. La velocità di raffreddamento minore si manifesta durante gli ultimi stadi del processo di solidificazione ed è concentrata nella parte centrale dello scan dove si osserva una microstruttura grossolana a grani equiassici (Figura 14 c)), causata da un importante accumulo di calore e quindi da una bassa velocità di solidificazione. Come illustrato in Figura 15, velocità di solidificazione relativamente basse portano ad avere una crescita di dendriti colonnari lungo l'intera lunghezza del perimetro del melt pool in tutti i campioni. Si può notare come la direzione di crescita delle dendriti sia dall'interfaccia con la piattaforma verso il centro del melt pool, a causa della direzione del flusso di calore durante il processo di solidificazione.

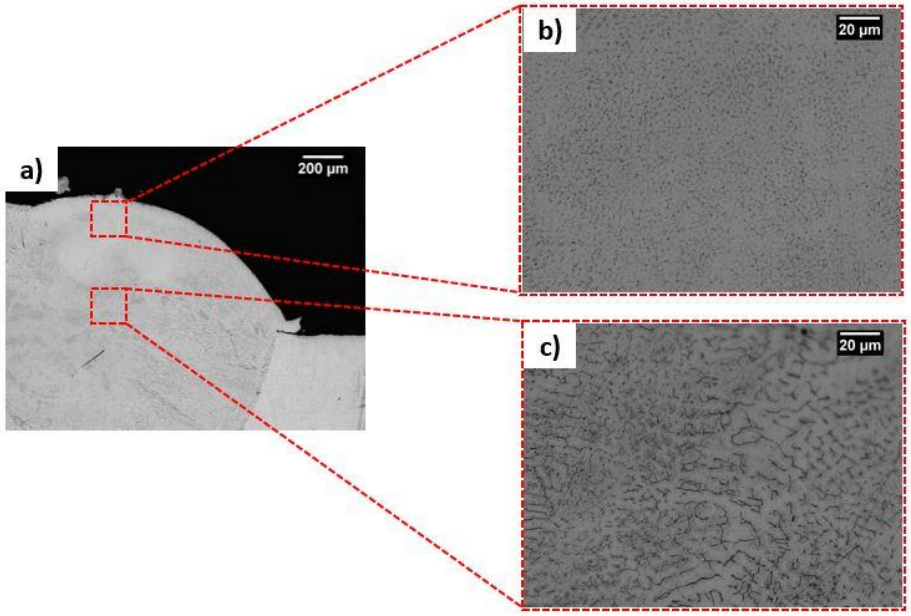

Figura 14: Micrografie OM: a) melt pool dello scan del campione P3_3, 50 X, b) dettaglio della microstruttura della regione superiore del melt pool, 500 X, c) dettaglio della microstruttura della regione centrale del melt pool, 500 X.

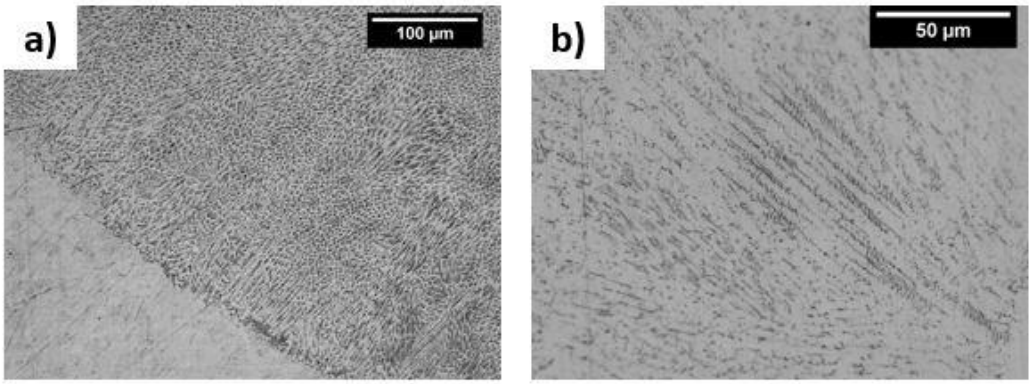

Figura 15: Micrografie OM della crescita colonnare delle dendriti: a) campione P3_7, 200 X, b) campione P3_6, 500 X.

Inoltre, come era già stato osservato durante le analisi effettuate sulle polveri, durante il processo DED solidificano le fasi austenitiche e ferritiche (Figura 16). La presenza di austenite e di ferrite nei campioni di AISI 316L ottenuto da processi additivi è stata confermata da diversi studi condotti negli ultimi decenni [2], [4], [5], in cui sono state identificate le strutture ferritiche e austenitiche sia nella zona centrale di saldature laser sia intorno alla linea di fusione.

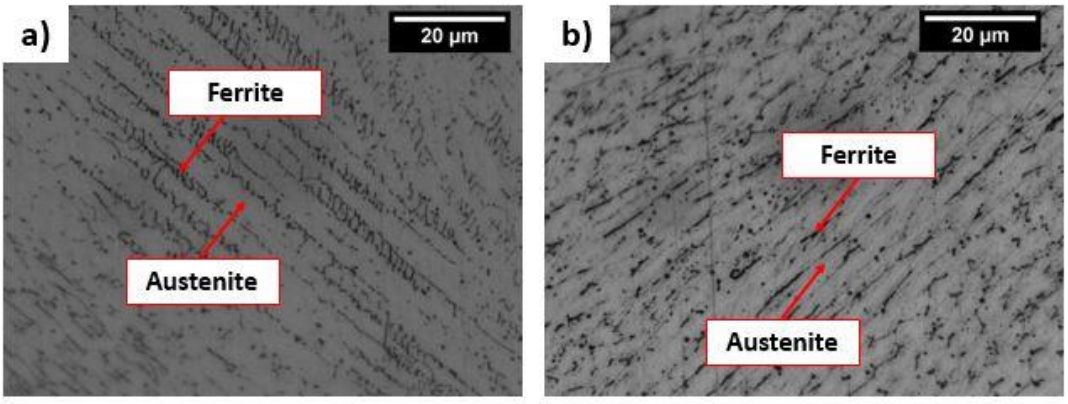

Figura 16: Microstruttura del melt pool vicino al perimetro: a) campione P3_3, 1000 X, b) campione P3_7, 1000 X.

Anche nei campioni realizzati tramite il processo DED sono stati rilevati i particolari sub-micrometrici dispersi all'interno del melt pool e presenti in tutti i campioni. Tali particolari sono stati oggetto di ulteriori analisi EDS e i risultati hanno confermato la loro composizione in O, Si e Mn, rivelandosi pertanto simili in termini di composizione chimica rispetto a quelli trovati nelle polveri analizzate in precedenza. Inoltre, esaminando la microstruttura dei campioni, in particolare la superficie, sono stati identificati ossidi di cromo la cui composizione è stata confermata dal risultato di un'analisi EDS riportata in Figura 17. Si può notare che nella regione superiore del campione, si può identificare uno strato ricco di Cr e O, ma povero di Fe e Ni. Ciò è dovuto al fatto che gli acciai inossidabili come il 316L contengono sufficiente cromo per subire passivazione a contatto con l'ossigeno, formando una pellicola di ossido di cromo sulla superficie. Questo strato previene l'ulteriore corrosione bloccando la diffusione dell'ossigeno sulla superficie dell'acciaio e impedendo al processo di corrosione di diffondersi nella massa del metallo. Allo stesso tempo, però, occorre segnalare che la formazione di questi strati di ossido rappresenta una discontinuità nel materiale, pertanto la loro presenza è prevedibile ma non auspicabile.

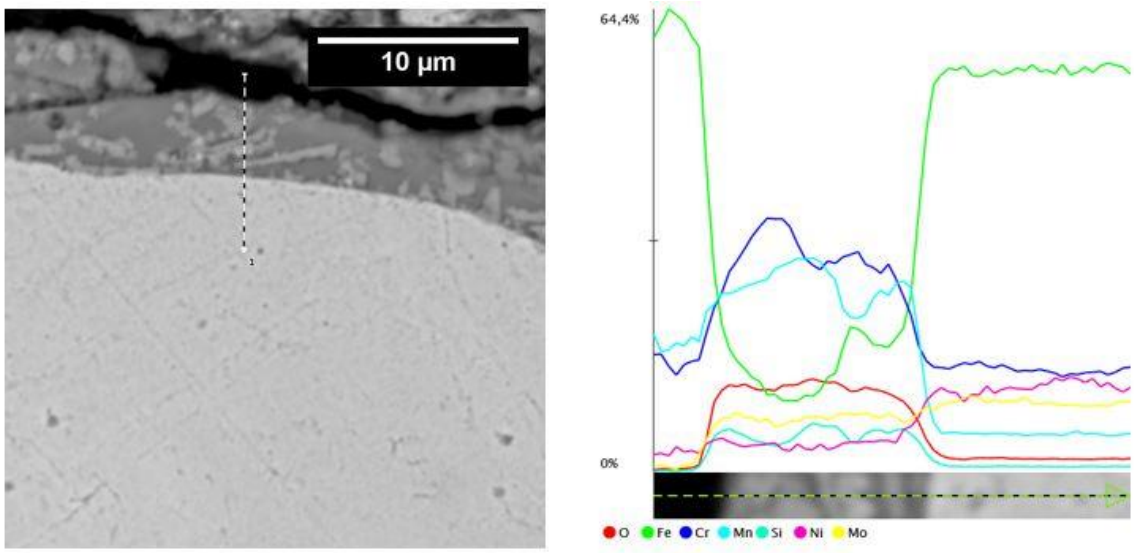

Figura 17: Analisi EDS lineare e concentrazione di O, Fe, Cr, Mn, Si, Ni e Mo.

L'effetto dei parametri di processo, come la potenza del laser e la strategia di scansione, sulla microstruttura dei campioni è stato studiato con riferimento alle spirali. In particolare, è stata analizzata la dimensione della spaziatura delle braccia dendritiche (DAS) e l'effetto della potenza e della strategia su di essa. Dall'analisi e dal calcolo del DAS eseguiti sui campioni P3_1, P3_2, P3_3 e P3_4, sono stati ottenuti i risultati riportati in Tabella 4. Come mostrato in Figura 18, con l'aumento della potenza del laser, le strutture dendritiche in prossimità del bordo del melt pool passano dall'essere sottili (con un valore medio di 2 µm per campioni realizzati con una potenza laser di 300 W) a grossolane (con un valore medio di 3 µm per campioni realizzati con una potenza laser di 600 W), il che significa che gradualmente aumenta il parametro DAS. Ciò è dovuto al fatto che l'elevata energia termica trasferita dal laser ad alta potenza al melt pool riduce la velocità di solidificazione delle singole strutture dendritiche, dando di conseguenza alle dendriti maggior tempo per crescere. Al contrario della potenza, che ha un effetto importante sulla microstruttura, la scelta di una strategia di scansione piuttosto che un'altra sembra non influenzare la dimensione del DAS.

Tabella 4: Misura della spaziatura delle braccia dendritiche (DAS) dei campioni P3_1, P3_2, P3_3 e P3_4.

	P3_1 : 300 W, S1	**P3_2 : 300 W, S2**	**P3_3 : 600 W, S1**	**P3_4 : 600 W, S2**
DAS (µm)	1,9 ± 0,3	2,1 ± 0,2	2.9 ± 0,4	3.0 ± 0,3

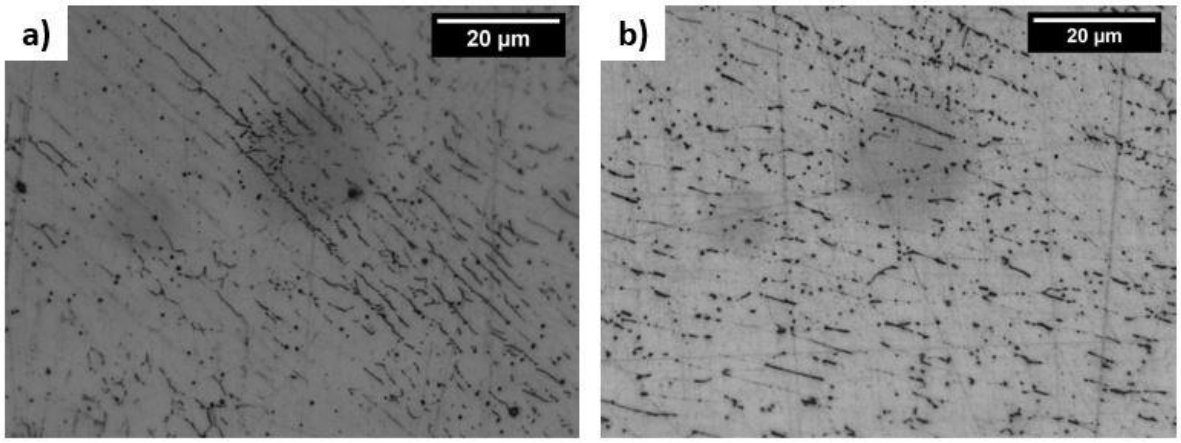

Figura 18: Micrografie OM della spaziatura delle braccia dendritiche dei campioni a) P3_5, 1000 X e b) P3_7, 1000 X.

L'attacco chimico con la soluzione Kalling No.2 ha anche permesso di calcolare la dimensione dei melt pool e, quindi, analizzare la geometria degli scan e l'effetto che la potenza del laser e la strategia di scansione hanno su di essa.

Per quanto riguarda i cerchi, la Figura 19 mostra le caratteristiche geometriche dello scan che sono state misurate per ciascun campione utilizzando il software Image J. In particolare, W e H sono rispettivamente la larghezza e l'altezza del melt pool, G è la crescita e D è la profondità. Inoltre, è stato calcolato anche il parametro Linear Energy Density (*LED*), $LED = P / (v \cdot 60)$, dove P è la potenza del laser e v è la velocità di scansione. Il *LED* è un parametro molto importante e utile per quantificare un processo laser e per vedere come gli effetti in termini di microstruttura e proprietà di un componente sono correlati ai parametri di processo.

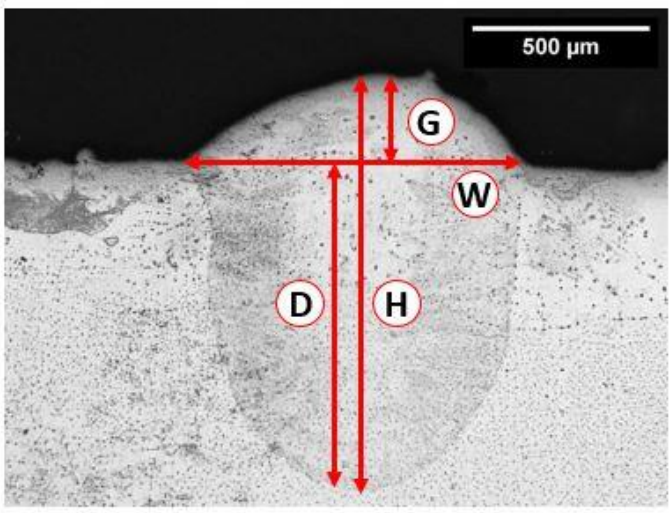

Figura 19: Parametri geometrici calcolati per ogni scan dei cerchi attraverso il software Image J.

Per quanto riguarda i cerchi, sono stati analizzati in particolare i quattro campioni P5_1, P5_2, P5_3 e P5_4 (i cui parametri di processo sono elencati nella Tabella 2), che presentano la stessa velocità di scansione (450 mm / min) ma diverse potenze del laser (300 W e 600 W) e strategie opposte. I risultati sono riportati in Figura 20 a), b), c) e d).

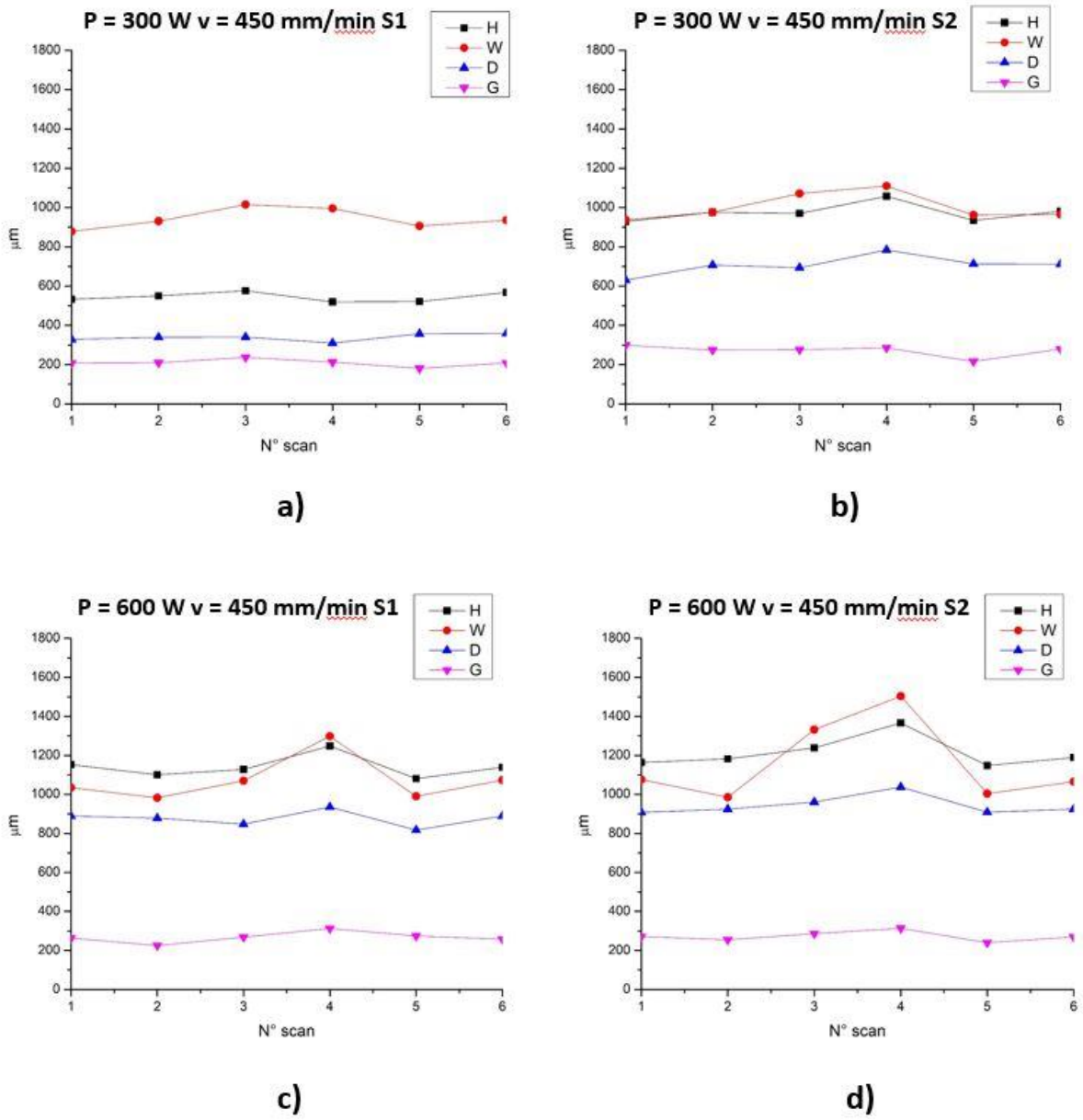

Figura 20: Misura dell'altezza (H), larghezza (W), crescita (G) e profondità (D) del melt pool dei campioni a) P5_1, b) P5_2, c) P5_3 e d) P5_4.

Da questi risultati si può dedurre che, lavorando a basse potenze (300 W), la strategia di scansione non ha effetto sulla larghezza e sulla crescita dei melt pool, mentre influenza fortemente l'altezza degli scan che tende quasi a raddoppiare (da 500 µm con strategia S1 a 900 µm con S2). Infatti, poiché con la strategia S2 si inizia a sinterizzare le polveri dal cerchio esterno per poi muoversi verso quello interno, si ha un maggiore quantità di calore accumulata e quindi un'altezza degli scan maggiore. La strategia, inoltre, influisce sulla profondità del melt pool che raddoppia (da 300 a 600 µm). Passando a potenze maggiori (600 W) e confrontando i campioni con stessa potenza ma strategia opposta, l'altezza, la larghezza, la crescita e la profondità sono uguali per entrambi i campioni. Pertanto, quando il processo richiede potenze elevate, l'effetto del cambio di strategia viene superato dal parametro di processo particolarmente elevato e quindi non vi è alcun cambiamento nella geometria del melt pool. Considerando la stessa strategia e confrontando i campioni con potenza diversa (300 W e 600 W), si può notare che l'altezza, la larghezza e la profondità aumentano, mentre la crescita è l'unica grandezza che rimane costante in tutti i campioni. Per questo motivo, si può affermare che sia l'aumento della potenza del laser sia il cambio di strategia di scansione influiscono principalmente sull'altezza e sulla

profondità. Se l'obiettivo principale è ottenere un aumento della larghezza, è necessario solo aumentare la potenza del laser senza agire sulla strategia. Al contrario, poiché la crescita è sempre costante, l'aumento della potenza del laser o il cambio di strategia non hanno alcun effetto sulla crescita del melt pool.

Usando questi dati geometrici, è stato possibile calcolare per i campioni P5_1, P5_2, P5_3 e P5_4 l'efficienza della polvere P_e, come $P_e = (A_c \cdot F \cdot \rho_p)/f$, dove A_c (mm^2) è l'area dello scan (approssimata all'area di un triangolo di base la larghezza W del melt pool e altezza la crescita G), f (g/s) è la velocità di alimentazione, F (mm/min) è la velocità di deposizione e ρ_p (g/cm^3) è la densità della polvere. I parametri di processo dei campioni selezionati sono riportati in Tabella 2 e la densità della polvere è stata considerata come la densità teorica del 316L, ossia 7.99 g/cm^3. I risultati del calcolo dell'efficienza della polvere per i quattro campioni analizzati sono riportati in Figura 21.

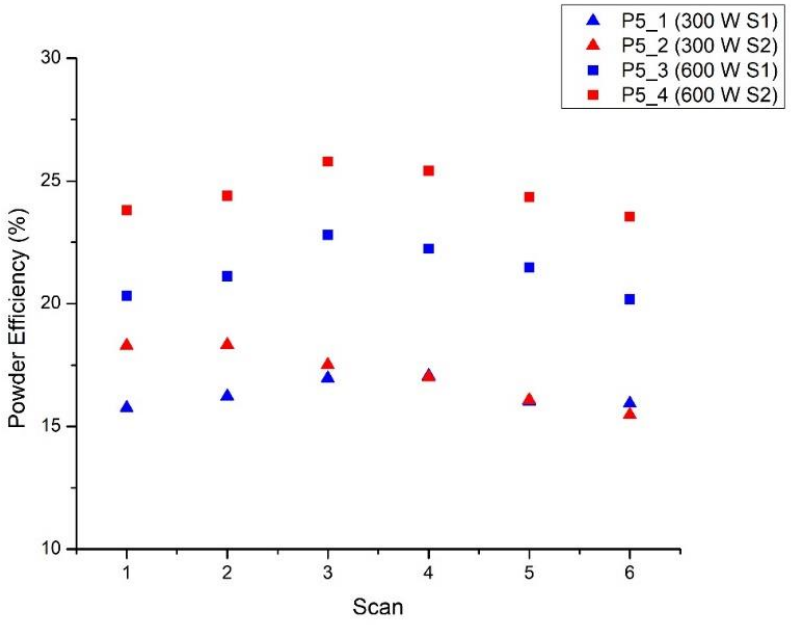

Figura 21: Efficienza della polvere dei campioni P5_1, P5_2, P5_3 and P5_4.

Dalle misure effettuate sui quattro campioni, è stato osservato che per i campioni P5_1 e P5_2 costruiti con potenza relativamente bassa (300 W), si ottengono valori medi di efficienza della polvere di circa il 17%, mentre se si lavora con potenze laser più elevate, come 600 W, l'efficienza della polvere raggiunge valori del 23%. Inoltre, per quanto riguarda l'effetto della strategia di scansione, confrontando i campioni P5_1 e P5_2, essi hanno un valore di P_e del 14 e del 19%, rispettivamente, mentre i campioni P5_3 e P5_4 hanno un valore di P_e del 21 e del 24%, rispettivamente. Per questo motivo, la strategia S2 (dall'esterno verso l'interno) sembra essere preferibile perché permette di raggiungere valori di P_e più elevati. È importante, tuttavia, sottolineare che il processo DED ha generalmente bassi valori di efficienza della polvere, quindi questo potrebbe portare a grandi quantità di polveri metalliche riciclate e "scartate". Per questo motivo, è molto importante capire se la polvere metallica che è già stata introdotta in un processo DED può essere riutilizzata, garantendo così un riciclo delle materie prime e quindi una riduzione degli scarti.

Per quanto riguarda le spirali, le caratteristiche geometriche che sono state misurate per ciascun campione sono mostrate in Figura 22. In particolare, Wtot è la larghezza totale dei cinque melt pool e W è la larghezza di un singolo melt pool, H è l'altezza, G è la crescita e D è la profondità del melt pool. Inoltre, sono stati calcolati il parametro Linear Energy Density (LED), così come la percentuale di overlap (Ov) per studiare l'effetto di sovrapposizione.

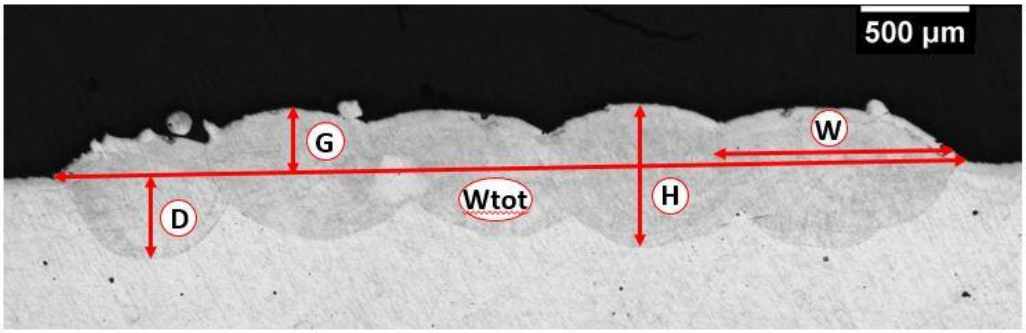

Figura 22: Parametri geometrici calcolati per ogni scan delle spirali attraverso il software Image J.

L'effetto della strategia di scansione è chiaramente visibile in Figura 23, dove le micrografie dei campioni P3_3 e P3_4 sono messe a confronto. Nel campione realizzato con strategia S1 (P3_3), il cerchio interno è coperto da quelli esterni, mentre utilizzando la strategia S2 accade il contrario. Come è mostrato in Figura 23, non è possibile definire un preciso bordo che delimita la zona di overlap perché, a causa del processo di rifusione, il bordo del primo melt pool non è visibile. Per questo motivo, nelle spirali S2 la larghezza W è calcolata sullo scan interno, mentre per i campioni S1 W è calcolata sullo scan esterno. Questo metodo di misura è illustrato in Figura 24.

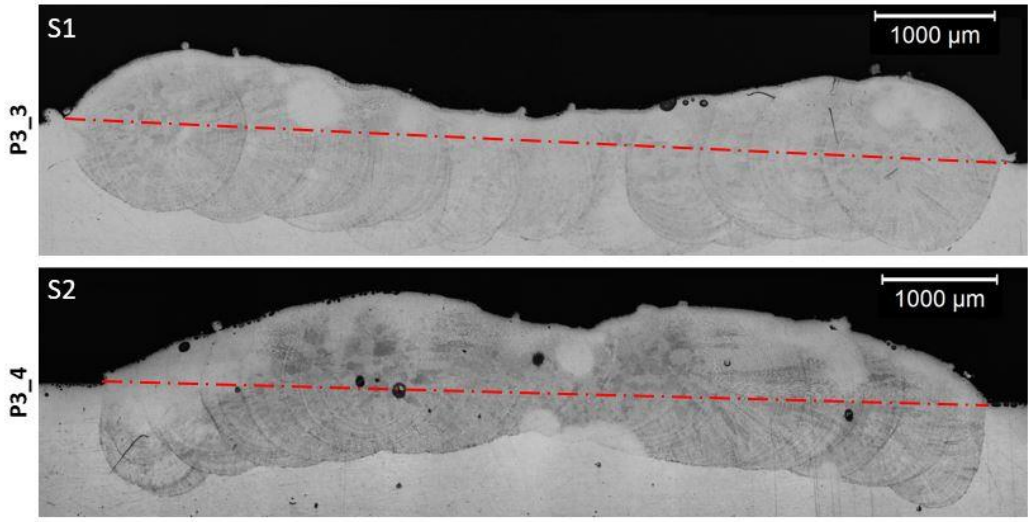

Figura 23: Micrografie OM a 50 X della sezione dei campioni P3_3 e P3_4; i trattini rossi indicano la linea della piattaforma.

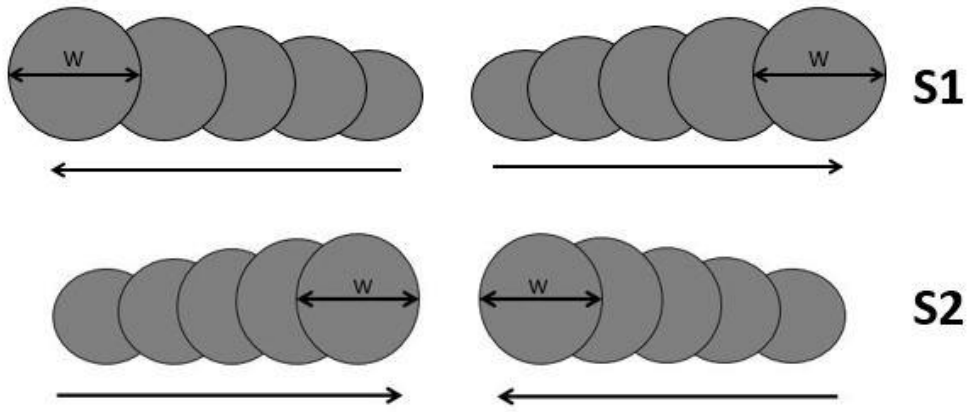

Figura 24: Rappresentazione schematica della misura della larghezza W per entrambe le strategie di scansione, S1 e S2.

I risultati più interessanti sono riportati in Figura 25, in cui la larghezza totale (Wtot) dei cinque melt pool e l'altezza media (H mean) dei cinque scan sono state diagrammate in funzione della percentuale di overlap.

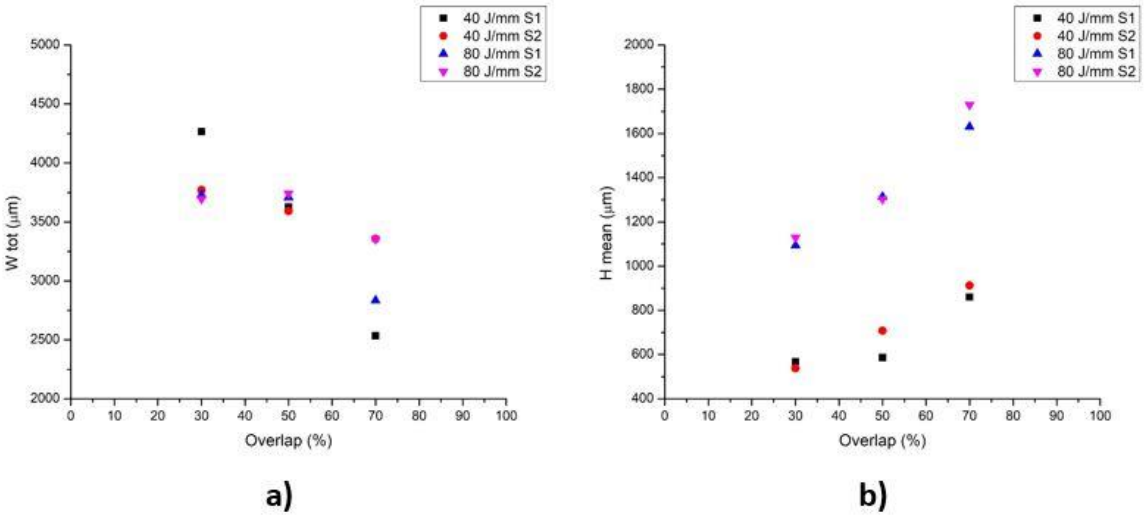

Figura 25: a) Larghezza totale e b) altezza media in funzione della percentuale di overlap.

Osservando i risultati in Figura 25, si può notare come la larghezza totale diminuisce all'aumentare della percentuale di overlap, perché gli scan sono maggiormente sovrapposti, pertanto la larghezza totale sarà più piccola, come illustrato nella rappresentazione schematica di Figura 26. Invece, l'altezza media aumenta quasi linearmente con la percentuale di overlap perché, se il valore di overlap è elevato, l'accumulo di calore è notevole e questo risulta in altezze degli scan importanti (Figura 26).

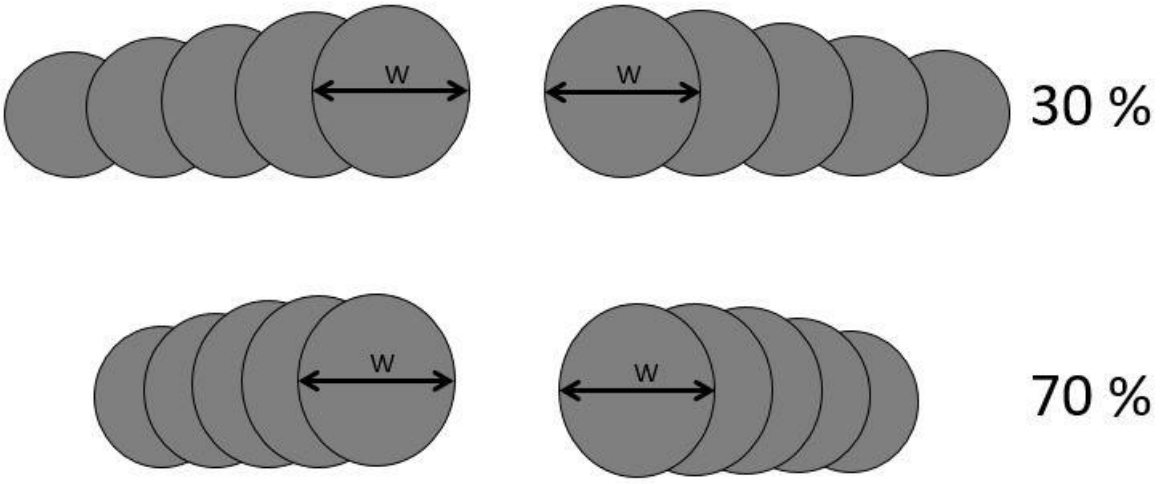

Figura 26: Rappresentazione schematica della percentuale di overlap (30 % e 70 %).

Considerando elevati valori di overlap, la scelta della strategia di scansione ha un effetto importante sull'altezza dello scan. Infatti, come mostrato in Figura 24, l'uso della strategia S1 determina un'altezza di scansione esterna più alta rispetto a quella della scansione più interna. Questo si verifica in quanto la strategia S1 inizia dal cerchio interno e si sposta su quello esterna, quindi quando l'ultima scansione viene depositata, questa andrà a cadere sulla scansione precedente che è già in fase di solidificazione, avendo così una crescita più elevata. Questo fenomeno è particolarmente visibile quando si utilizzano potenze laser elevate e valori di overlap elevati, come mostrato nella Figura 27, mentre se si utilizzano bassi overlap e basse potenze, questo fenomeno non è più visibile.

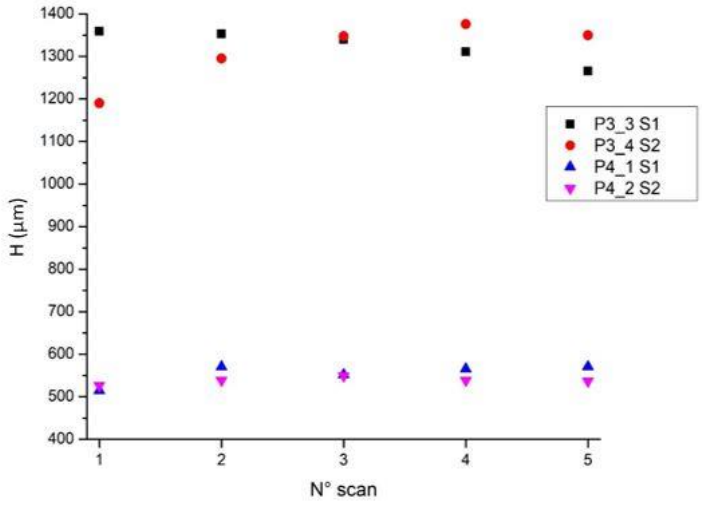

Figura 27: Altezza dello scan in funzione del numero dello scan per i campioni P3_3 (600 W, 50 % Ov, S1), P3_4 (600 W, 50 % Ov, S2), P4_1 (300 W, 30 % Ov, S1), P4_2 (300 W, 30 % Ov, S2).

Infine, per quanto riguarda le prove meccaniche, i test di microdurezza Vickers sono stati effettuati sulla sezione di tre campioni, P5_1, P5_3 e P5_4, appartenenti alla Piattaforma 5 e i cui parametri di processo sono riportati in Tabella 2. Per ciascuno scan del campione, è stata realizzata una griglia sulla sezione parallela alla direzione di crescita, assicurando una distanza di 150 µm tra un'indentazione e l'altra. Analizzando i primi due campioni, P5_1 (300 W) e P5_3 (600 W), è stato valutato l'effetto della potenza sulla microdurezza. Al contrario, analizzando il secondo campione P5_3 (S1, dal cerchio interno a quello esterno) in confronto con il terzo campione P5_4 (S2, dal cerchio esterno a quello interno) è stato studiato l'effetto della strategia di scansione. I risultati della prova di microdurezza Vickers e le risultanti mappe sono riportate in Figura 28.

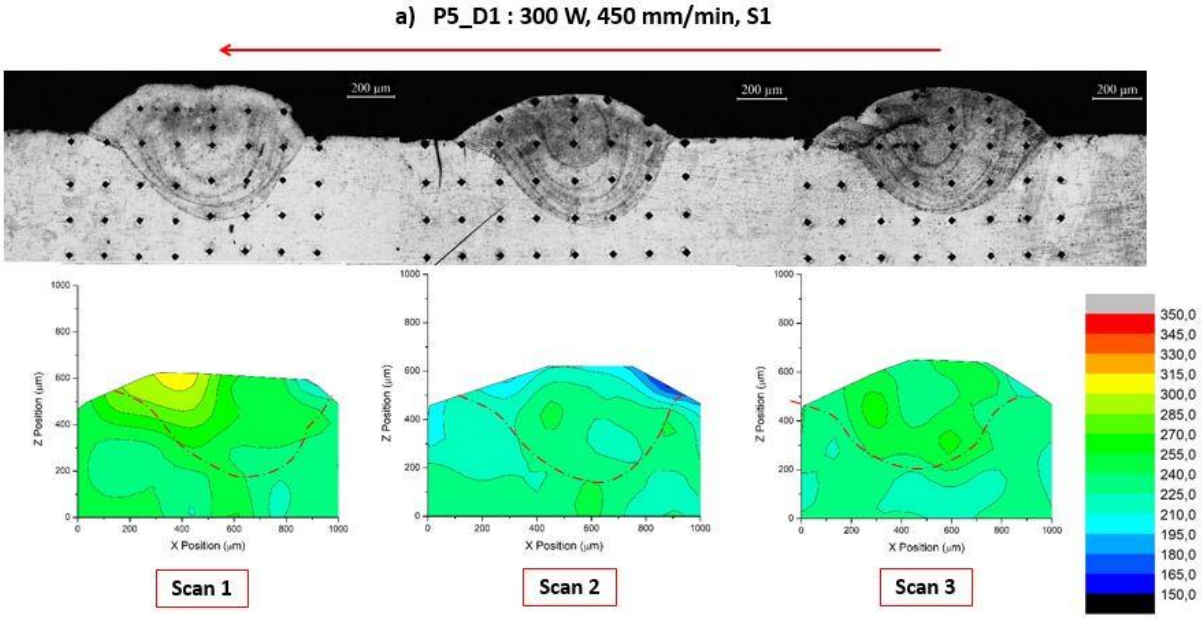

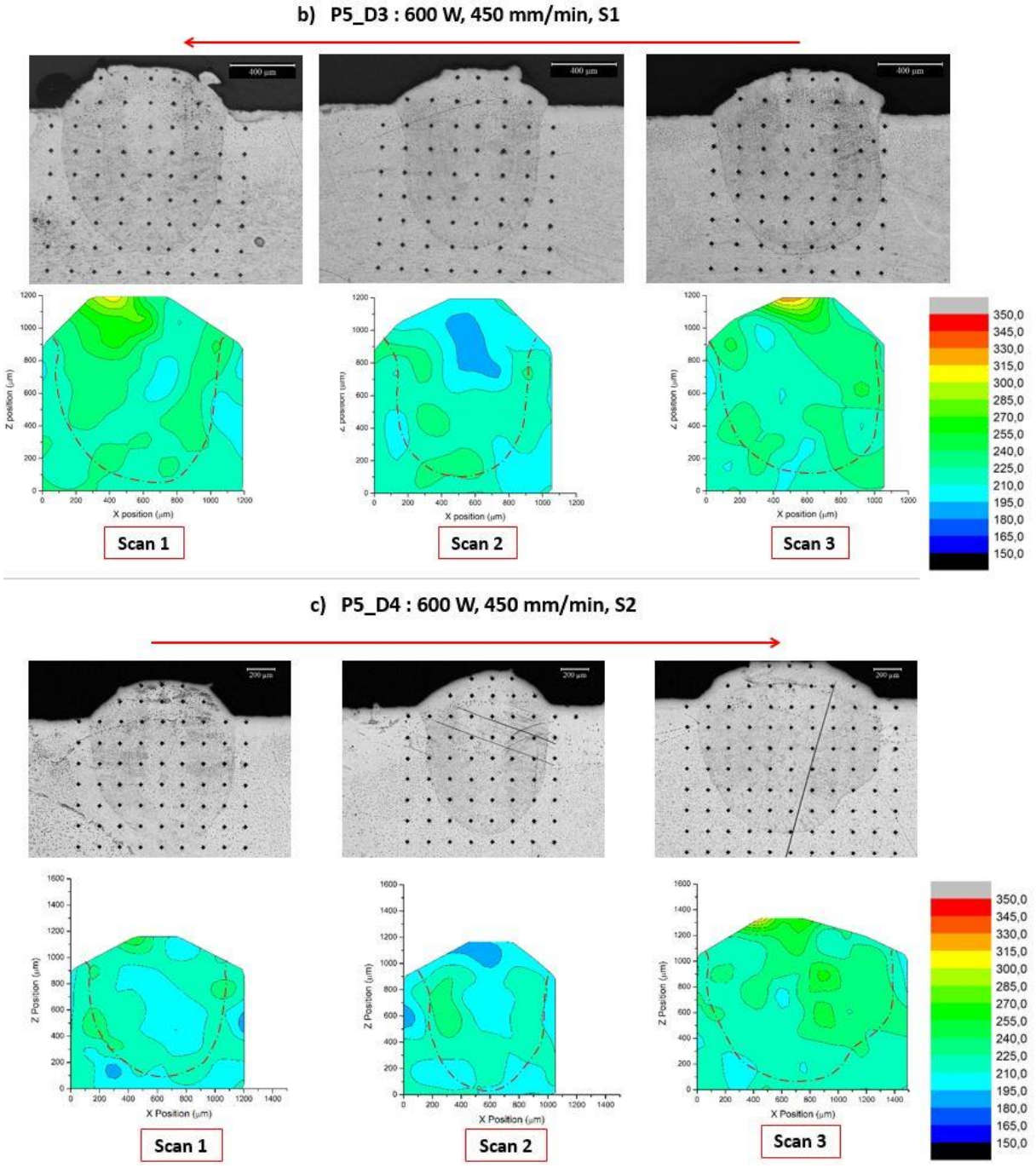

Figura 28: Griglie di indentazione e mappe di microdurezza Vickers per i campioni a) P5_1, b) P5_3 e c) P5_4.

I valori di microdurezza Vickers registrati per tutti i melt pool sono leggermente superiori rispetto al valore di microdurezza della piattaforma in 316L. Come mostrato in Figura 28, la microdurezza è quasi omogenea in tutto il melt pool fino alla piattaforma. Avvicinandosi al centro del melt pool, la micro-durezza aumenta leggermente e questo fenomeno è visibile soprattutto nello scan 3 di ciascun campione. Un aspetto comune per tutti e tre i casi è che la scansione esterna ha una microdurezza più elevata: infatti, essa si raffredda più velocemente perché ha una superficie di scambio più ampia e quindi, alla fine del processo, avrà una microstruttura più fine che conferisce una maggiore durezza. Osservando le mappe in Figura 28, si può ancora notare che, aumentando la potenza del laser e concentrandosi sull'area del melt pool, il campione P5_3 costruito con una potenza di 600 W ha una durezza inferiore in tutte le scansioni rispetto a quella del campione P5_1 costruito con una potenza di 300 W. Ciò è dovuto al fatto che se la potenza del laser aumenta, il melt pool solidifica più lentamente e quindi assume

una microstruttura grossolana, quindi un valore di microdurezza inferiore. Per quanto riguarda l'effetto della strategia di scansione, utilizzando la strategia S1 la differenza in microdurezza della prima e della terza scansione (che presentano una durezza maggiore) con la seconda (che presenta una durezza inferiore) è più marcato rispetto al caso in cui viene utilizzata la strategia S2. Impiegando la strategia S1, infatti, la prima scansione realizzata è quella interna, che in effetti ha un'elevata durezza nell'area del melt pool. Tuttavia anche la scansione esterna ha un'elevata durezza perché, nonostante sia depositata per ultima e quindi sia influenzata dall'accumulo di calore dovuto alle scansioni precedenti, potrebbe essere in grado di scambiare più facilmente calore con l'ambiente e quindi solidificarsi rapidamente e avere una durezza elevata.

La durezza è stata poi studiata su scala nanometrica, realizzando delle misure di nanoindentazione sulla sezione del campione P5_2 della Piattaforma 5 (i cui parametri di processo sono riportati in Tabella 2) in quattro aree differenti: la prima misura è stata effettuata nella parte superiore dello scan (TOP), la seconda sul lato sinistro del bordo del melt pool (LEFT), la terza sul lato destro (RIGHT) e l'ultima sul fondo del melt pool (BOTTOM) (Figura 29).

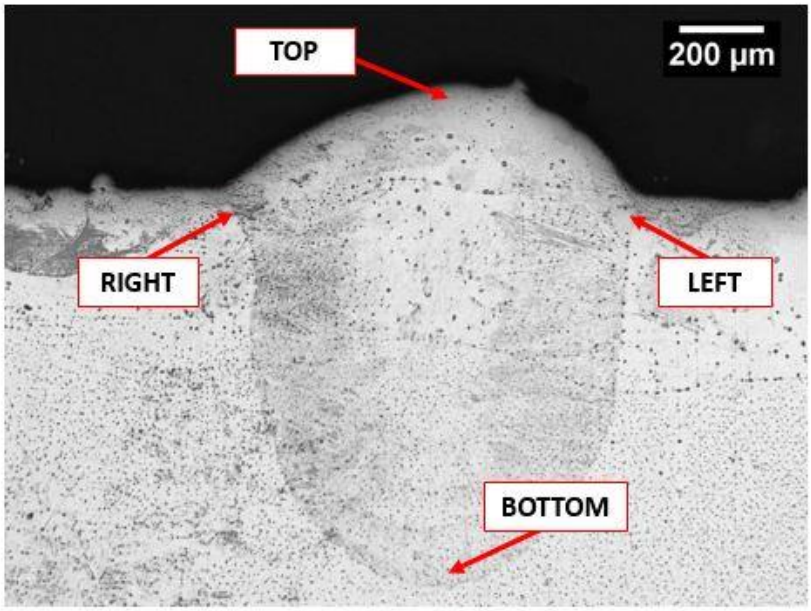

Figura 29: Quattro differenti aree in cui sono state realizzate le misure di nanoindentazione.

I risultati dei test di nanoindentazione confermano che la durezza all'interno del melt pool è omogenea anche a livello nanometrico. La parte superiore dello scan presenta una durezza maggiore, in quanto solidifica molto velocemente avendo un'elevata superficie specifica. Infatti, come è stato evidenziato nella trattazione sulla microstruttura dei campioni, la parte superiore dello scan è la regione che presenta la più elevata velocità di raffreddamento e quindi, alla fine del processo DED, presenta una microstruttura fine che conferisce elevata durezza. Comunque, risulta necessario analizzare l'effetto dei parametri di processo e della strategia di scansione anche nella piattaforma massiva, poiché probabilmente l'effetto della strategia sulla durezza non è visibile nel primo strato depositato, ma dopo un certo numero di scan potrebbe diventare più importante.

Conclusioni

In questo lavoro di tesi è stato studiato l'effetto dei parametri del processo DED sulle caratteristiche microstrutturali e geometriche delle scansioni in acciaio inossidabile AISI 316L. Le analisi sono state condotte su due fronti al fine di analizzare l'effetto del processo DED sia sulle polveri che sui campioni.

Per quanto riguarda le polveri, l'obiettivo principale perseguito è stato capire se la polvere di AISI 316L dopo essere stata introdotta in un ciclo DED potesse essere riutilizzata, dato che l'efficienza della polvere del processo è piuttosto bassa (con un massimo del 25% lavorando con alte potenze). Per questo motivo, la possibilità di riutilizzare le polveri è particolarmente auspicabile. Dalle analisi effettuate sulla nuova polvere e quella utilizzata per un singolo ciclo DED, è risultato che le polveri usate hanno una forma più irregolare, dimensioni maggiori e porosità elevata. Inoltre, la durezza delle polveri che hanno subito un ciclo DED è inferiore alla durezza della polvere nuova, di circa il 15%. Da un punto di vista microstrutturale, le analisi XRD hanno dimostrato che la polvere usata è caratterizzata dalla presenza di una nuova fase ferritica, non presente nella polvere originale in quantità rilevabili, ma in generale la microstruttura in entrambe le polveri è fine ed omogenea. È importante sottolineare che i raggi X hanno un limite di rilevamento del 5%, quindi è possibile che ci sia ferrite anche nella polvere nuova in quantità inferiore a quelle rilevabili, ma sicuramente minore rispetto alla polvere usata. Le osservazioni al microscopio ottico hanno evidenziato anche che il lotto di polvere usata contiene particolari microstrutturali che rispondono più prontamente all' attacco chimico rispetto ad altre. Questa diversa risposta evidenzia un possibile diverso comportamento di fusione. Questo aspetto richiede ulteriori indagini per capire se questa polvere possa essere riutilizzata per un nuovo ciclo DED, dopo aver setacciato le particelle che presentano dimensioni adatte al processo. Un altro aspetto che deve essere studiato è la natura dei particolari sub-micrometrici di Si, O e Mn presenti principalmente nella polvere usata, ma anche nei campioni DED. È necessario indagare la causa della loro formazione e se sono distribuiti casualmente o hanno siti preferenziali per la loro formazione.

Passando alle analisi effettuate sui campioni, nonostante il fatto che essi siano stati fabbricati con due diverse geometrie e parametri di processo, tutti i campioni hanno la stessa microstruttura all'interno del melt pool. In particolare, la regione superiore del melt pool presenta una struttura fine perché ha una elevata velocità di raffreddamento, mentre la zona centrale ha una struttura più grossolana e il fondo del melt pool vede la crescita di strutture dendritiche colonnari. Anche nei campioni, specialmente nelle aree in prossimità del bordo del melt pool, è stata osservata la fase ferritica tra gli spazi interdendritici e sono state individuate anche le caratteristiche submicrometriche ricche di O, Si e Mn. Entrambi questi risultati sono stati confermati da numerosi studi sul 316L ottenuto da processi additivi che hanno osservato la stessa microstruttura nel melt pool.

Un aspetto molto importante in questo lavoro è stata la valutazione dell'effetto dei parametri di processo e della strategia di scansione sulla microstruttura e sulla geometria dei melt pool. Per quanto riguarda la microstruttura, dalle misurazioni DAS si è notato che l'aumento della potenza del laser porta ad una struttura dendritica più grossolana, poiché l'elevata quantità di calore trasferita al melt pool riduce la velocità di raffreddamento, ritardando il processo di solidificazione. Invece, scegliere una strategia piuttosto che l'altra sembra non influenzare la morfologia della struttura dendritica. Passando ora all'analisi dei melt pool, sono state studiate le geometrie dei campioni, sia per le spirali che per i cerchi. Per quanto riguarda i cerchi, le scansioni centrali hanno una larghezza maggiore di quelle esterne a causa dell'accumulo di calore, indipendentemente dal tipo di strategia utilizzata. Invece, la scelta della strategia influisce sull'altezza delle scansioni che risultano essere più alte quando si utilizza la strategia S2, poiché probabilmente il calore è concentrato principalmente all'interno del cerchio, e questo porta a un maggiore accumulo di calore, quindi ad una scansione più alta. L'aumento di potenza porta ad avere melt pool più profondi e quindi più alti, ma la crescita è l'unica grandezza che resta sempre costante in tutti i campioni. Pertanto, se l'obiettivo è ottenere scansioni con un valore di crescita più elevato, non conviene agire sulla potenza del laser o sulla strategia, poiché agire su questi due parametri influenza solo la profondità e l'altezza delle scansioni.

Per quanto riguarda le spirali, l'analisi è stata concentrata sullo studio dell'effetto della sovrapposizione. Quando vengono selezionati come parametri di costruzione bassi valori di overlap, il confronto dei campioni ottenuti con le strategie di scansione S1 ed S2 mostra che la strategia S2 fornisce una maggiore sovrapposizione quando vengono utilizzati parametri LED elevati. Inoltre, quando si

utilizzano potenze laser elevate, la sovrapposizione è maggiore di quella nominale perché le elevate potenze laser portano a melt pool più grandi e più profondi, quindi a maggiori valori di overlap. Per questo motivo, valori di potenza inferiori garantiscono la percentuale di sovrapposizione stabilita in fase di progetto ovvero migliore accuratezza. Osservando l'effetto dei parametri di processo su altezza e larghezza, si è osservato che la larghezza totale diminuisce all'aumentare della sovrapposizione, poiché le scansioni sono più sovrapposte, quindi la larghezza totale sarà inferiore. Invece, l'altezza media aumenta quasi in modo lineare con la percentuale di overlap, perché se il valore di sovrapposizione è elevato, l'accumulo di calore è notevole e ciò comporta elevate altezze di scansione. Considerando l'altezza delle scansioni, esse sono influenzate dal cambio di strategia perché, a seconda della direzione della deposizione (dal cerchio interno a quello esterno (S1) o dal cerchio esterno a quello interno (S2)), l'ultima scansione ha un'altezza maggiore in riferimento alla linea di base della piattaforma, dando così al campione una geometria caratteristica a seconda che venga utilizzata la strategia di scansione S1 o S2. Questo fenomeno è particolarmente visibile quando si utilizzano potenze e valori di overlap elevati. Pertanto, confrontando i risultati di entrambe le geometrie, si può affermare che la strategia ha poca influenza sulla dimensione del melt pool, mentre la variazione della potenza del laser influenza le grandezze geometriche e, nel caso delle spirali, anche il valore di overlap ha un effetto decisivo sulla forma delle scansioni. Un aspetto che sarebbe interessante ulteriormente valutare è l'effetto della variazione della velocità di scansione e della velocità di alimentazione sulla geometria dei melt pool, poiché in questo lavoro questi due parametri avevano un valore costante in tutti i campioni.

Infine, da un punto di vista meccanico, la durezza delle scansioni è stata valutata per diversi campioni con geometria a cerchi concentrici sia a livello micro che a livello nano. In entrambi i casi, è stato notato che la durezza è abbastanza omogenea muovendosi dal melt pool alla piattaforma di 316L. Man mano che ci si avvicina alla parte superiore/centrale del melt pool, la microdurezza aumenta leggermente perché questa regione è la più veloce a solidificare, assumendo anche una struttura a grana fine. Aumentando la potenza del laser e concentrandosi sull'area del melt pool, il campione costruito con una potenza maggiore ha una durezza inferiore in tutte le scansioni rispetto a quella dei campioni costruiti con una potenza inferiore. Ciò è dovuto al fatto che, se la potenza del laser aumenta, il melt pool solidifica più lentamente e quindi assume una microstruttura più grossolana. Per quanto riguarda l'impatto della strategia di scansione, utilizzando la strategia S1, la differenza nella durezza della prima e della terza scansione con la seconda è più visibile rispetto al caso in cui viene utilizzata la strategia S2. Impiegando la strategia S1, la prima scansione depositata è quella interna, che in effetti ha un'elevata durezza nell'area del melt pool; ma anche la scansione esterna ha un'elevata durezza poiché, anche se depositata per ultima e quindi influenzata dall'accumulo di calore dovuto alle scansioni precedenti, potrebbe essere in grado di scambiare più facilmente calore con l'ambiente e quindi solidificarsi rapidamente e avere una durezza elevata. Un aspetto che necessita di un'ulteriore analisi è il motivo per cui la piattaforma in cui sono stati costruiti i campioni con potenze inferiori ha una durezza più elevata rispetto a quella dei campioni costruiti con potenze più elevate e bisognerebbe comprendere la relazione tra questo fenomeno e la zona termicamente alterata (HAZ).

Index

1. Introduction

The American Society for Testing and Materials (ASTM International) defines Additive Manufacturing (AM) as "*a process of joining materials to make objects from 3D model data, usually layer upon layer, as opposed to subtractive manufacturing methodologies*" (ASTM F2792). This is a process that can be applied to all classes of materials including metals, ceramics, polymers, composites and biological systems.

While AM has been around as a means of processing materials for, arguably, over two decades, it has only recently begun to emerge as an important commercial manufacturing technology. It has received considerable attention in the past few decades from both the commercial and academic sectors, with over 3500 patents related to AM emerging from 1975 to 2011 [6]. Time has demonstrated that AM is not just restricted to rapid 'printing' of prototypes, but is also a means for generating fully functional parts for service in a variety of applications.

The fundamental premise of AM is to create a part by effectively joining materials (similar or dissimilar), typically in a layer-by-layer fashion via CNC (Computer Numerical Control) displacement, from imported three-dimensional (3D) model data. In this way, a machine can "assemble" a 3D part by bonding materials, with each new layer of material being a manifestation of 3D model cross-sectional data. These models are typically in the form of Computer Aided Drawings – CAD in the STL (Standard Tessellation Language) file format and are 'sliced' into many fictious cross-sectional areas, which dictate the CNC displacement.

Nowadays, among the emerging production technologies, additive techniques are the most promising because they are characterized by:

- the possibility to produce components with complex geometries that cannot otherwise be realized in a single piece with traditional techniques;
- a great process flexibility and drastic reduction in the costs of making variations compared to a basic model;
- the reduction of production waste;
- the possibility of printing components and mechanisms already assembled;
- a drastic reduction of "time to market": the ability to produce small batches to be marketed immediately to test their effectiveness and appeal, to make changes as needed by users, and then to start production on large scale, results in effective time and cost savings, offering unprecedented competitive advantages.

The main areas in which additive technologies have replaced the traditional technologies are aerospace, the production of components of aeronautical engines, biomedical, with particular reference to the production of prosthetic supports in the orthopaedic field, orthodontics and the production of audio protection, the production of components for the motorsport sector.

To accomplish effective material joining, the successful combinations of material, or feedstock, and energy delivery are required and they differ with process material and various AM machines. As the process material changes, then so can the material 'preform'. For this reason, manufacturing systems can be divided into three broad categories: (i) powder bed systems, (ii) powder feed systems, and (iii) wire feed systems [7]. The typical ASTM-recognized AM methods are material extrusion, material jetting, sheet lamination, vat photopolymerization, binder jetting, Direct Energy Deposition (DED) and Powder Bed Fusion

(PBF). Each AM method is tailored for building a specific type of material, so that the effective material deposition and joining can be unique.

When it comes to the AM of metallic parts, the DED is one of the most proven and feasible methods. This process involves the deposition of powder metal and their simultaneous or subsequent melting via a focused laser beam to accomplish layer-to-layer metallurgical bonding. [8].

The current thesis has the aim to evaluate the microstructural and compositional features, the thermal effects and the mechanical behaviour of Stainless Steel AISI 316L samples realized through the DED process. These analyzes aim to characterize:

- the geometry and the extension of the "melt pool" (region of superheated molten metal in proximity to the laser/material interface);
- the presence of porosity, cracks and impurities and their distribution;
- the microstructure;
- the element distribution.

The analysis of these samples are part of a European project called *Borealis*, and coordinated by Prima Industrie in collaboration with a large group of multi-national companies. The project looks to combine different technologies in a single machine to deliver true-net-shape products through a real-one-step process with an unprecedented material usage efficiency and energy efficiency. Borealis will implement an advanced 3D laser scanner that will support different laser based additive and subtractive technologies. For the first time ablation technology will complement the AM fabrication process to allow surface finishing and micro texturing that would be unachievable in one processing step. The machine will be equipped with an innovative flexible revolver head that will enable blending multiple powders of different materials and with different particles dimensions (micro and nano powders). In this way, Borealis will enable the integration of multiple AM technologies in one single machine to combine the most productive alternative with the most precise one with zero set-up time and zero material waste. It would like to offer world class efficiency and the highest throughput rate (2000 cm^3/h) with unprecedented surface quality (submicron rugosity) and it will minimize powder losses by guaranteeing a controlled atmosphere in the operative region (thanks to a shielded working space that encapsulates all ejected powders and protects them from oxygen contact).

In this thesis, chapter 2 describes the DED process and state of the art on the AISI 316L obtained from AM. Chapter 3 introduces the materials used and the analyses undertaken in this study. The results and conclusions are presented in Chapter 4 and 5, respectively.

2. Background

2.1 Direct Energy Deposition (DED)

Directed Energy Deposition (DED) utilizes metal wire and/or powder preforms that are directly deposited to a work site accompanied with simultaneous irradiation of a laser beam. Coupled with a moving substrate, DED provides for a pool of molten metal that travels in space and time. The substrate is the 'stage' in which the additive manufacturing process occurs. As shown in Figure 2.1, in-line with the deposition head, which can consist of either a single powder-spray nozzle or multiple nozzles, there is a focused laser beam. When particles or wire feedstock are deposited, the laser beam provides sufficient thermal energy to melt the particles along the deposition path. In this way, it creates a molten pool (liquid metal) that is a heat-affected zone (HAZ) with a penetration depth. Once the deposition of a single layer is complete, the build plate moves via CNC relative to the deposition head and the process is repeated. Thermal monitoring may be implemented through the use of infrared cameras and/or pyrometers. Earlier DED systems consisted of single, coaxial nozzles (coaxial with laser beam) in atmosphere, while current DED machines may have up to four (or more) nozzles and utilize inert gas as to minimize high oxidization rates inherent for elevated temperature metal processing (Figure 2.1).

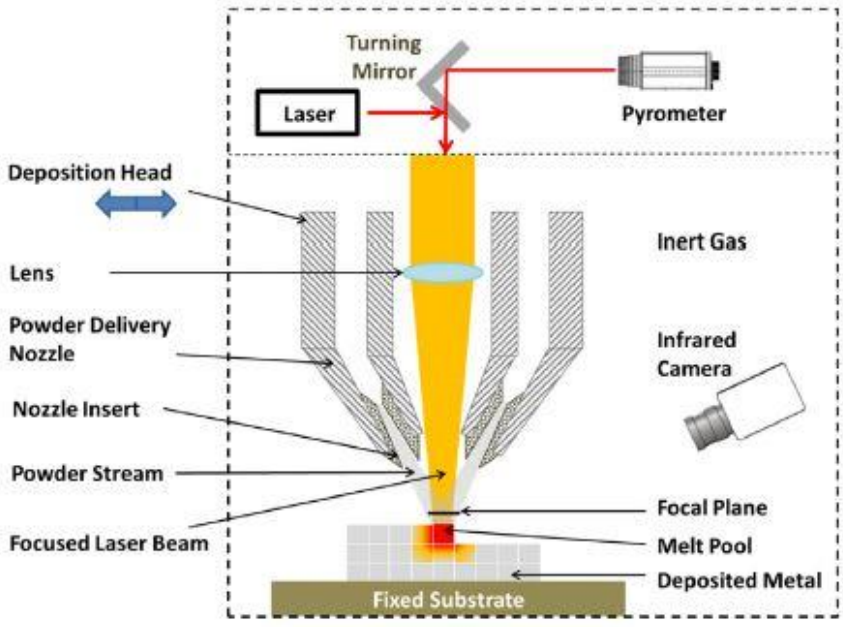

Figure 2.1: Blown powder Directed Energy Deposition (DED) with thermal monitoring [8].

Another very used method to make AM metallic prototypes/parts is Powder Bed Fusion (PBF) process that makes components via the incremental height-wise movement of a table consisting of a compact, uniformly distributed layer of metallic powder that is selectively melted by a focused laser beam, as DED. The main differences between DED and PBF can be exploited for various applications and end-user needs. PBF can provide for finished parts with finer surface quality, but a de-powdering procedure is required. DED may require a post-AM machining procedure, but the surface quality may not be as fine as a PBF part. PBF may be

more advantageous for construction of 3D structures with over-hanging parts, since the powder bed acts as a supporting structure. The lasers utilized for PBF usually have lower power (due to the finer powder size) than those required for DED. Since DED does not rely on a pre-deposited layer of metallic powder, it may be used as a means to repair or coat parts via cladding. In addition, DED can be utilized for creating functional graded/composed parts with different material/alloy concentrations. Finally, preform mixing can be accomplished with DED, such as coaxial powder delivery and lateral wire feeding.

Directed Energy Deposition has demonstrated to effectively fabricate a wide range of materials such as: titanium alloys, tool steels, austenitic steels, martensitic steels, nickel-base superalloys and cobalt-base alloys [9].

2.1.1 Powders

Powders can vary in size, shape and in terms of how they are produced. For most DED applications, the powders are larger in size compared to those used in PBF-L processes. For DED, it is common to see powders range between 10 and 100 µm and are typically spherical in shape. Spherical-shaped particles can reduce any entrapment of inert gas within the melt pool and can thus lead to a final part with less porosity.

Gas atomization, water atomization and plasma rotating electrode processes (PREP) are typical means for producing powders effective for DED application. The particle feed rate is the average mass of particles leaving the DED nozzle with respect to time and can range between 1-10 g/min (grams per minute). The inter-layer idle time is the finite time elapsed between successive material/energy deposits or layers and can range, for example, from 0 to 1000 s [8].

2.1.2 Physical events

Powder-based DED consists of many interconnected, coupled physical events, all occurring at a very short time scale. As shown in Figure 2.2, some of these physical events, in order of approximate occurrence, include: laser delivery, particle/powder delivery, laser/powder/gas interactions, melt pool initiation (melting), melt pool energy/stability/morphology, heat loss to environment via thermal radiation and convection, solidification, intra-part conduction, thermal cycling and part-to-substrate conduction.

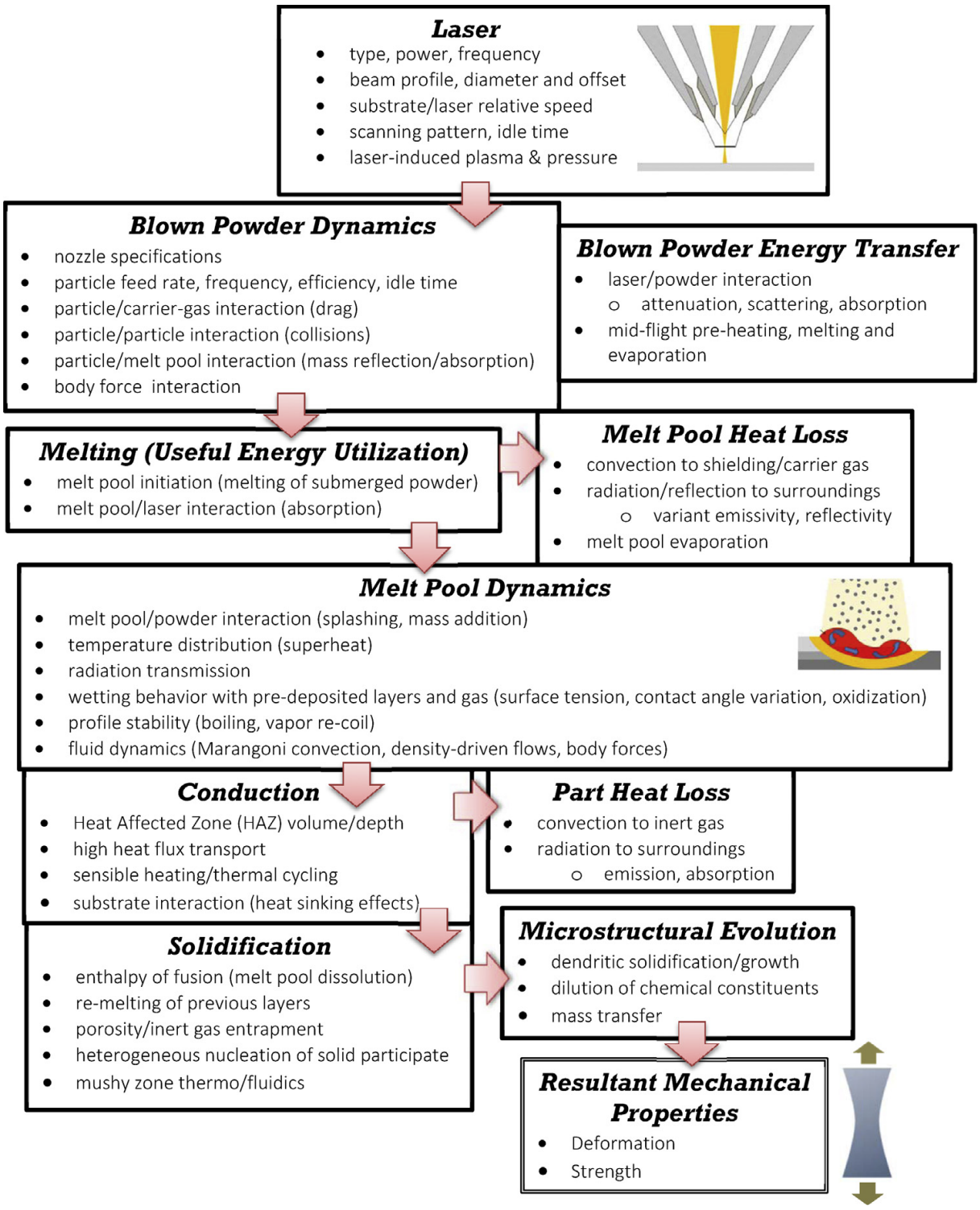

Figure 2.2: Physical events occurring during DED for given instant in time [8].

Each following point in this section will highlight major findings relevant to these physical events.

1) Laser and powder delivery: powder-based DED allows both material and energy delivery to occur simultaneously at a given location. This is accomplished by the careful combination and integration of blown powder and a relatively high laser power source. DED machines can have either a single-nozzle or multi-nozzle in order to introduce the continually

fed powder stream. The laser beam is carried into the DED chamber and then directed to the deposition region using a plano-convex lens. The type of laser, and its maximum power capability, varies between various DED machines. Typically, a Nd:YAG (neodymium-doped yttrium aluminium garnet) laser is used with power ranging between 1 and 5 kW. Another type of laser is the CO_2-type laser, which has wavelengths an order-of-magnitude larger with respect to the Yb:YAG one (10.6 μm) and this can result in a less energy efficient DED process. Utilization of CO_2 lasers for DED can require very high powers, with maximum laser capacities near 18 kW [8].

Laser attenuation occurs due to the blown powder absorbing and scattering the electromagnetic radiation. The radial laser power intensity profile, e.g. in Figure 2.3 a), and ratio of attenuated-to-original laser power, e.g. in Figure 2.3 b), both are affected by the intersecting powder stream feed rate and profile [10]. For fixed laser power, increasing the powder feed rate will result in a slight decrease in the mean temperature of the powder stream and a higher degree of laser attenuation as shown in Figure 2.3 b) for a Gaussian irradiation profile. It may be noticed that laser attenuation can be significant and can result in only 75% of original power reaching the melt pool surface. Furthermore, toward the centre of the laser beam, the ratio of attenuated-to-original laser power is lowest: this means that the powder closest to the beam centre absorbs more energy and can even melt mid-flight.

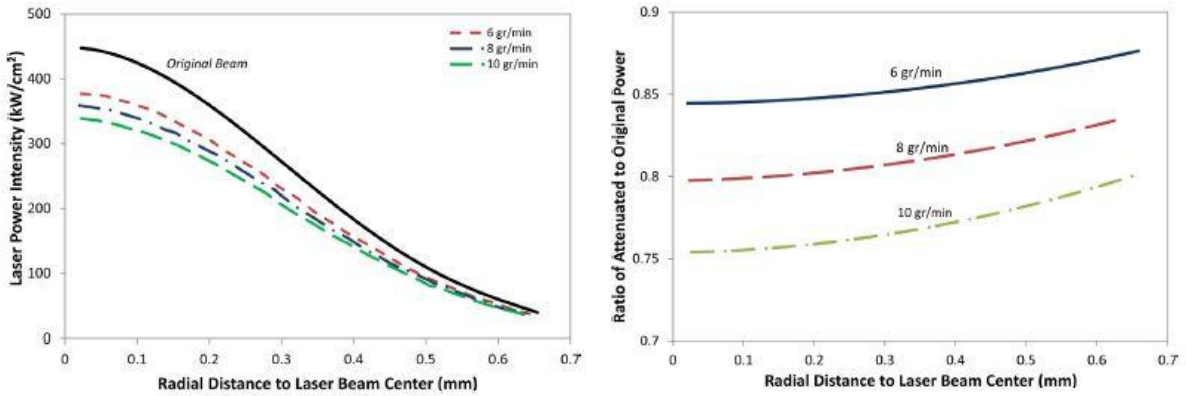

a) b)

Figure 2.3: **a)** Laser power intensity vs. radial distance for various powder feed rates (H13 tool steel, laser power = 2200 W, beam diameter = 1.2 mm and traverse speed = 5 mm/s), **b**) Ratio of attenuated-to-original power vs. radial distance for various powder feed rates (H13 tool steel, laser power = 2200 W, beam diameter = 1.2 mm and traverse speed = 5 mm/s) [10].

To avoid this complex radiation problem of laser attenuation and particle/melt pool absorption, it can be used a laser-surface coupling coefficient A(T) to scale the input laser power and approximate the incident/delivered power to melt pool region. This coupling coefficient can range between 0.15 and 0.50 and depends on the type of laser utilized, on surface preparation and temperature. The coupling coefficient can be estimated by using the temperature-dependent electrical resistivity of the material through the following Hagen-Rubens relationship:

$$A(T) = \sqrt{8\varepsilon_0 \omega \rho_e(T)} \tag{2.1}$$

where A(T) is the laser-surface coupling coefficient, ε_0 is the permittivity of free space, ω is the angular frequency of the laser irradiation (rad/s) and $\rho_e(T)$ is the material's temperature-variant electrical resistivity. Specific values (for Nd:YAG) can be 0.28 for AISI 316 SS or 0.36 for Inconel 718.

The absorption of the laser irradiance can be affected by the laser-induced plasma that can be formed during DED for high power scenarios. The primary source for plasma is through the vaporization and ionization of mid-flight particles and can be avoided through the correct combination of powder feed rate and laser power. Furthermore plasma effect can be minimized through the use of specific shielding gases, like helium [11].

A very useful and simple means of quantifying energy delivery for unit area of material is the *specific energy* E (J/mm^2) and it is a function of laser power, traverse speed and beam radius:

$$E = \frac{P}{2r_b V_{beam}} \tag{2.2}$$

It is a parameter that can be used to predict layer height/width and whether melting can occur for a given set of parameters [12].

During beam exposure, the blown particles will undergo sensible heating, increase in temperature rapidly, depending on their location in the material jet stream and laser beam. Sometimes, the particles can evaporate due to excessive power transfer during exposure. The main cooling mechanism for mid-flight particles is forced convection with the carrier/shielding gas. Its presence will additionally impact the particle movement by introducing drag force on the material jet stream and can result in particle deceleration and instability during flight.

Another very important parameter that allows to quantify the particle catching ability of the melt pool during a DED process is the *powder efficiency* P_e which is the ratio of powder utilized for final part formation over the actual amount of powder delivered/blown by the system over a given time interval. It is simply calculated from the measured scan area A_c, feeding rate, F, scanning speed, S, and powder density, ρ_p, as follows:

$$P_e = (A_c \cdot S \cdot \rho_p)/F \tag{2.3}$$

The value of P_e gives an idea of how much powder goes inside the melt pool and is involved in the melt after being sprayed from the nozzle. It depends on the nozzle geometry, angle and the size distribution of the particles utilized. The maximum powder efficiency is achieved when the powder jet stream diameter is matched to that of the incident laser beam and it typically increases with deposition layer due to bulk heating effects in the part. Low powder efficiency can lead to large amounts of recycled and 'scrapped' metallic powders. This can increase the manufacturing costs and complexity by introducing routine cleaning/recycling processes within the DED machine [13].

2) The melt pool: the melt pool is the region of superheated molten metal in proximity to the laser/material interface, typically in the form of a spherically shaped droplet that moves at the traverse speed (Figure 2.4). It is thermodynamically unstable, adjusting in shape and in internal energy due to surrounding heat transfer and liquid/solid interactions.

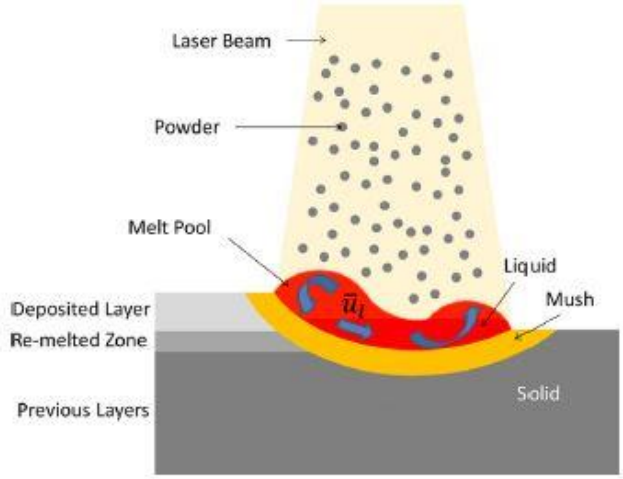

Figure 2.4: Schematic representation of a melt pool during DED [8].

The metallic powder is blown into it while the laser allows its survival via energy transfer. Melt pool morphology, temperature and wetting behaviour are very important parameters in quality control because the melt pool is the initiation of the solid part. Dimensional tolerances and microstructural features of the finished part, as well as the existence of residual stress, depend on the melt pool behaviour and shape during DED process.

Due to the natural limitation of thermal radiation and due to interference from the blown powder, only a portion of the incident laser is absorbed by the melt pool. This portion of heat is then transferred sensibly to the environment either via radiation/convection or sensibly/latently to the combined HAZ/melt pool region. Heat transfer between the melt pool and surroundings (e.g. the DED machine chamber) occurs through convection with the shielding/carrier gas and thermal radiation with surrounding elements. Radiation heat transfer during DED is dictated by the melt pool's spectral emissivity that is a function of its superheat and amount of oxygen within it. Wang and Felicelli demonstrated that the melt pool length and temperature profile are sensitive to changes in the melt pool emissivity, as shown in Figure 2.5 [14].

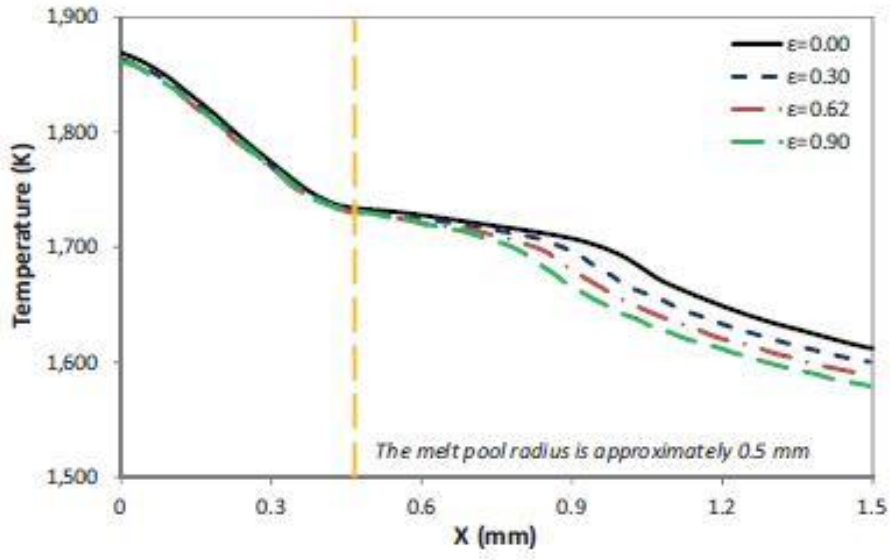

Figure 2.5: Simulated melt pool temperature variation along plane of deposition as function of melt pool emissivity. The centre of the melt pool is at x = 0 mm and approximate melt pool radius is provided [14].

The temperature variation along the substrate is shown in Figure 2.5 in addition with the approximate melt pool length. As the melt pool emissivity decreases, the temperature variation along substrate length becomes more isothermal with a melt pool leading edge/boundary of higher average temperature. For DED of stainless steel, the heat loss due to convection and radiation can be on-the-order of 10% [14].

A power-dependent temperature gradient crosses the entire melt pool because of the sensible heat transfer. This thermal gradient is significant, ranging between 100 and 1000 K/mm and this is attributed to the high heat flux, as the heated boundary is spatially small relative to entire melt pool. The powder injection affects the melt pool superheat, and increasing the powder feed will decrease the melt pool temperature. Griffith et al. demonstrated that, specifically for a DED-build of a H13 tool steel thin-wall, the maximum melt pool temperature is located near the laser and is noticeably higher than the melting temperature (1700 K) of the processed material [15]. A near-Gaussian temperature profile exists in the melt pool, with high-ordered variation near the laser location and more linear variation toward the trailing edge of the melt pool (x = 0), as shown in Figure 2.6. The linear variation can be attributed to solidification heat transfer and pool-to-surroundings, while the high-ordered variation is due to superheat-driven, sensible heat transfer effects near the high heat flux laser/pool interface. In the laser heating zone, the gradient is near-constant due to the phase-change heat transfer, while in the solidifying region, the gradient is non-constant and decreasing with location from the melt pool centre.

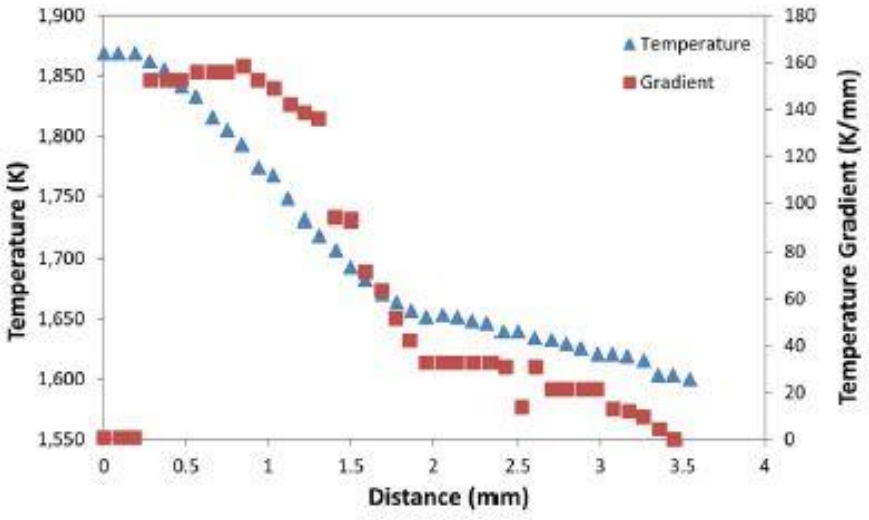

Figure 2.6: Characteristic temperature distribution and gradient along the length/radius of a H13 tool steel melt pool during DED [15].

Wang et al. demonstrated that the temperature distribution within the melt pool is sensitive to laser input power and that it is, for majority of laser powers investigated, superheated above the liquidus temperature [16]. The melt pool temperature distribution becomes more isothermal as the laser power decreases, while its peak temperature increases with higher specific energies (slower traverse speeds and higher laser powers).

He and Mazumder studied the evolution of maximum temperature in the melt pool over time [10]. As shown in Figure 2.7, in the initial period, the temperature increases very quickly due to the sudden input of the laser. After the maximum temperature exceeds the solidus

temperature, the liquid pool begins to form. Then the temperature increases slowly until it reaches a steady state.

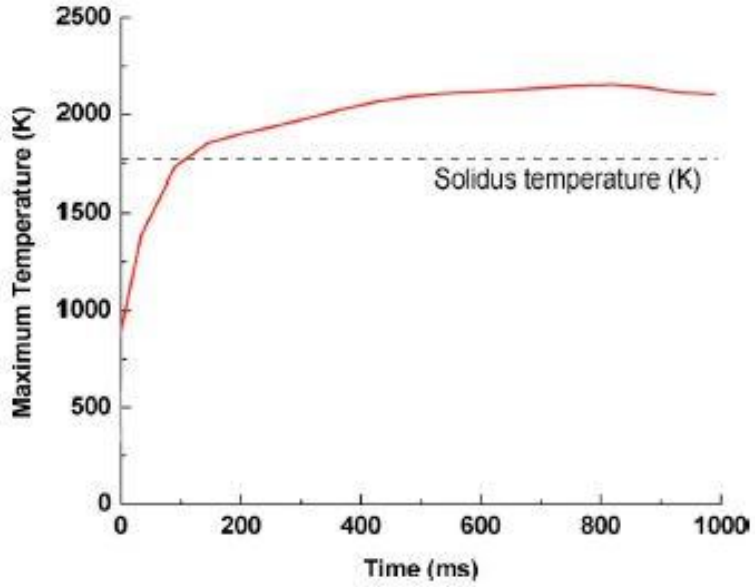

Figure 2.7: Maximum temperature in the liquid pool as a function of time. Laser power: 1900 W, beam diameter: 1.8 mm, scanning speed: 200 mm/min, powder flow rate: 8 g/min [10].

The melt pool temperature and morphology is affected by interfacial forces such as surface tension and metal vapour recoil, the last one being more prevalent at and beneath the melt pool centre. The highest superheat will be directly below the melt pool this can lead to boiling heat transfer (or vapour recoil) characterized by the birth/growth of metal vapour bubbles and trapped inert gas. When the vapour recoil force exceeds the liquid/gas surface tension force near the periphery of the melt pool, the melt pool is expulsed. The recoil force increases with temperature faster than the surface tension force: in this way, as the process parameters are varied as to increase the bulk temperature near the melt pool, mass loss due to boiling in the melt pool can happen. Liquid metal expulsion will increase as the irradiated power intensity increases.

Marangoni convection, that is fluid motion driven by surface tension gradients, is another mechanism that can influence the melt pool temperature. In fact, it can increase the natural convection heat transfer in the melt pool, by increasing advection along the periphery. This mechanism provides for transport of thermal energy from the centre of the laser beam to the melt pool periphery via convection. Melt pool heat transfer and temperature distribution are coupled with melt pool morphology which is also coupled with the wetting behaviour at the part interface. Marangoni transports promotes free convection flows and provides for higher peak velocities in the melt pool and higher intra-pool heat transfer coefficients. If Marangoni transport is negligible, free convection flow is predominant, but the peak velocities are much smaller and the heat transfer through this type of melt pool can be valued only via conduction. The type of Marangoni flow is strongly correlated to the temperature dependence of the surface tension. Previous studies demonstrated in fact that positive surface tension/temperature sensitivity is indicative of a melt pool with narrow and shallow shape with flow occurring inward, toward the centre of the melt pool. Negative surface tension/temperature sensitivity along the melt pool is indicative of a melt pool with a wide and shallow shape with flow occurring outward, toward the periphery of the melt pool.

During DED, a strong temperature variation along the melt pool results in both density and surface tension gradients along its length/thickness. Powder feed rate and particle angle-of-attacks will significantly affect the free surface stability and motion of the melt pool, as well. For a given laser power, molten metals with high surface tension sensitivity to temperature will tend to have higher peak velocities within its melt pool during DED. The peak velocity will increase with laser power for a given focal area: in this way, the temperature difference between the irradiated top surface of the melt pool and its periphery will most likely increase and this will drive stronger convection currents with higher peak velocities.

As far as the morphology and the shape of the melt pool are concerned, the geometry of a deposition track is affected by its fluidic behaviour and solidification rate. The melt pool free surface topology is highly transient because of blown powder entry, gas flow, oxidation and laser irradiation. This morphology is also coupled with surface/fluid phenomena such as surface tension, capillary forces and the melt pool fluid dynamics. The melt pool shape depends on many variables during DED, such as the blown powder efficiency, liquid/solid wetting behaviour, inert gas flow rates, heat transfer and more.

Peng et al. [12] demonstrated that, in general, as the specific energy increases, the deposition layer height, width and depth increase. Also, when the ratio of the deposition depth (into part) to part thickness becomes too large, previously deposited layers can re-melt. A too small ratio results in less adhesion between adjacent layers. Furthermore, increasing the powder feed rate decreases the depth of melt pool.

The melt pool shape also strongly depends on the traverse speed. The melt pool becomes elongated at higher travel speeds and penetrates less into successive layers, thus impacting the HAZ. The melt pool length and temperature increase with laser power or slower traverse speeds, while the cooling rate at the liquid/solid interface decreases [12]. Higher substrates temperatures correspond to longer melt pools with little effect on the temperature profile. The melt pool length decreases as the gas heat transfer coefficient increases. Although the melt pool will elongate as the traverse speed increases, the depth of the melt pool will decrease. However, there is a slight dependence of the melt pool depth with traverse speed. For a given laser power and powder feed rate, a specific melt pool depth can be achieved with two traverse speeds, and this is due to the parabolic dependence of melt pool depth on traverse speed.

The free surface of the melt pool will dictate the deposited layer cross-sectional profile. This liquid/vapour interface is unstable and in non-equilibrium because of the blown powder mass addition, heat transfer, fluidic motion and previous layer surface roughness/surface quality. As shown in Figure 2.4, the powder injection results in a tilted melt pool profile and the angle of this tilt is related to the deposition layer thickness and melt pool length. Related to multi-track deposition, the morphology of the melt pool becomes more asymmetric in shape, becoming more “tilted”, relative to single deposition. Furthermore, the number of nozzles utilized to accomplish DED will impact the topology of the melt pool, and the tilt angle will become more axi-symmetrical.

3) Solidification: solidification of the melt pool is a mechanism governed by the net heat transfer through the melt pool. This is a very important physical phenomenon because if it is inefficient and it is coupled with the existence of parasitic phenomena such as entrapped gas or debris, it can lead to porosity in the DED-fabricated parts. In fact, the lack of effective fusion between successive layers can lead to porosity and can occur due to lack of sufficient laser

power, typically at the beginning of a track deposition since this region has undergone more cooling relative to other regions. Porosity can be affected by un-melted particles that are more likely to be present in the first/second deposition layers near the substrate because of the large amount of heat traveling to the substrate in the early phases of DED [4].

Solidification can be classified into three major classes: 1) heterogeneous nucleation, 2) mushy-zone heat/mass transfer, 3) microstructural evolution via heat treatment. As shown in Figure 2.4, the mushy zone is the region between the melt pool and the solid material and it is a two-phase mixture, with remnants of solid particulate and molten metal. The mean of heat transfer in this region is the natural convection, as the density variation is significant. The mushy zone is a result of melting and solidification occurring over a finite temperature range, between the solidus and liquidus temperature.

The solidified microstructure is strictly related to the cooling rate, that is the temperature change of the melt pool during time and changes along the volume of the melt pool, being the highest at the solid-liquid interface and decreasing with distance from the centre of the melt pool. It will depend on the heat loss and conduction heat transfer through parts. The cooling rate, at a given location near the melt pool, can be calculated by multiplying the temperature gradient at the liquidus isotherm, $\nabla T\_i\ (r,t)$, with the traverse speed, V_{beam}, e.g.:

$$\frac{\delta T}{\delta t} \cong \|\nabla T\_i\ (r,t)\| \cdot V_{beam} \tag{2.3}$$

There is also an empirical form for the cooling rate that can be used to estimate the solidification heat transfer. Zheng et al. found a correlation, e.g.: $\lambda_2 = A(C_R)^{-n}$, where λ_2 is the dendrite arm spacing (DAS), C_R is the cooling rate and A and n are material constants [17].

In particular, the solidified microstructure depends on local solidification rates within the melt pool, the ratio of cooling rate to thermal gradient R, and the temperature gradient at the solid-liquid interface, G. Two critical solidification parameters are the ratio G/R, which affects the solid-liquid interface shape, and the cooling rate $G \times R$, which affects microstructure dimensions. Different G and R values may result in three major structure morphologies within DED parts: columnar (elongated grain morphology), columnar-plus-equiaxed and equiaxed (isotropic grain morphology). It has been found that a higher solidification rate promotes the transition from columnar to equiaxed grain morphologies and that increasing the cooling rate leads to a finer microstructure. The tendency to form a columnar structure increases by increasing the ratio G/R, while decreasing G/R is favourable for equiaxed structures [18].

As the melt pool cools very rapidly because the melting temperature of a metal is almost two orders-of-magnitude higher than that of the surrounding inert gas and environment, this can lead to the production of a very fine grain structures, that is dendritic morphology characterized with low DAS. Dendritic arm spacings are on the order of 1-10 µm and depend on the DED process parameters and material used. As shown in Figure 2.8 (a) and (b), increasing the traverse speed increases the cooling rate which results in a microstructure with lower characteristics DAS and the introduction of cellular-type growth. A DED process that provides for low power and smaller melt pools will result in smaller-DAS, finer micro-structural parts.

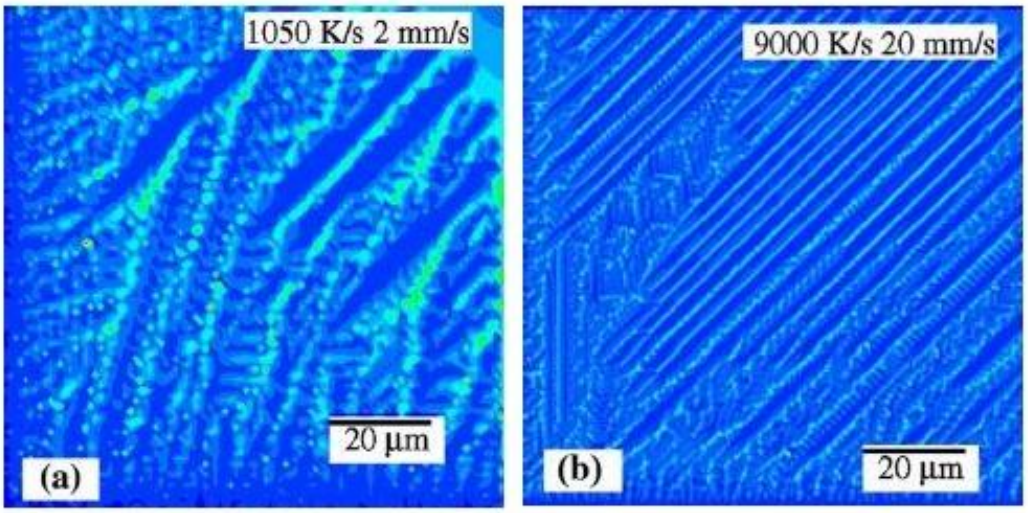

Figure 2.8: EBSD images showing the effect of traverse speed on the simulated HAZ-vicinity cooling rate and microstructure of a carbon-based steel: **a)** traverse speed = 2 mm/s, **b)** traverse speed = 20 mm/s [19].

In order to predict the microstructures inherent to solidification, it is also necessary to model the nucleation and growth of all possible phases. When the melt pool solidifies, the previously deposited layers behaves as a heat sink and this results in directional solidification. The grains or solid-phase columnar fronts move in a direction opposite to the heat flux vector at a specific velocity. The solidification velocity is related to the laser travel velocity and melt pool morphology, while the melt pool thermal gradient is related to the laser power and established temperature field in the part/substrate. Since the thermal gradients are high for laser processing, the exact position of liquid/solid interfaces can be neglected. Variation in the melt pool shape due to powder addition and surface wetting will affect dendritic growth direction and can also affect the solidification velocity. The strong thermal gradients in the melt pool give rise to natural convective flows that can be turbulent and impact solidification. Un-melted powders will behave as nucleation sites within the solidifying melt pool. The observed microstructures within a part fabricated via DED will be helpful in order to understand the solidification heat flux vector direction during DED. For example, the presence of directional columnar microstructure is indicative of unidirectional heat flux in the height-wise direction

4) Conduction heat transfer: in the proximity of the melt pool and mushy zone exists a region of very high temperature and heat transfer relative to the environment of the part called 'heat affected zone' (HAZ). HAZ consists of substantial temperature gradients as a result of the laser-initiated melt pool, phase-change heat transfer and surrounding environment. Sensible (conduction) heat transfer occurs within the HAZ in pre-deposited layers, while latent heat transfer occurs within the mushy zone and re-melting can occur for very high laser powers. The depth of the HAZ can be related to the penetration depth, and it can be seen as a function of part height, power and temperature.

The repetitious passing of the laser over a solid region of the part leads to 'thermal cycling' effect, characterized by localized temperature field disturbances with sharp temperature increases, instant high cooling rates and then modest-to-low cooling rates. In this way, the average temperature of the part can increase with time depending on the thermal mass of the part and substrate and the time between layer deposits. This temperature behaviour can

cause heat treatment or solid state transformations, which then leads to microstructural evolution and thermomechanical interactions, such as residual stress formation.

Ultra-high heat fluxes on the order of 500 kW/cm^2 are easily achievable during DED and they are responsible for initiation and sustainment of the melt pool and HAZ, as well as the temperature gradients within them. Higher heat fluxes increase the dimension of the HAZ and the bulk part temperature field. In order to accurately predict HAZ temperatures, analytical and numerical models can be used, but all the idealizations and assumptions must be integrated to solve the DED/HAZ problem. The dimension of the HAZ is typically minimized in order to reduce the tendency of re-processing/re-melting previously deposited layers, resulting in microstructure evolution.

Due to temperature gradient between the melt pool and the substrate, conduction heat transfer through the part thickness occurs, as well as convective/radiative heat loss occurs simultaneously because of the temperature difference between the part and the environment. Considerable temperature gradients in the part can result in thermal deformation and the rise of residual stress because thermal strains are developed between successive layers due to anisotropic shrinkage in deposition layers. This also leads to stress gradients resulting in part warping and distortion.

The initial temperature, thermal capacitance and size of the substrate in which the part is built atop can have a very important impact on its temperature history and microstructure. During DED, the temperature difference between the melt pool and substrate provides for conduction heat transfer, which results in cooling of the melt pool and HAZ. In this way, the non-thermally controlled substrate behaves as a heat sink, especially during initial layer deposits where heat transfer to the substrate is fundamental. The initial temperature of the substrate, if it is not preheated to a temperature closer to the melting temperature of the material, can have a substantial influence on microstructure in proximity of the substrate since the thermal gradients during the first deposit layer can be significant. Preheating the substrate is useful to reduce residual stress and risk of cracking and thermal distortion, but it leads to lower bulk cooling rates limiting the achievable phase transformations and possibility for microstructural refinement. Sometimes, partial re-melting of the substrate is done to ensure uniformity between the substrate/part microstructure, especially in cladding processes.

Thermal monitoring is the most common method for monitoring laser-based processes, given the direct coupling of metallurgical bonding and heat transfer. In this method, the outer-surface temperature field of a part is observed over a region or its entirety during processing. For DED, this temperature distribution is very important because it gives information regarding the cooling rates, thermal gradients near the HAZ and part, which are all related to microstructure. The temperature and shape of the melt pool atop the part during DED is also indicative of part and layers integrity.

2.1.3 Process parameters

The DED process consists of various operating/process parameters that are set, monitored and/or controlled to ensure part quality and build success. The most important and controllable operating parameters that affect the thermal history and microstructure include: powder feed rate, laser power, laser/substrate relative traverse speed and laser scanning strategy. Such operating parameters are material-dependent and can be altered for a given material to control

structural quality, functional-grading or porosity. As discussed in the previous section, these parameters affect the melt pool shape and incident energy, and consequently, the cooling rate and local thermal gradients.

The laser/substrate relative traverse speed effectively dictates the length of time DED takes for a given part geometry and is typically on the order of 1–20 mm/s. The laser scanning pattern is set by the operator and dictates the laser position and height-wise positioning of the substrate via CNC. The laser power is the total emitted power from the DED laser source. This power is typically on-the-order of 100–5000 W while the beam diameter is on-the-order of 1 mm [9].

The combination of higher traverse velocity and lower laser power results in lower incident energy at the top of the part, typically resulting in finer microstructures due to the higher cooling rates. In contrast, lower cooling rates and coarser microstructures can be achieved by decreasing the traverse speed and increasing the laser power. Lower incident energy, due to laser attenuation and radiation effects, tends to result in finer equiaxed structures, while higher incident energy generally results in columnar grains and coarser microstructures [18].

Powder feed rate has a direct impact on the distribution of powder density in the melt pool, and thus layer height and microstructures during DED. Liu and Dupont demonstrated a linear increase in the layer height as the powder feed rate increases [20]. For a fixed powder feed rate, the amount of powder that is injected into the melt pool varies for different scanning directions because of the distance between the powder stream and laser spot. As shown in Figure 2.9, the powder injection point may be ahead or behind the laser spot, depending on scanning direction. This can result in a highly asymmetric melt pool, impacting the boundary and solidification heat transfer [21]. The relative locations between the powder injection point and laser beam, that is the quantity of powder melted, affects the amount of powder injected into the melt pool.

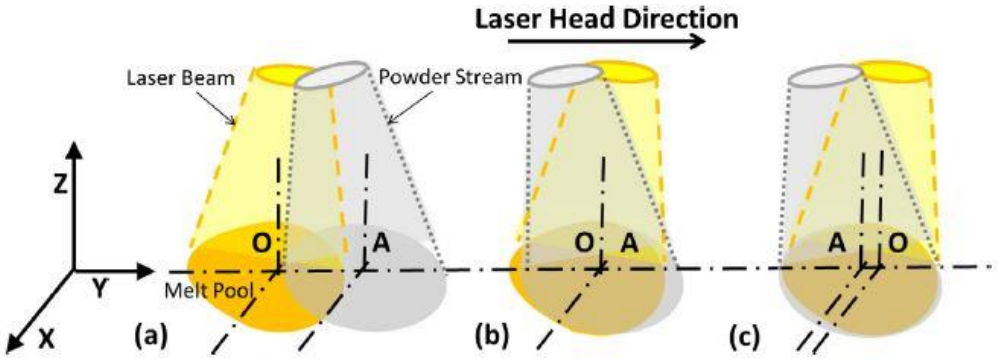

Figure 2.9: Powder injection point, A, **a)** ahead of, **b)** in-line with and **c)** behind the laser spot centre, O [21].

The shadow area shown in Figure 2.9 represents the overlap between the powder stream and laser irradiation area. It can be noticed that the overall shape of the melt pool is elongated and has no rotational symmetry. When the powder injection point A is ahead of the laser spot O, the amount of powder injected into the melt pool is less than the case in which the powder injection point is behind the laser spot. This is due to the fact that in the second case the overlap between the powder stream and the laser irradiation area is bigger than the overlap in the first case, that is the melt pool is bigger.

In order to maintain a constant deposited mass flow rate, the powder feed rate and laser scanning velocity can be set based on scan direction and the distance between laser beam and powder nozzle. However, nowadays there are no quantitative studies that suggest the optimal

control parameters, such as levels of powder feed rate and laser scanning velocity, because of the complexity associated with the physics and the dynamics of the DED process.

As far as the laser scanning strategy is concerned, there are four common deposition patterns (raster, bi-directional, offset and fractal patterns) for use in AM [22]. In addition to these deposition patterns, more 'offset-patterns' can be used by indicating direction, such as offset-out and offset-in. These offset patterns depend on the starting point of deposition, as shown in Figure 2.10.

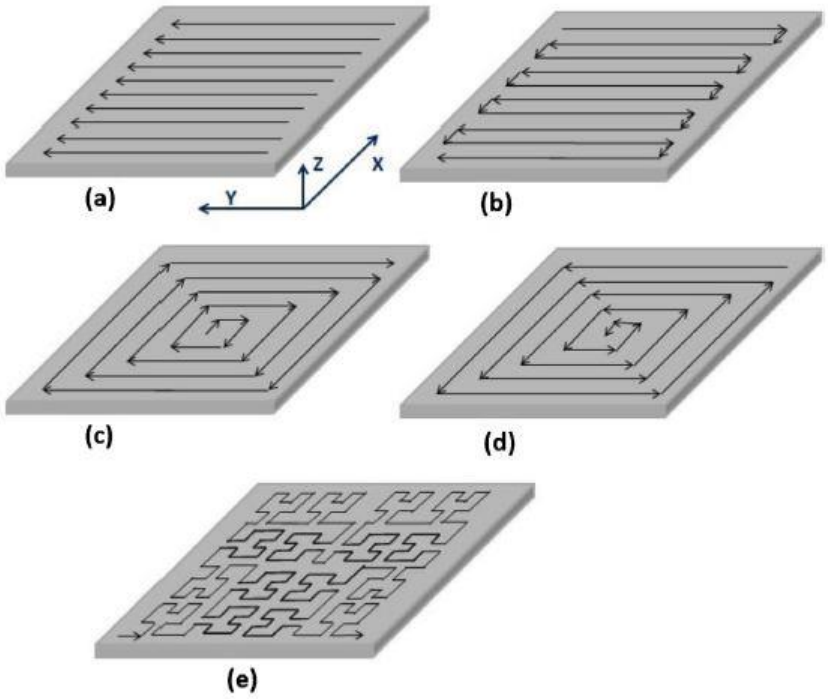

Figure 2.10: Different deposition patterns: **a)** raster, **b)** bi-directional, **c)** offset-out, **d)** offset-in and e) fractal [6].

Different deposition patterns significantly affect the geometric and mechanical properties of the fabricated parts. Choosing the right scanning pattern reduces the production of residual stresses and any thermal distortion. The raster pattern is the most commonly used deposition pattern because of its ease of implementation. As indicated in Figure 2.10, the laser scanning path of the raster pattern does not depend on the shape of the fabricated part, and thus can be implemented to fabricate a variety of parts.

Nickel et al. studied the effects of the raster, offset and fractal deposition patterns on the geometric accuracy of the steel fabricated part [23]. They noticed that the fractal and offset-out deposition patterns generate the smallest substrate deformations. Square corners can lead to the offset and fractal deposition patterns causing interior defects; in this way, adopting fractal or offset patterns can produce parts with higher quality.

2.1.4 Process optimization

The mechanical integrity of DED parts depends on the process parameters, which affect microstructural distribution via thermal history. For this reason, it is important to optimize the DED process parameters to produce near-net-shaped parts with minimal defects. Optimal process parameters are typically determined via experiments, which usually require high experimental costs and time investment. Therefore, it is challenging to develop a

comprehensive and general methodology for DED process optimization because many interacting process parameters are involved.

To solve this issue, one possibility is to reduce the dimension of process models by grouping parameters, typically in dimensionless form. Possible choices of dimensionless parameters are melting efficiency, deposition efficiency, process efficiency, laser absorptivity, specific energy and others [11]. The advantage of using dimensionless parameters is that these parameters are usually defined based on DED processes, instead of materials to be processed. In this way, when a material is to be processed, dimensionless parameters can be used to identify the range of parameters in which good metal parts are formed. Peng et al. [12] studied nickel alloy and utilized specific energy, a dimensional parameter grouping of the laser power, traverse speed and laser diameter, e.g.:

$$\text{Specific Energy} = \frac{\text{Laser Power}}{\text{Laser Scanning Speed} \times \text{Laser Diameter}} \tag{2.4}$$

The specific energy is an important parameter for quantifying many laser processes for sufficient bonding strength and joint/layer resistance to collapsing.

Another possibility is the use of 'process maps', a methodology particularly useful for optimization due to its adoption of dimensionless parameters [24]. These plots have non-dimensionalized ordinates to help in determining effects related to changing scan rate, part preheating and laser power, and are generalized based on analytical, numerical or experimental results. Process maps can be a very useful tool and help DED users in identifying the appropriate process parameters for a given material for fabrication via DED.

Process maps have been developed for predicting the steady state melt pool size in parts for any practical combination of DED variables. Beuth et al. [24] demonstrated how the normalized melt pool length (l) varies as a function of normalized distance travelled by the laser (X), as shown in Figure 2.11.

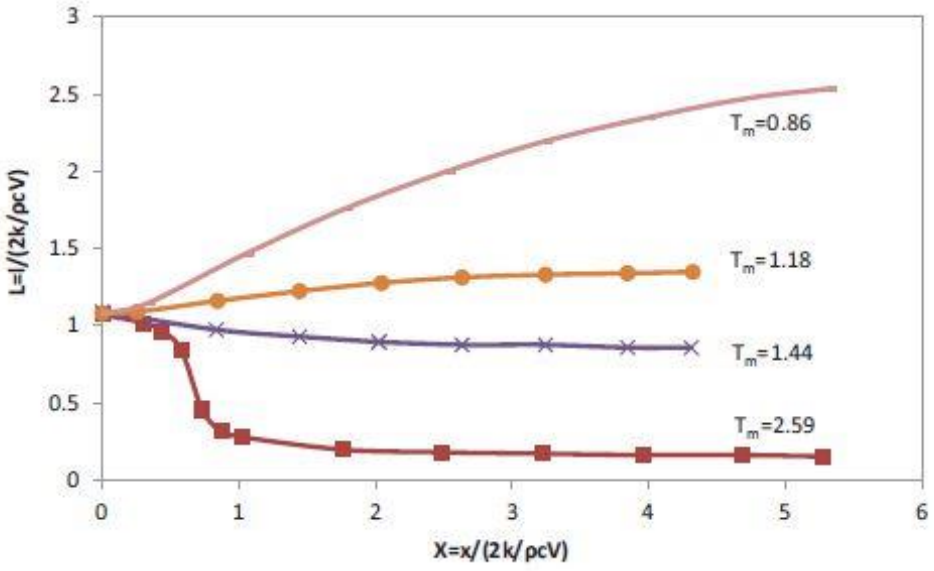

Figure 2.11: Normalized melt pool length (L) versus normalized distance from the location of a step change in laser power (X) for a thin-walled structure for various, normalized melt pool temperatures T_m [24].

Each curve represents a process map of corresponding melt pool temperature T_m. The vertical gaps between two curves represent changes in the (normalized) melt pool length when the melt pool temperature changes due to various DED dynamics. The horizontal gaps indicate the (normalized) distance needed to be travelled by the laser to obtain constant melt pool length when the melt pool temperature changes, which can be converted to the laser travel time by dividing by the traverse speed. These results can be used to determine, in general, how to modify process variables in order to obtain an ideal melt pool size, control maximum residual stresses and control microstructure.

However, there also exist two major limitations in the existing process map methods. First, process maps are for limited part shapes, developed for thin-wall and bulk shapes only. This method does not hold for other common shapes, let alone parts with complex geometry. However, one promising application of AM is to fabricate parts whose geometry is so complex that they cannot be produced using traditional manufacturing methods. For this reason, in order to make process maps useful in manufacturing applications, future work is needed to develop process maps that are representative for the thermal behaviours and mechanical properties of parts with various shapes. Secondly, process maps do not consider temperature-dependent material properties because material properties are idealized as being independent of part temperature. This assumption may not be a realistic one in real world applications, in fact process maps are used to approximate the fabrication process when the temperature remains in a certain range.

2.1.5 Mechanical characteristics

Post-manufacture characterization of parts is a very important procedure for many manufacturing processes, because it allows one to evaluate if a material or a part is suitable for its usage. In order to evaluate the mechanical performance of a part, there are different mechanical tests, such as tensile, hardness, fracture toughness, impact resistance and fatigue.

The tensile test is a common mechanical test for measuring properties related to material monotonic strength. Tensile properties and hardness of DED parts are usually equal to or greater than those of wrought and cast materials because of high cooling rates that lead to fine microstructures. Tensile properties of various laser-produced and wrought materials are listed in Table 1 [18].

Table 1: Comparison of the tensile properties of materials formed by DED and their wrought counterparts at room temperature [18].

Alloys	Ultimate stress (MPa)		Yield stress (MPa)		Elongation to failure (%)	
	Wrought	DED	Wrought	DED	Wrought	DED
316 SS	586	758	234	434	50	46
316L SS	480	540-560	170	330-345	40	35-43
404L SS	…	655	176	324	55	70
AISI H-13	1725	1703	1448	1462	12	1-3

CPM-9V	…	1315	…	821	…	>2
Ti-6Al-4V	931	896-1000	855	827-965	10	1-16
TC-18	1157	1147-1188	1119	1095	14	4.5-5.75
IN-718	1379	1400	1158	1117	20	16
IN-625	834	931	400	614	37	38
IN-600	660	731	285	427	45	40
IN-690	725	665	348	450	41	49
IN-738	1095	1200	950	870	6.5	18

As shown in Table 1, the yield and the ultimate tensile strength of DED parts are higher than those fabricated from wrought materials in most cases, while the elongation-to-failure is typically lower for DED parts and this can be attributed to micro-porosity and oxide inclusions within the parts.

The part's building orientation during DED affects the resultant tensile properties of the part. For example, as shown in Figure 2.12, Shamsaei et al. [6] demonstrated that specimens deposited in the direction along (e.g. parallel to) the length of the tensile samples (e.g. X direction) typically exhibit higher tensile strength than those with layers deposited perpendicular to their length (e.g. Y or Z direction). This anisotropic behaviour can be explained by the presence of weak interfacial layers, in Z and Y directions.

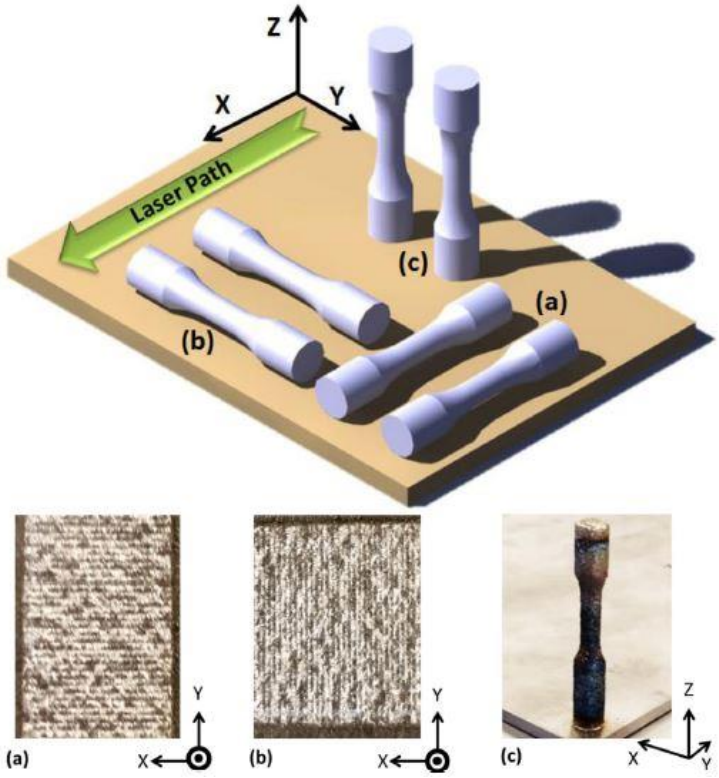

Figure 2.12: Schematic view of a laser-deposited Ti-6Al-4V specimens, **a)** as-deposited surface in the X direction (horizontally oriented), **b)** as-deposited surface in the Y direction (laterally oriented) and **c)** as-deposited surface in the Z direction (vertically oriented) [6].

Different cooling rates for these two deposition orientations may also influence microstructure and mechanical properties. Samples built in the longitudinal direction (X direction) are characterized by a laser passing time between each successive layer which is longer compared to materials built in the Y or Z directions. This difference leads to higher cooling rates and consequently finer microstructures for specimens deposited in the X direction.

As far as fatigue resistance is concerned, fatigue is one of the main failure modes of materials in many applications. During the fatigue process, cyclic damage leads to local cracking and causes fracture after a sufficient number of cycles. Fatigue failure can be characterized by three stages: crack initiation (nucleation), crack propagation and final fracture. Cracks tend to initiate at grain boundaries, inclusions, pores and other microstructural defects.

Microstructural features have a very important influence on fatigue behaviour. Finer microstructures typically exhibit better crack initiation resistance as compared to coarser microstructures, but have a flatter crack path that result in higher crack growth rates. Therefore, materials with finer microstructure usually have less resistance to crack propagation, as compared to coarser microstructures [6].

2.2 AISI 316L Stainless Steel

AISI 316L stainless steel is an austenitic stainless steel which comprises iron alloyed with chromium of mass fraction up to 18 %, nickel up to 14 % and molybdenum up to 3 %, along with other minor elements. It displays high hardness and toughness, high corrosion resistance and high machine-ability. It also has low stress to rupture and tensile strength at high temperature. All these interesting properties make that it has a huge usage in many fields like marine, energy, aerospace and medical environments. Generally austenitic stainless steel parts are manufactured using casting, forging or extrusion, but these technologies do not allow for the preparation of complex parts and the final component must be machined into the final shape. This causes these processes to be time consuming and additionally austenitic stainless steels, such as 316L, are relatively expensive to machine. So the hard and expensive workability of the 316L, along with the spread of its usage and wide availability of relatively inexpensive feedstock for AM, has led to several recent publications that focus on the study of the microstructure and the relationship with the process parameters and the properties of this particular stainless steel obtained by means of DED or AM in general. For example, Ziętala et al [1] studied the microstructure of 316L stainless steel fabricated using a Blown Powder AM process. In particular, they analysed the microstructure of the original metal powder and that of the samples obtained from the AM technique, in order to see how the process had affected the stainless steel microstructure. As shown in Figure 2.13, the metal powder revealed the presence of only a single austenite phase, while the XRD pattern of the AM samples indicated that after the process, austenite and ferrite were present in 316L stainless steel.

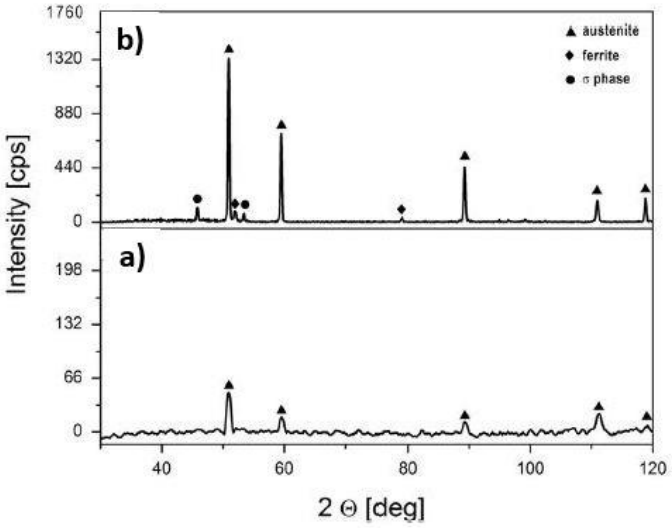

Figure 2.13: XRD patterns of the 316L stainless steel powder a) and the 316L stainless steel samples obtained using the LENS technique b) [1].

The presence of austenite and ferrite was confirmed by the experiments performed by Takalo et al. [2] that the austenitic solidification in austenitic stainless steel welds was related to the composition of the alloy. When the Creq/Nieq ratio was less than 1.48, where Creq and Nieq represent the chromium and nickel equivalents on the Schaeffler diagram shown in Figure 2.14, the welds solidified with the austenite being the primary or leading phase and the delta ferrite, if any, located in the interdendritic spaces. In this study, in order to verify the existence of delta ferrite, the chemical composition of the AISI 316L stainless steel powder (Table 2) was used to calculate the values of Creq and Nieq. The location of the composition of the AISI 316L on the Schaeffler constitution diagram is shown in Figure 2.14. Based on the Cr and Ni content (austenite stabilizing elements) and the Schaeffler diagram, it can be observed that the composition is located inside the ferrite-austenite area predicting a ferritic phase between 0 wt% and 5 wt%.

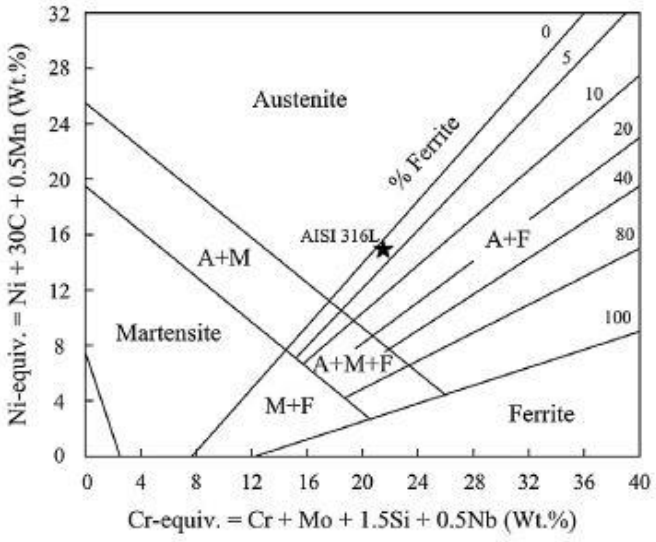

Figure 2.14: Schaeffler constitution diagram showing the composition of the AISI 316L stainless steel powders with a black star [2].

Table 2: Chemical composition of AISI 316L stainless steel powder.

Element	C	Cr	Cu	Fe	Mn	Mo	Ni	P	S	Si
wt %	< 0.03	17.5 – 18.0	< 0.50	Bal.	< 2.0	2.25 – 2.50	12.5 – 13.0	< 0.025	< 0.01	< 0.75

Furthermore this result was also confirmed by Rong et al. [4] who worked on T-joint laser welding 316L. They have observed a microstructure where the austenite and ferrites structures were in the weld centre and around the fusion line (Figure 2.15). Another confirmation is given by the work of Huang et al. [5] on Laser beam welding of T-joint. They also found microstructures consist of a large amount of austenite and a small amount of ferrite (Figure 2.16).

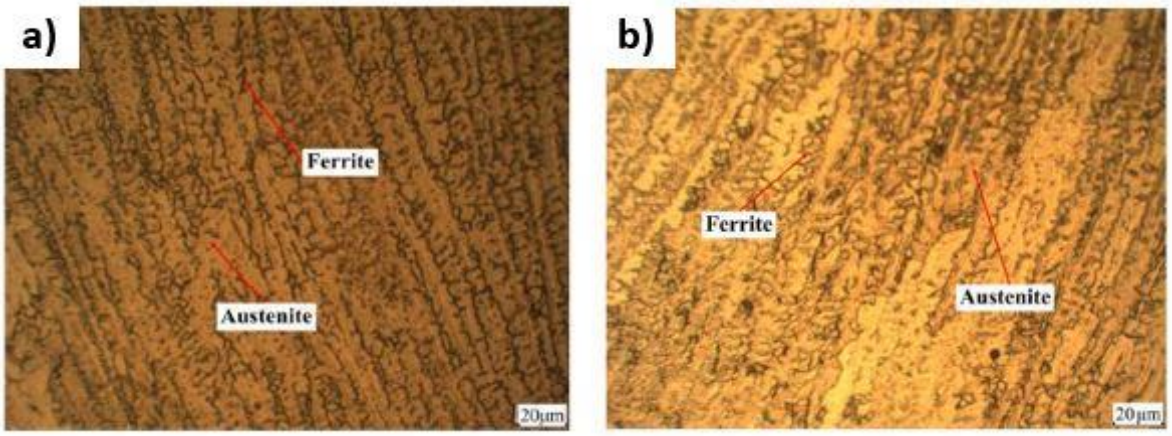

Figure 2.15: Grain growth: **a)** microstructure near the fusion line, 500 X, **b)** microstructure near the middle position of the weld, 500 X [4].

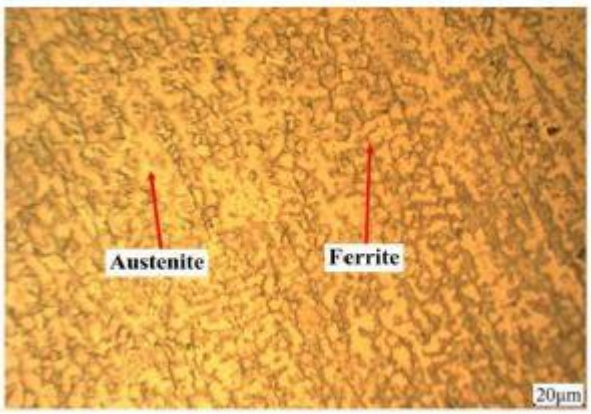

Figure 2.16: Weld zone, 500 X [5].

Another characteristic of the microstructure of the 316L samples built by DED is the presence of sub-micrometer features dispersed throughout the melt pool. Wang et al. [25] worked on 316L obtained by laser powder-bed-fusion (L-PBF) and they found many features rich in O, Si and Mn; they were very small (nanometric size) and observed along the cellular walls, within the ferritic phase (Figure 2.17).

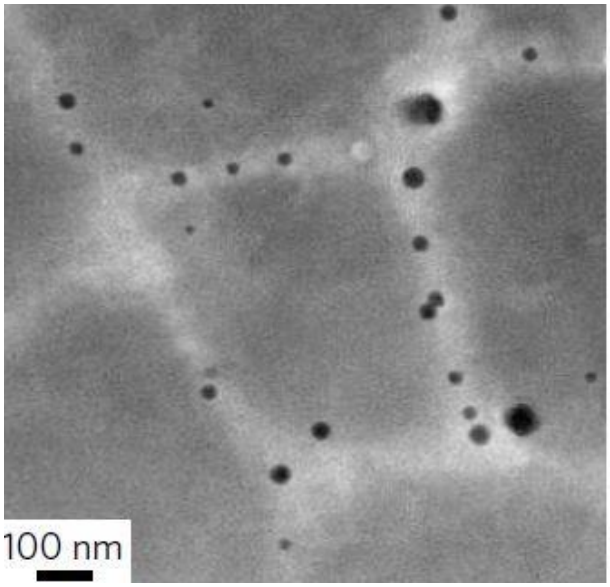

Figure 2.17: Scanning TEM (STEM) image of a solidification cell. The nanoparticles segregated to the cell were identified as transition-metal-rich silicates formed during L-PBF processing [25].

As far as the morphology of the microstructure is concerned, the microstructure of the 316L obtained by means of DED or AM in general, is different from the microstructure of the steel produced with subtractive manufacturing methodologies. This aspect was observed and studied by Rong et al. [4] who found that the microstructure near the fusion line remain equiaxed austenite grains, while a columnar dendritic structure is present within the melt pool near its boundary, as shown in Figure 2.18.

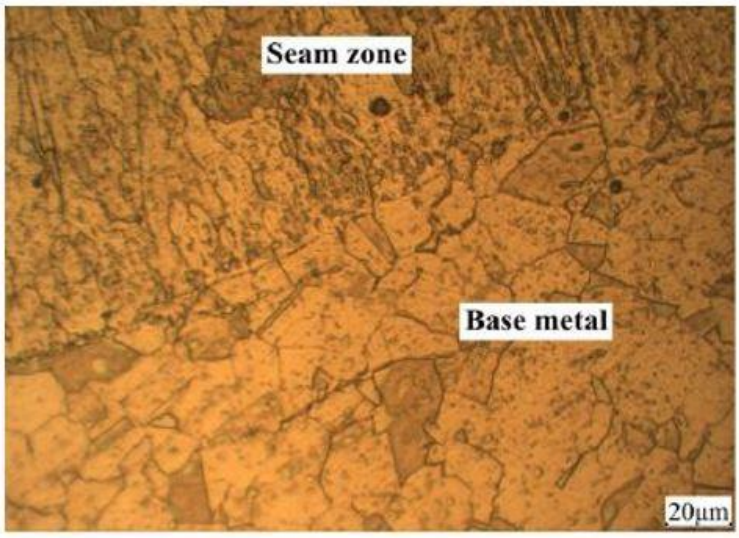

Figure 2.18: Weld fusion line at a magnification of 500 X [4].

Dutta et al. [26] studied the relationship between the DED process parameters and the resultant microstructure of AISI 316L steel. They managed to produce 316L steel parts with a homogeneous microstructure and minimum porosity and they noticed that the morphology of the microstructure depends on the laser parameters, in particular the scan speed. In fact, the grain size was coarsened with decrease in scan speed and the range of grain size (maximum-minimum) was reduced with increasing scan speed. They also found that micro-porosities present in the microstructure could be reduced with increase in scan speed.

Also Pinkerton and Li [27] studied the influence of laser parameters, in particular of pulse frequency and duration, on the microstructure, surface roughness and hardness of 316L stainless steel parts, using a pulsed wave CO_2 laser. They performed tests with both continuous and pulsed laser beams and found that both of them can produce consolidated parts, suitable for functional prototyping and tooling applications, and in both cases the structure is entirely austenitic. In particular, a pulsed laser beam can reduce the porosity obtained using a continuous beam, but low pulse repetition frequencies give coarse layer structure. Surface roughness varies little with pulse frequency, but a better result is achieved with a pulsed laser beam rather than continuous wave mode. Furthermore, they evaluated the hardness of walls of AISI 316L stainless steel which increases with pulse frequency and is generally greater in the middle of the wall than in the upper layers.

Through DED not only improve mechanical properties like hardness, but also other properties such as the corrosion resistance. About this, Yue et al. [28] showed that the laser treatment of AISI 316L steel improves its pitting corrosion resistance. The main reason for this effect is the development of a more homogeneous surface composition and the amount of undesirable precipitates and second phases are reduced.

3. Materials and methods

3.1 Powders

A gas atomized AISI 316L stainless steel powder, produced by LPW Technology Ltd., was used as the starting material of the DED process. Figure 3.1 shows SEM micrographs of the powder at different magnifications and the corresponding chemical composition is listed in Table 2. As shown in Figure 3.1, the particles have a roughly spherical shape and some satellites.

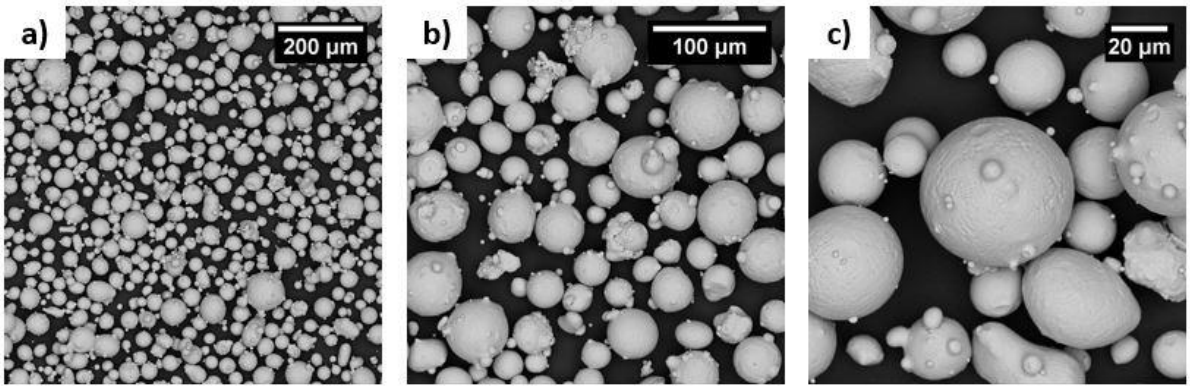

Figure 3.1: SEM micrographs of AISI 316L powder, **a)** 300 X, **b)** 800 X and **c)** 2000 X.

3.2 DED system

The AISI 316L stainless steel samples were fabricated in the SUPSI (University of Applied Sciences and Arts of Southern Switzerland) laboratory (ARM lab – DTI) using a Laserdyne 430 system (Figure 3.2). The Laserdyne 430 is a three axis laser processing system with a vertical movement (Z axis) on the deposition head and a X/Y position speed of 15 m/min. The main characteristics of this machine are listed in Table 3. The laser source is a fiber laser Convergent Photonics CF1000 with a maximum laser power of 1000 W and a wavelength of 1070 nm. The deposition head is an Optomec deposition head with 4 nozzles (multinozzle configuration) and the powder feeder is an Optomec powder feeder too. All samples were built using argon of purity 4.6 as shielding and carrier gas, using a carrier mass flow of 4 l/min.

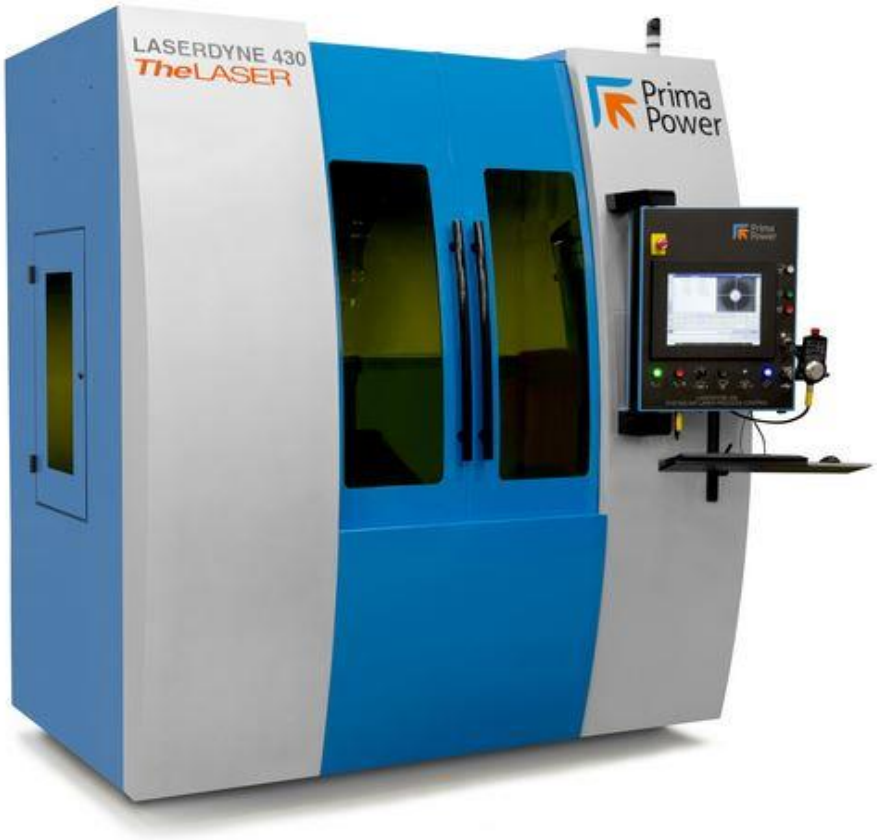

Figure 3.2: Laserdyne 430 [29].

Table 3: Basic system specifications of a Laserdyne 430 machine [29].

Travel	*X axis* *Y axis* *Z axis* *BeamDirector 3*	585 mm 408 mm 508 mm 900 degrees continuous motion in C axis 300 degrees continuous motion in D axis
Position speed	*X and Y axes* *Z axis* *BeamDirector 3*	15 m/min 15 m/min 0 – 90 rpm
Accuracy	*X, Y, Z axes* *BeamDirector 3*	12.5 µm bi-directional ± 6 arcseconds
Resolution	*BeamDirector 3*	0.0005 degree
Repeatability	*X, Y, Z axes* *BeamDirector 3*	12.5 µm bi-directional within 6 arcseconds
Minimum programmable increment		2.5 µm
Table Load Capacity		250 kg

3.3 Samples

The samples analyzed in this work have been realized on rectangular AISI 316L baseplates, with a size of 150x80x8 mm and have two different geometries:

- spirals: circular layers with different track overlapping: 30 %, 50 %, 70 % (variable width and height) on Baseplates 3 and 4 (Figure 3.3);
- circles: circular tracks with a diameter of 3, 9 and 15 mm (variable width and height) on Baseplates 5 and 6 (Figure 3.4).

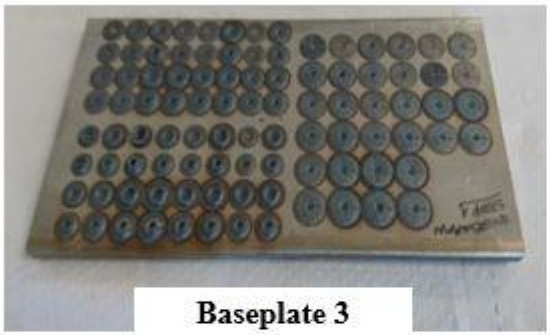

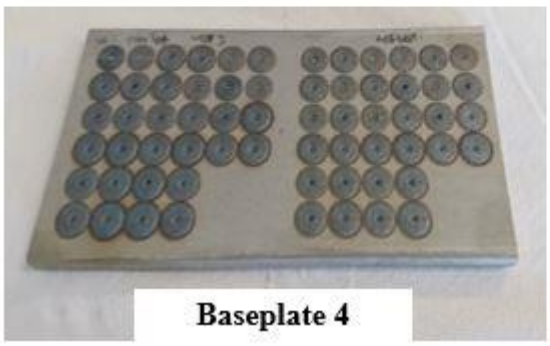

Figure 3.3: Image of the Baseplates 3 and 4 with spirals.

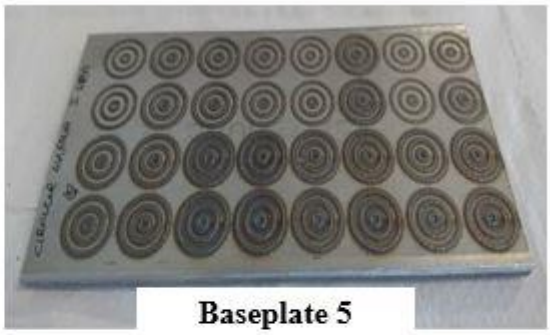

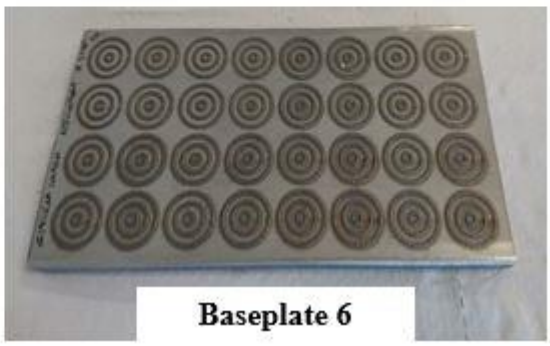

Figure 3.4: Image of the Baseplates 5 and 6 with circles.

As far as the spirals are concerned, five concentric overlapping circles were built varying power (*P*), scan speed (*F*), overlapping and scanning strategy, while in the case of circles, three concentric non overlapping circles were built changing power, speed and strategy, as well. The S1 strategy starts from the internal circle and moves to the external one, while the S2 strategy starts from the external circle and moves to the internal one.

Among all the samples on the baseplates, those with the most interesting combination of building parameters were selected in order to analyse the effect of heat accumulation and the relationship between the process parameters and the microstructure. The main building parameters used for the production of these samples are listed in Table 4 and 5, for the spirals and the circles respectively.

Table 4: Building parameters used for spirals.

n.	P [W]	F [mm/min]	G [g/s]	Strategy	Overlap
P3_1	300	450	0.0415	S1	50 %
P3_2	300	450	0.0415	S2	50 %
P3_3	600	450	0.0415	S1	50 %

P3_4	600	450	0.0415	S2	50 %
P3_5	300	450	0.0415	S1	70 %
P3_6	300	450	0.0415	S2	70 %
P3_7	600	450	0.0415	S1	70 %
P3_8	600	450	0.0415	S2	70 %
P4_1	300	450	0.0415	S1	30 %
P4_2	300	450	0.0415	S2	30 %
P4_3	600	450	0.0415	S1	30 %
P4_4	600	450	0.0415	S2	30 %
P4_5	150	200	0.0415	S1	30 %
P4_6	150	200	0.0415	S2	30 %
P4_7	350	500	0.0415	S1	30 %
P4_8	350	500	0.0415	S2	30 %

Table 5: Building parameters used for circles.

n.	P [W]	F [mm/min]	G [g/s]	Strategy
P5_1	300	450	0.0415	S1
P5_2	300	450	0.0415	S2
P5_3	600	450	0.0415	S1
P5_4	600	450	0.0415	S2
P6_1	150	200	0.0415	S1
P6_2	150	200	0.0415	S2
P6_3	350	500	0.0415	S1
P6_4	350	500	0.0415	S2

3.4 Characterisations

3.4.1 Microstructural characterisation

In order to analyse the microstructure, the samples were cut along the XZ plane and both samples and powders were cold mounted using ClaroCit resin and polished to 1 µm. Then they were etched with different reagents in order to find the best chemical etchant to highlight the microstructure. The following etchants were used:

- Aqua regia (15 ml HCl, 5 ml HNO_3, 100 ml H_2O), immersion for 60 s and 120 s;
- Modified Aqua regia (HCl, HNO_3, CH_3COOH), immersion for 5 s, drop for 10 s, wad for 10 s;
- Electrolytic etching (H_3PO_4, 6V);
- Kalling No.2 solution (HCl, $CuCl_2$, CH_3CH_2OH).

After several tests, the Kalling No.2 solution was chosen in order to etch the samples for 10 seconds. The geometry values of the melt pools were evaluated by means of the Image J software.

In this thesis, the following microscopes were used:

- Optical Microscope Leica DMI 5000 (Figure 3.5), in order to analyze the powder cross section, the size and geometry of the melt pool and the effect of the chemical etching on the microstructure;
- Scanning Electron Microscope (SEM) Phenon XL equipped with a fully integrated electron dispersive spectroscopy (EDS) (Figure 3.6), in order to analyze the powder and samples microstructure and their chemical composition obtained through EDS.

Figure 3.5: Optical Microscope Leica DMI 5000.

Figure 3.6: Scanning Electron Microscope (SEM) Phenon XL equipped with a fully integrated electron dispersive spectroscopy (EDS)

3.4.2 X-rays diffraction

X-Ray diffraction (XRD) analyses were carried out only on fresh and used AISI 316L powders using a PANalytical Xpert^3 system in a Bragg Brentano configuration in a 2θ range between 20 and 100° (operated at 40 kV and 40 mA with a step size 0.013 ° and 30 s per step).

3.4.3 Mechanical tests

Hardness

Micro-Vickers hardness was evaluated using the micro-Vickers indenter Leica VMHT with a load of 100 gf applied for 15 s. The measurements were carried out on the cross section of the samples embedded in the cold resin, concentrating on the melt pool area by making the indentations along the X-axis and the Z-axis of the cross-section. Vickers indentations were measured with the Image J software. In particular, the two diagonal lines of the indentation, d_1 and d_2 (Figure 3.7), were measured and the Micro-Vickers hardness (HV) was calculated using the following formula:

$$HV = (1.8544 \cdot F)/(d_1 \cdot d_2) \text{ [kgf/mm}^2\text{]} \quad (3.1)$$

where F is the force applied in kilograms-force (kgf) and $d_1 \cdot d_2$ is the surface area of the resulting indentation in square millimetres (mm^2).

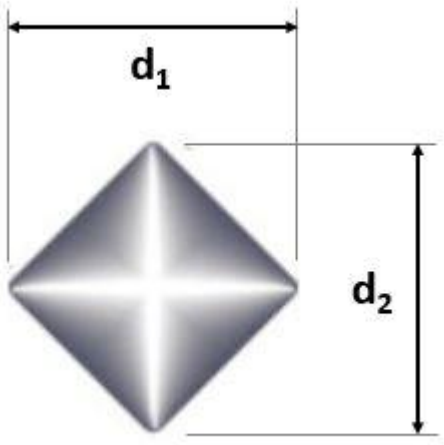

Figure 3.7: Diagonal lines of the Vickers indentation.

Nanoindenter

A Nanoindenter TI950 Nanoindenter (Hysitron) was used in order to analyse the sample hardness at a smaller scale. A diamond Berkovich tip indenter and a controlled load of 2500 μN were used and the test was done by applying and removing the controlled load to the samples. An 11 x 11 grid has been made, with a distance between one indentation and the other of 10 μm in different areas of the scan melt pool.

4.Results and discussion

In this thesis both powders and samples were analyzed. For this reason, the following chapter will be divided into two sections: the first deals with the results obtained by analyzing the AISI 316L stainless steel powders, while the results of the tests performed on the DED samples are shown and discussed in the second section.

4.1 Powder

In order to understand if the residual powder remaining after a DED cycle can be reused for a new process, both new powders and used powders have been analyzed. The main goal was to check if the AISI 316L stainless steel powder retained the original microstructural, compositional and mechanical properties after having faced a DED process.

At first the powders were deposited on an SEM stub and tapped in order to remove the loose particles. Then they were observed at the Scanning Electron Microscope at different magnifications (Figure 4.1 and 4.2). As shown in Figure 4.1, particles of the new powder are characterized by a spherical shape and satellites on the surface, while in the used powder most of the particles have an irregular shape because after melting during the DED process they tend to remelt together by assuming irregular shapes (Figure 4.2). Furthermore, as can be seen from Figure 4.2, also spherical particles are present in the used powder and this is likely because there are un-melted powder particles. Moreover, from these micrographs it is noticed that in the used powder there are no longer very fine particles, which are in large quantity in the new powder. For this reason, it can be said that the size of the new powder particles is smaller than the size of the particles that have already undergone the DED process.

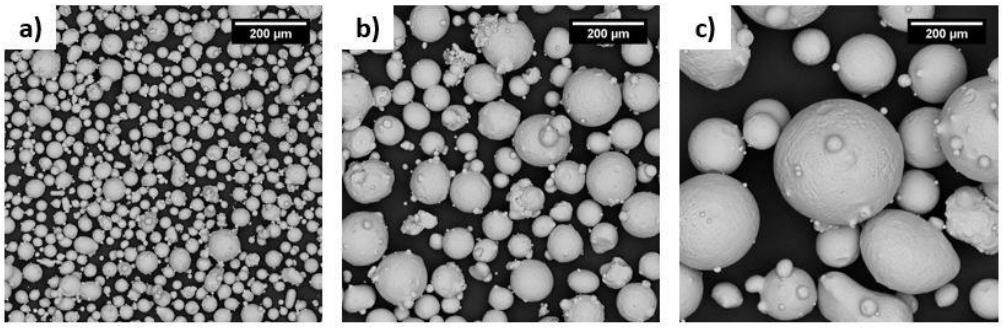

Figure 4.1: SEM micrographs of 316L new powder, **a)** 300 X, **b)** 800 X and **c)** 2000 X.

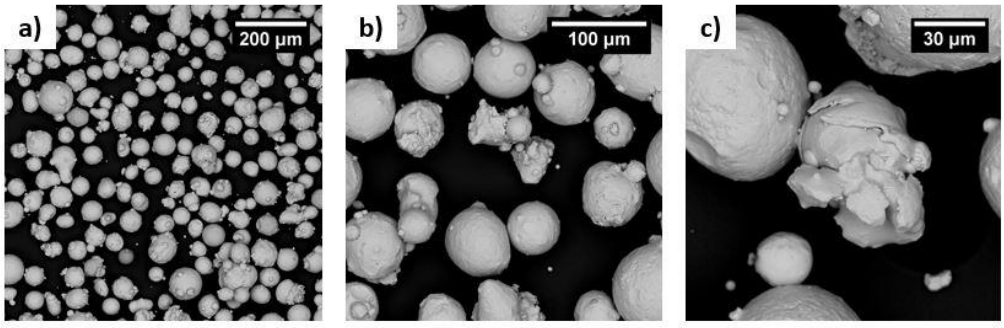

Figure 4.2: SEM micrographs of 316L used powder, **a)** 300 X, **b)** 800 X and **c)** 2000 X.

4.1.1 Particle size distribution

This observation was confirmed by the calculation of the particles size distribution of both powders. Particles size was calculated by means of the image analysis method (in number) and the laser granulometry (in volume) techniques. The result in number gives greater importance to the fine fraction of the particles, while in the volume result larger particles are more important. As far as the granulometry for image analysis is concerned, in order to calculate the particle size distribution, 3 different images of the new powder and used powder were taken using the SEM at the magnification of 300 X. Then, the Image J software was used in order to analyse particles and calculate the values of the diameters. The granulometry result obtained with the image analysis method is shown in Figure 4.3.

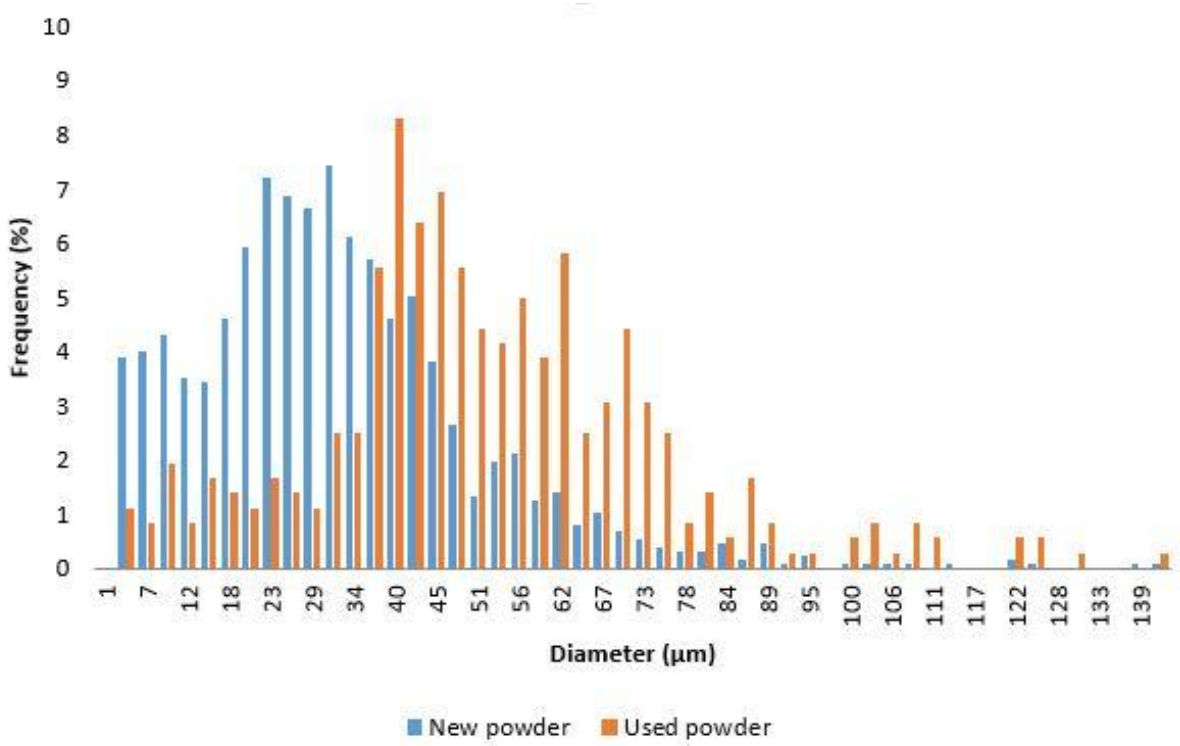

Figure 4.3: Particle size distribution obtained by means of the granulometry for image analysis method (in number).

As shown in Figure 4.3, this number analysis gives a particle size distribution in which the new powder particles diameters are in the range of 10-50 µm, while particles diameters of used powder are in the range of 30-75 µm. Also the laser granulometry confirms that the used powder has particles with a bigger size. The Figure 4.4 shows the particle size distribution obtained by means of the laser granulometry technique and it can be noticed that there is a peak around 95 µm characteristic of used powder particles, while the peak diameter of the new powder particles is shifted to lower values, around 45 µm.

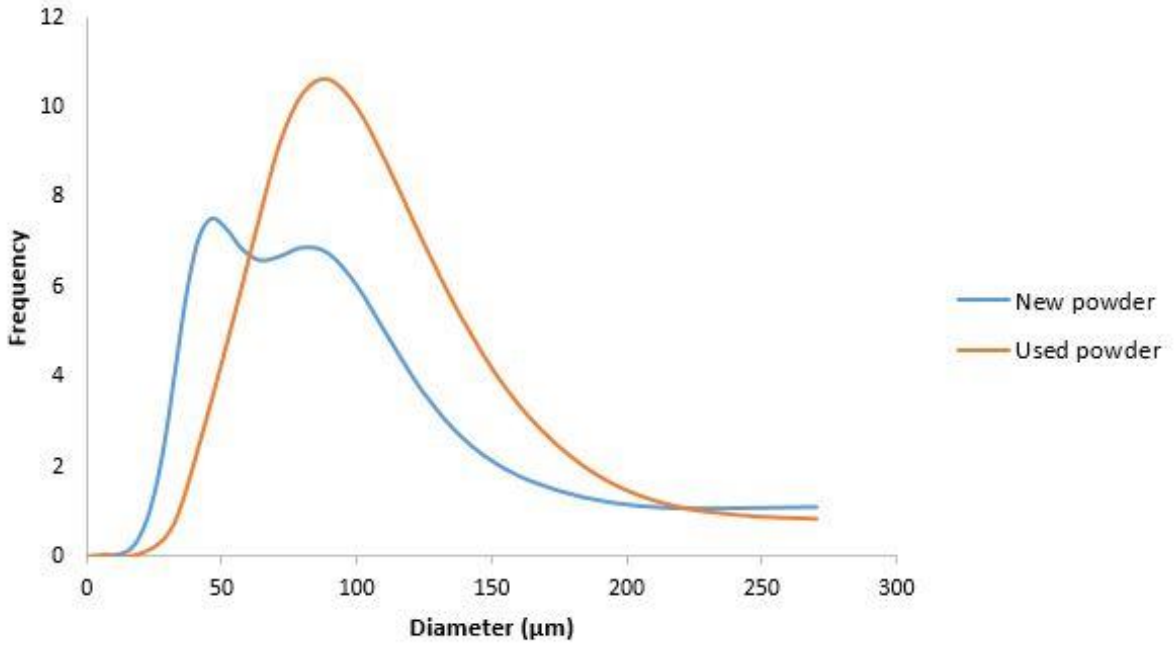

Figure 4.4: Particle size distribution obtained by means of the laser granulometry technique (in volume).

As can be seen from Figure 4.3 and Figure 4.4, when the granulometry for image analysis method is used most of the fine particle may be lost during the powder collection. However, this attention to the fine fraction of particles is not important for this work, so it can be said that the most interesting result is given by the laser granulometry technique.

4.1.2 Porosity

Particle size is not the only parameter that changes between new powder and old powder, but also porosity varies between the two types of powders. Both new powders and used powders were cold mounted using ClaroCit resin, polished on SiC papers with granulations of 500, 800, 1200, 2400, 4000, and with 3 and 1 µm diamond pastes. The mounted powders were observed at the optical microscope and SEM.

Particles porosity was calculated using the Image J software by reference to 10 different images of new powder and used powder taken to the Optical Microscope with at the magnification of 200 X. New powder particles are found to have a porosity of about 0.03%, while particles remaining from the DED process have a porosity, which is about 10 times larger than the porosity of the starting powder, i.e. 0.2%. The small spherical pores found in the new powder were likely to be caused by entrapped gas in the raw 316L stainless steel powder (Figure 4.5), while the porosity of the used powder is characterised by large and irregular in shape cavities, due to the DED process (Figure 4.6).

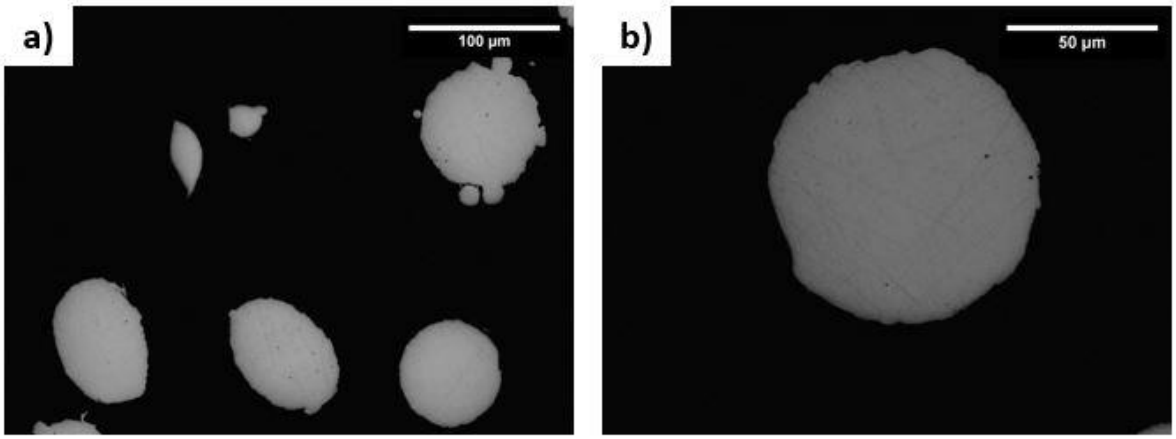

Figure 4.5: Optical Microscope micrographs of 316L new powder, **a)** 200 X and **b)** 500 X.

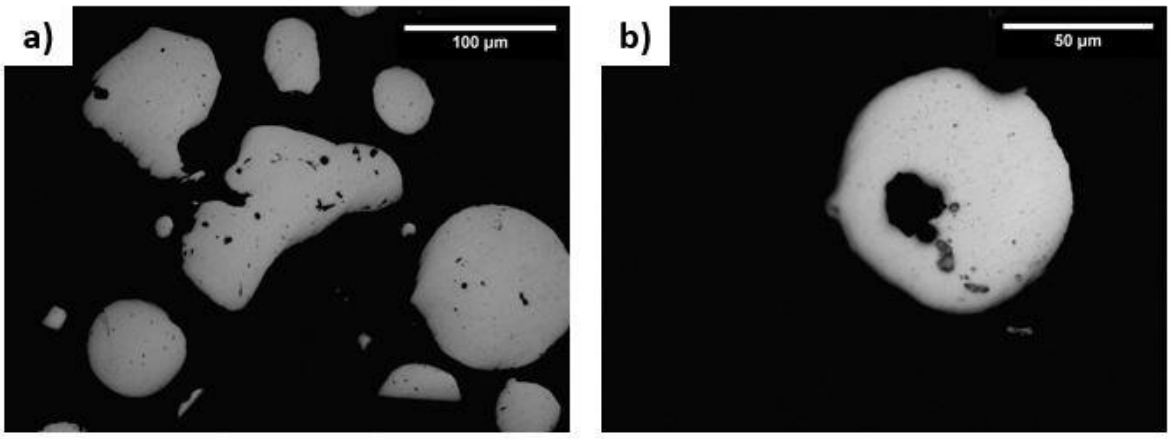

Figure 4.6: Optical Microscope micrographs of 316L used powder, **a)** 200 X and **b)** 500 X.

4.1.3 Microstructure

After having analyzed the shape, size and porosity of the particles, a further difference between the new and the used powder was found in the microstructure, particularly in the phases present. The XRD pattern reported in Figure 4.7 shows that the both powders consist mainly of the austenitic phase, but the used powder has a further peak characteristic of delta ferrite. A similar result was obtained by Ziętala et al. [1] who studied the microstructure of 316L stainless steel fabricated using a Blown Powder AM process (Figure 2.13). It can be seen from Figure 2.13 that there is the same characteristic peak of delta ferrite near the highest peak of austenite phase, which can also be seen in the XRD pattern (Figure 4.7) obtained from the analysis on the used powder done in this work. This is due to the position of the steel in the Schaeffler constitution diagram (Figure 2.14), in which its composition is located inside the ferrite-austenite area predicting a ferritic phase between 0 wt% and 5 wt%.

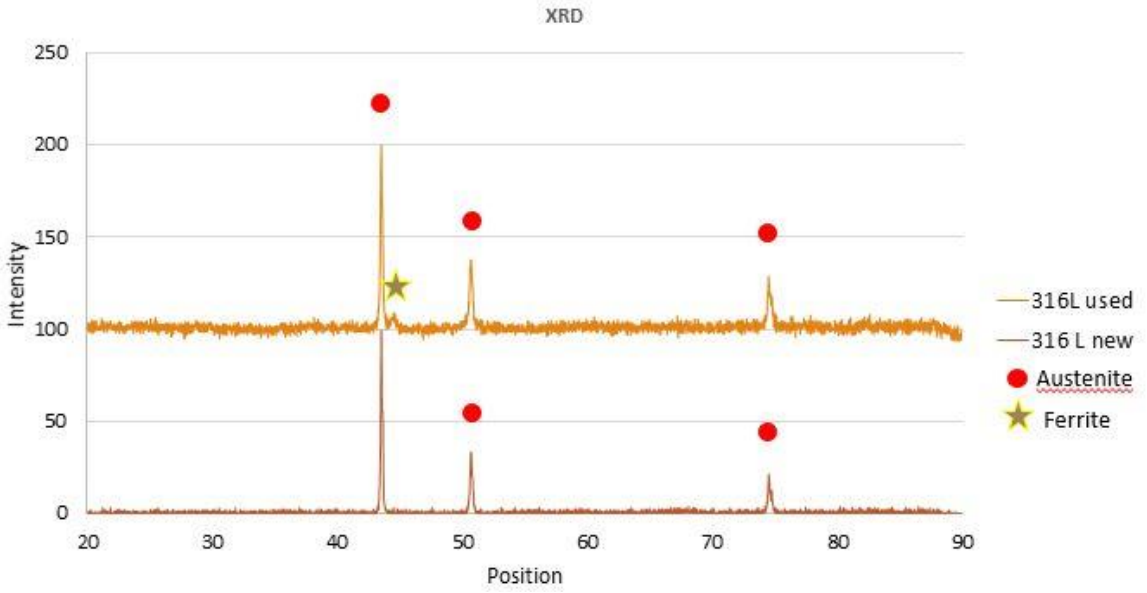

Figure 4.7: XRD patterns of the used and new powder.

Observing carefully both powders microstructure, it have also been detected sub-micrometer features dispersed throughout the surface of powder particles. An EDS analysis was carried out on these features and the results are shown below. It is important to underline that the analysis was conducted on the used powder particles, because the new powder did not have many of these features. Two point analysis were conducted on the dark feature (Figure 4.8 a)) and on the surface of the powder particle (Figure 4.8 b)), then the results in terms of chemical composition detected were compared to each other and also with the chemical composition of the alloy (Table 6). It can be noticed that the dark feature is rich in O, Mn and Si, while the amount of Fe, Cr and Ni decreases. In addition, if the composition of the particle surface without oxygen is considered, this results to have almost the same theoretical composition of the alloy.

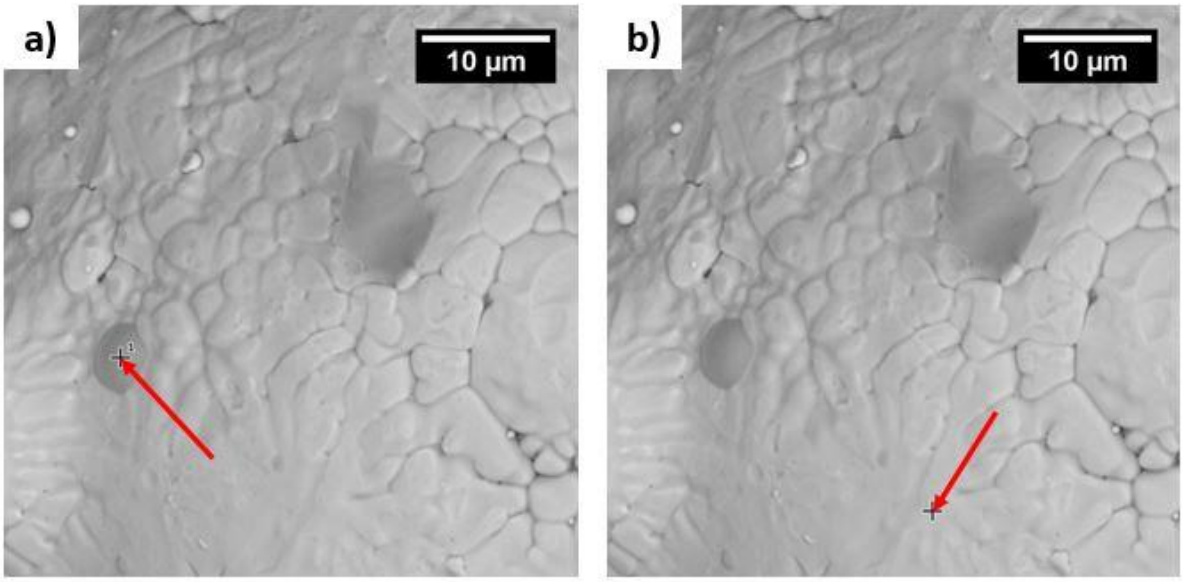

Figure 4.8: SEM micrographs of EDS point analysis, **a)** on the dark feature and **b)** on the particle surface.

Table 6: Chemical composition in %wt of the dark feature, the particle surface, the particle surface without oxygen and the AISI 316L stainless steel powder.

Area	Fe (%wt)	Cr (%wt)	Ni (%wt)	O (%wt)	Mo (%wt)	Mn (%wt)	Si (%wt)
Dark feature	4,19	8,38	1,29	51,86	1,78	18,32	14,18
Particle surface	61,43	15,59	9,27	8,36	3,25	1,14	0,96
Particle surface without oxygen	67,03	17,01	10,12	-	3,55	1,24	1,05
AISI 316L	Bal.	18,00	13,00	-	2,50	2,00	0,75

Then a map analysis was made on a different black feature belonging to another particle of new powder. As shown in Figure 4.9, this analysis also confirms the considerations made before: the feature is composed of O, Si and Mn and is poor in all other elements.

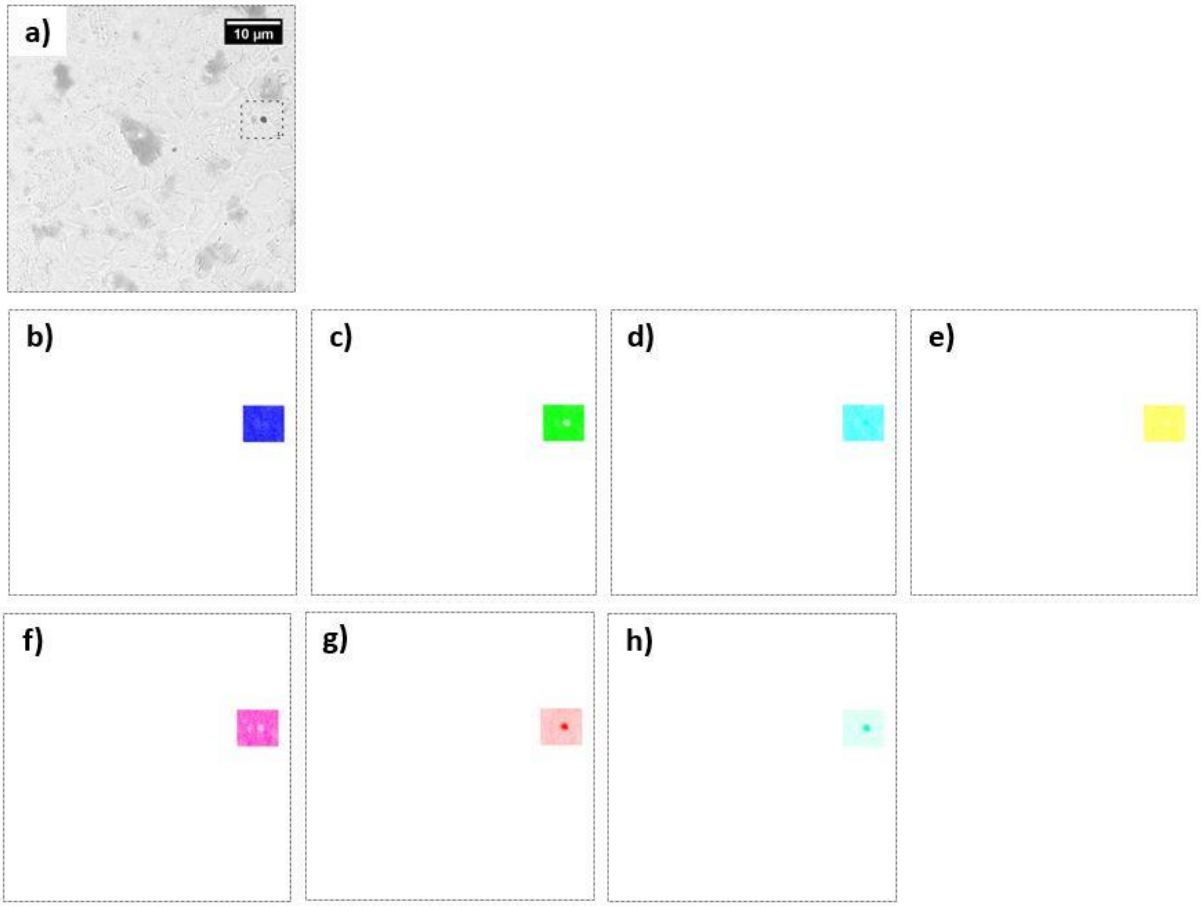

Figure 4.9: Map analysis **a)** on the dark feature and concentration of **b)** Cr, **c)** Fe, **d)** Mn, **e)** Mo, **f)** Ni, **g)** O and **h)** Si.

Finally, two linescan analyzes were conducted on the cross section of other new powder particles so as to intersect the dark features observed on the surface of the particles via SEM. As it can be seen from Figure 4.10 and Figure 4.11, dark features are poor in Fe and Ni, but have a high amount of O, Si and Mn. It is important to note that not all circular dark features

have the above mentioned composition. So probably, some areas that seem to be composed principally of O, Si and Mn from a SEM observation, may actually be micropores probably due to the detachment of the oxide during sample preparation. However, their nature has yet to be further investigated.

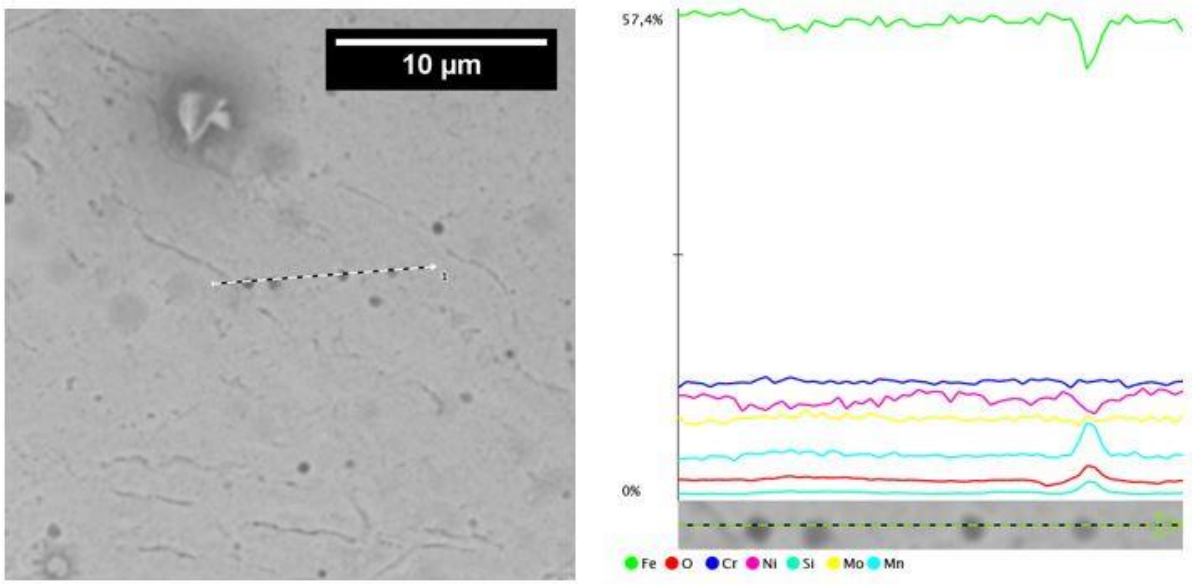

Figure 4.10: Linescan analysis and concentration of Fe, O, Cr, Ni, Si, Mo and Mn.

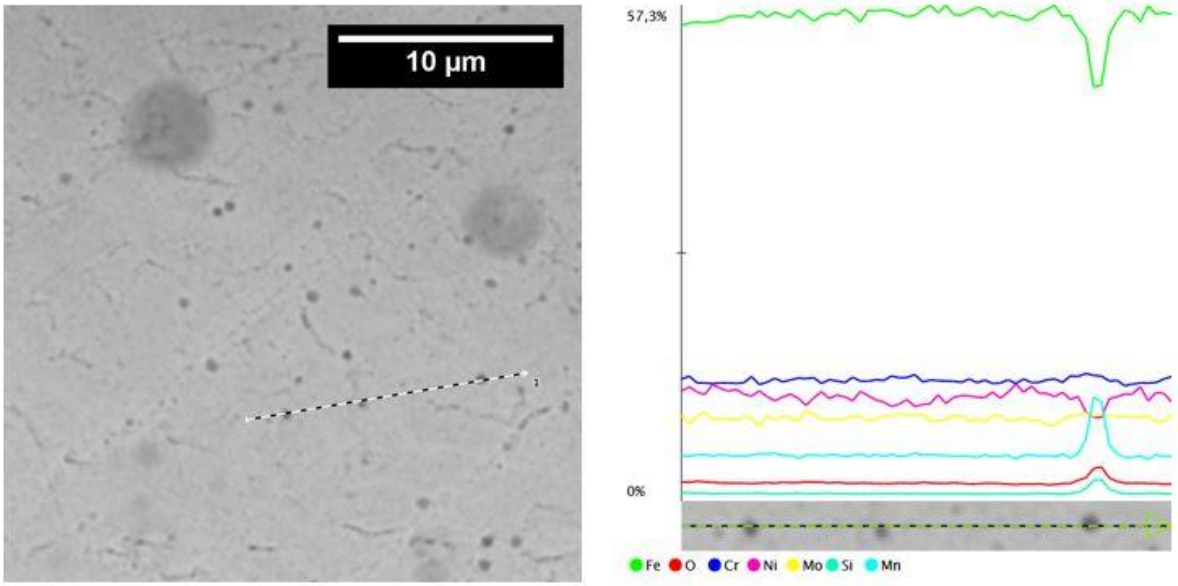

Figure 4.11: Linescan analysis and concentration of Fe, O, Cr, Ni, Si, Mo and Mn.

Similar results were obtained by Pauzon et al. [3] who studied the effect of Argon and Nitrogen atmospheres on the properties of the as-built 316L stainless steel components by Laser Sintering. They found inclusions that have turned to be Mn-Cr-Si surface oxides (Figure 4.12).

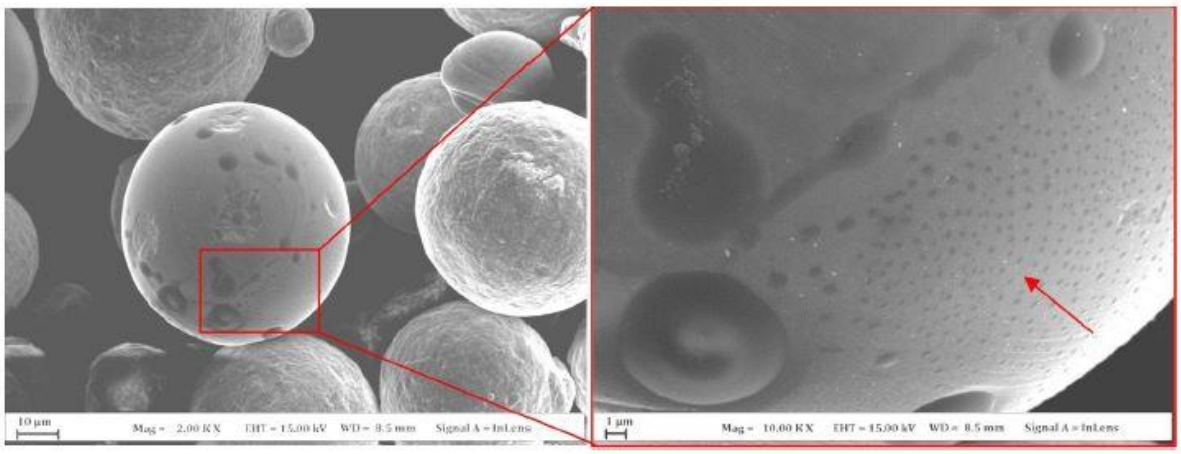

Figure 4.12: 316L powder after one conventional LS cycle [3].

Furthermore, since these oxides have been found mainly in the used powder particles rather than in the new powder, this may be due to exposure of powder in the chamber since the DED process chamber used to produce the samples does not exhibit a controlled atmosphere. So probably the powders exposed in the process chamber during fabrication may experience some oxygen uptake. Hence, it can be concluded that 316L powder is sensitive to oxidation during the DED process and tends to form Mn-Cr-Si surface oxides.

The microstructure of the powders was better observed by chemically etching the particles with the Kalling No.2 solution. Both new and used powders were cold mounted, polished and then etched with the solution for 10 seconds by immersion. As shown in Figure 4.13 and Figure 4.14, it appears that the microstructure is fine in both powders thanks to the high cooling rate and there are no inhomogeneities within the same particle, that is there are no areas that have a different microstructure within the same particle. It can be seen from Figure 4.14 a), some used powder particles are etched more aggressively than the particles that did not undergo the DED process. For this reason, it may be assumed that these particles will have different melting behaviours because they may have lost some alloying element or some precipitates may have formed that can more or less absorb the laser.

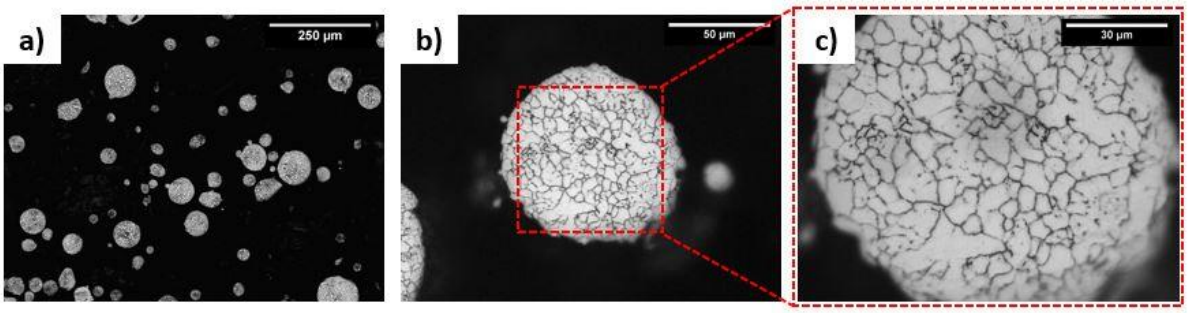

Figure 4.13: Optical Microscope micrographs: **a)** etched new powder, 100 X, **b)** enlarged micrograph of an etched particle, 500 X, **c)** detail microstructure inside the etched particle, 1000 X.

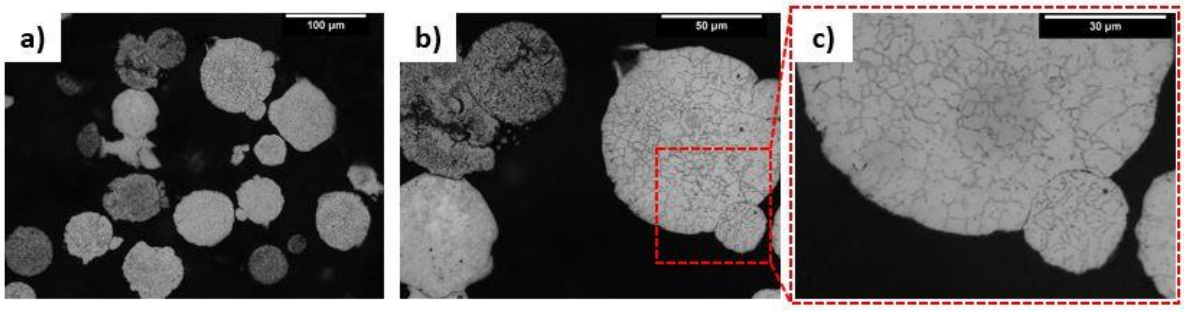

Figure 4.14: : Optical Microscope micrographs: **a)** etched used powder, 200 X, **b)** enlarged micrograph of an etched particle, 500 X, **c)** detail microstructure inside the etched particle, 1000 X.

4.1.4 Micro-Vickers hardness

In order to understand if mechanical properties are affected by the DED process, both powders were subjected to a Micro-Vickers hardness test using the micro-Vickers indenter Leica VMHT with a load of 100 gf applied for 15s. Micro-hardness measurements were taken on ten particles for both types of powder, as shown by the Figure 4.15 referring to some of the particles examined, and then the average Vickers micro-hardness has been calculated. The average Vickers micro-hardness of the new powder was 202 HV, which is about 15% harder than the Vickers micro-hardness (175 HV) of the used powder. This result further confirms that the microstructure changes after the DED process and this must be taken into account if the powder that has already undergone a DED cycle should be used for a new process.

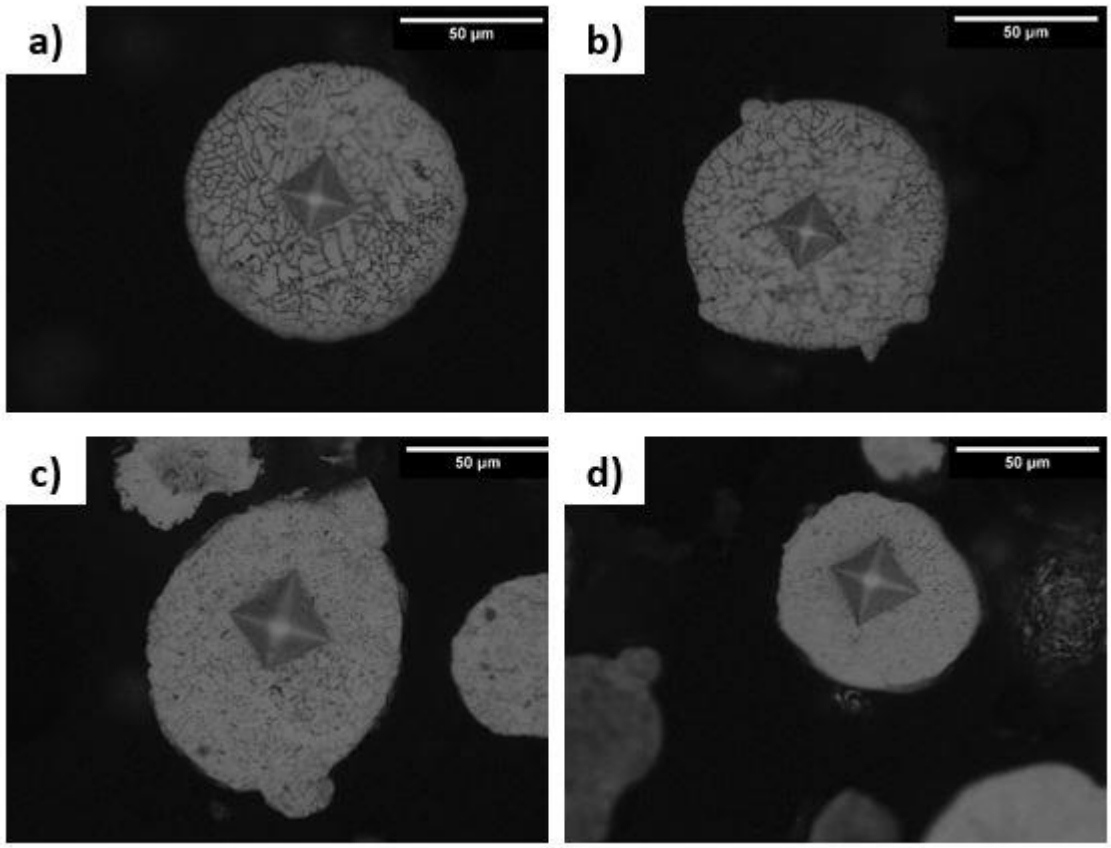

Figure 4.15: Optical Microscope micrographs of Micro-Vickers indentations on 316L new powder, **a)** and **b)**, at 500 X, and on 316L used powder, **c)** and **d)**, at 500 X.

4.2 Samples

In order to understand the effect of DED process parameters, like laser power and strategy, on the microstructure of the AISI 316L stainless steel, samples were cold mounted using ClaroCit resin, polished on SiC papers with granulations of 500, 800, 1200, 2400, 4000, and with 3 and 1 µm diamond pastes, chemically etched with the Kalling No.2 solution for 15 seconds by immersion, then observed at the optical microscope and SEM.

4.2.1 Microstructure

The solidification microstructure of the melt pools observed in the cross section of all stainless steel samples is dense, without the presence of any pores, cracks or unmelted powder particles and is characterized by the presence of regions with distinct microstructure. Due to temperature variation in the melt pool, the cooling rate varies along its volume and, for this reason, there are different microstructures in it [9]. Fine-grained structure (Figure 4.16 b)) is found near the top region of the scans where the melt pool cooling rate is relatively high, because radiation/convection heat loss is more prevalent.

The lowest solidification rates occur near final stages of melt pool solidification and are concentrated near the centre of the melt pool where large equiaxed structures (cellular structure) are observed (Figure 4.16 c)). If the top region of the melt pool can lose heat through radiation or convection and the perimeter undergoes a heat transfer with the baseplate, the centre of the melt pool sees a heat accumulation and hence a lower cooling rate.

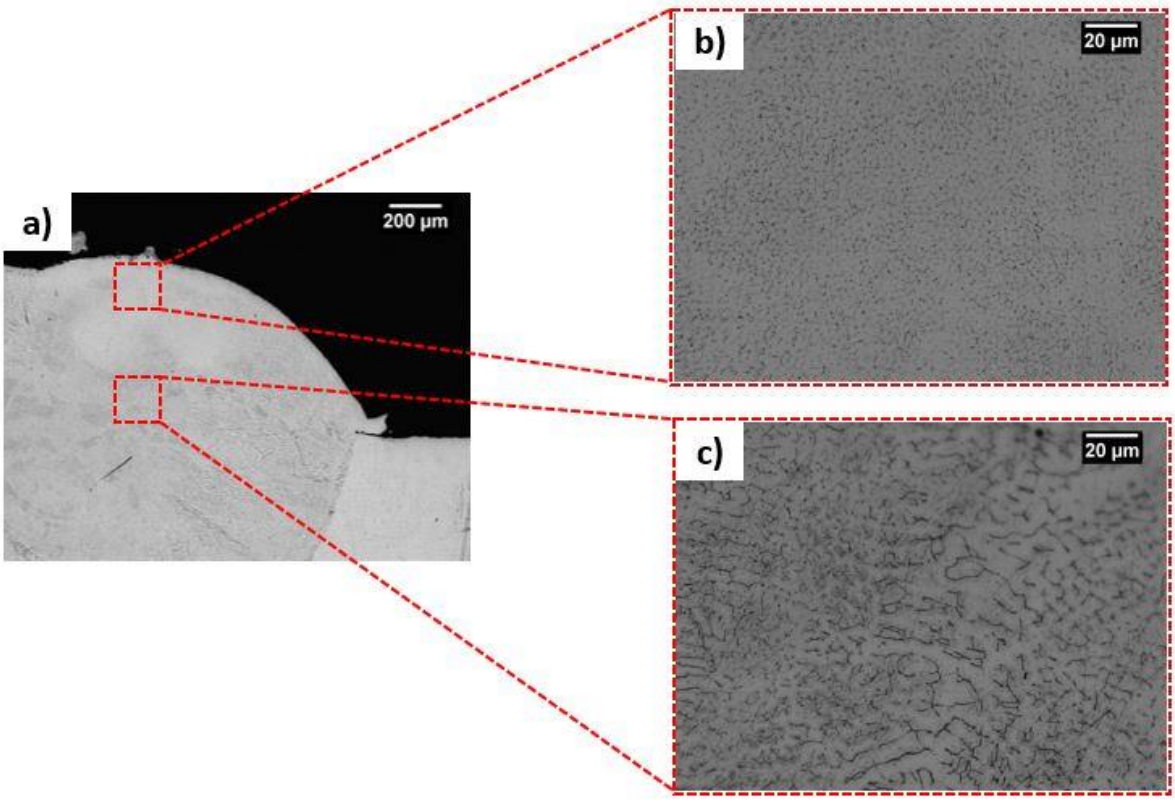

Figure 4.16: Optical Microscope micrographs: **a)** melt pool of the sample P3_3 50 X, **b)** detail of microstructure of the top of the melt pool, 500 X, **c)** detail of microstructure of the centre of the melt pool, 500 X.

As shown in Figure 4.17, relatively low solidification rates result in the columnar growth of dendrites throughout the entire length of the melt pool perimeter in all samples. It can be noticed that the growth direction of columnar dendrites is from the interface to the centre of the melt pool, that is the orientation of the dendrites tends to incline from the building direction (vertical) towards the centre of the melt pool. This can be explained considering that local heat transfer conditions, in particular the solidification heat flux direction, dictates grain orientation and texture evolution. As the height of the melt pool increases, its bulk temperature becomes higher, and consequently, heat transfer via part-to-baseplate conduction may become lower than that due to part convection/radiation. As a result, directional growth of dendrites more perpendicular to the build direction will occur. In addition, Figure 4.18 shows the flow lines observed along the melt pool boundaries caused by the heat flux during solidification.

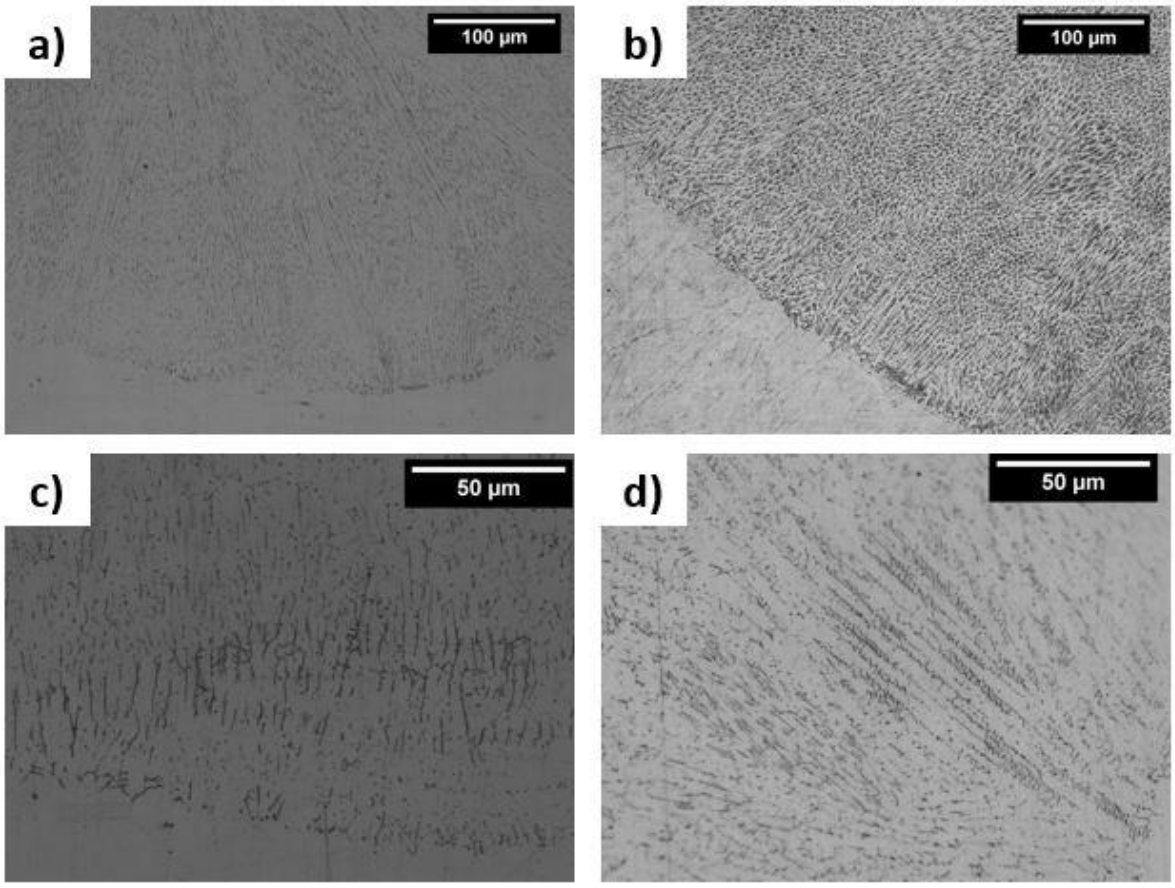

Figure 4.17: Optical Microscope micrographs of columnar growth of dendrites: **a)** sample P3_3 200 X, **b)** sample P3_7 200 X, **c)** sample P3_3 500 X, **d)** sample P3_6 500 X.

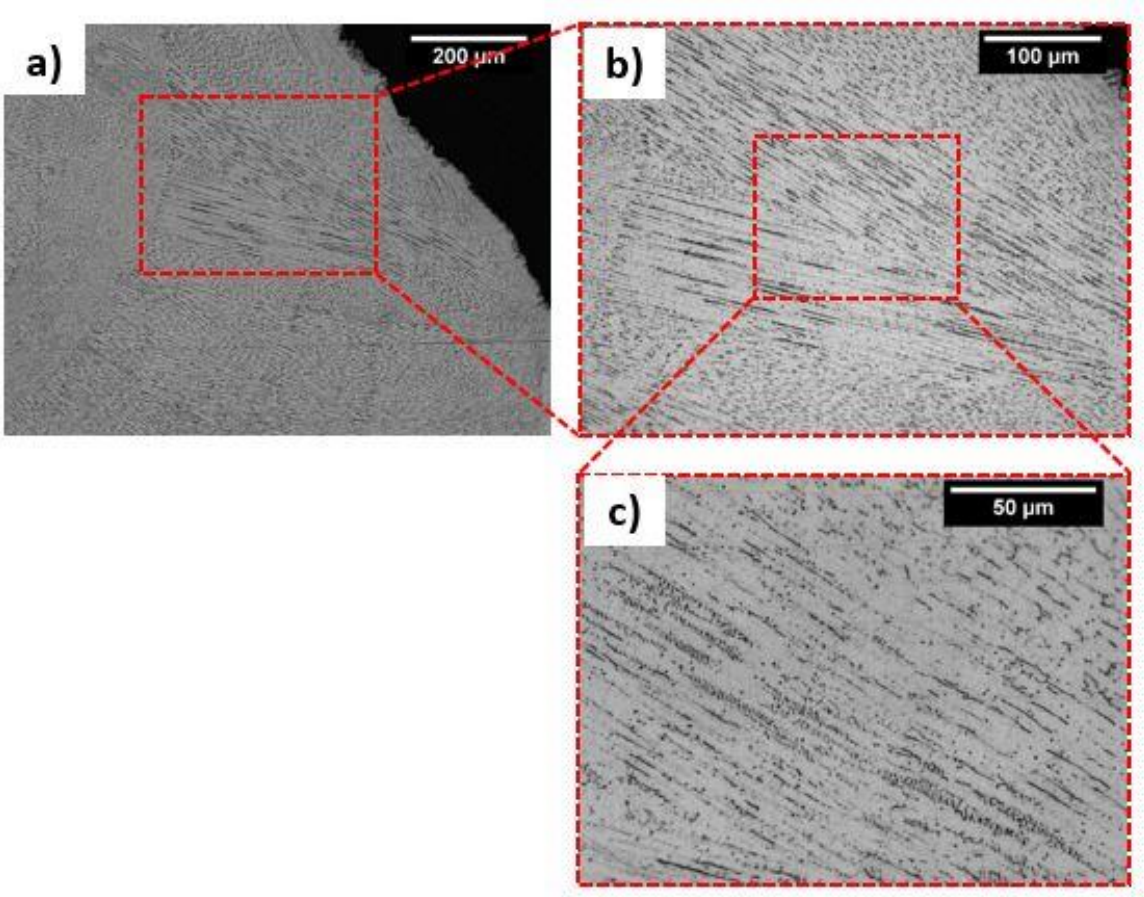

Figure 4.18: Optical Microscope micrographs: **a)** flow lines at the beginning of the melt pool boundary of the sample P3_8 100 X, **b)** detail of flow lines 200 X, **c)** detail of flow lines 500 X.

It has also been observed that the microstructure near the bottom of the melt pool remain equiaxed austenite grains, as shown in Figure 4.19 and as confirmed by the work of Rong et al. [4] who found the same microstructure near the fusion line of the weld shown in Figure 2.18.

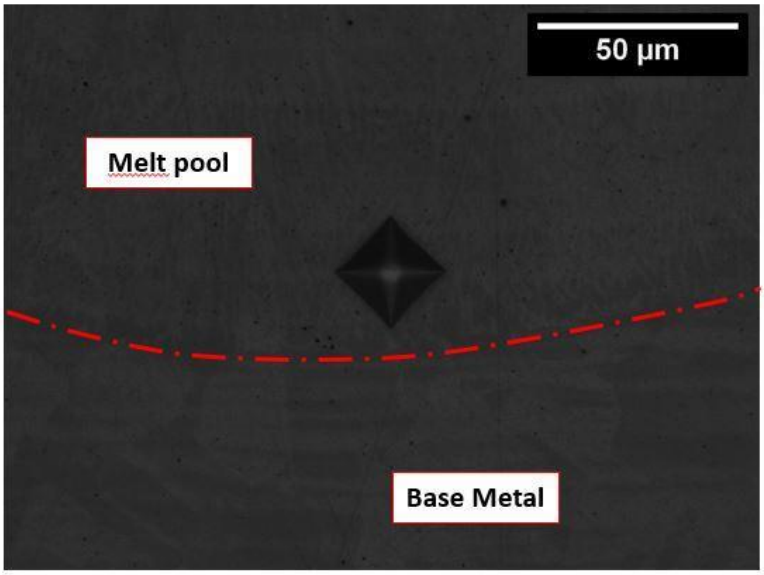

Figure 4.19: Optical micrograph of a Micro-Vickers indentation near the melt pool boundary (red dashes) at a magnification of 500 X. Below the boundary, the equiaxed austenite grains are visible.

As it has already been seen during the analysis of the powder, during the DED process metallographic structures of austenite and delta ferrite solidify (Figure 4.20).

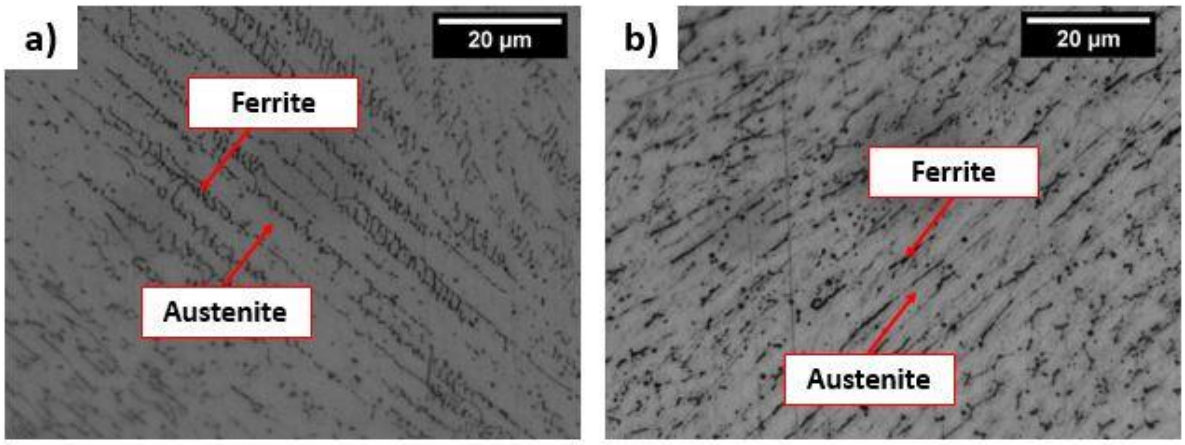

Figure 4.20: Melt pool microstructure near the boundary: **a)** sample P3_3, 1000 X, **b)** sample P3_7, 1000 X.

The presence of austenite and ferrite was confirmed by the experiments performed by Takalo et al. [2] that the austenitic solidification in austenitic stainless steel welds was related to the composition of the alloy. In fact, considering the chemical composition of the AISI 316L stainless steel powder (Table 2) and finding the location of the composition of the steel on the Schaeffler constitution diagram (Figure 2.14), they observed that the composition was located inside the ferrite-austenite area predicting a ferritic phase between 0 wt% and 5 wt%. Furthermore this result was also confirmed by Rong et al. [4] and Huang et al. [5] who worked on T-joint laser welding 316L, observing a microstructure very similar to that analyzed in this work, identifying the austenite and ferrites structures in the weld centre and around the fusion line (Figure 2.15 and 2.16).

In addition to the ferrite formation, a sort of segregation has been observed near the central region of the melt pool (Figure 4.21). As it has been analyzed in the work of Rong et al. [4], probably this segregation is induced by the non-spontaneous nucleation that refines grains. This conclusion was taken because they found the same microstructure that was observed within the melt pool of the samples analyzed during this work, but this segregation certainly needs to be better investigated.

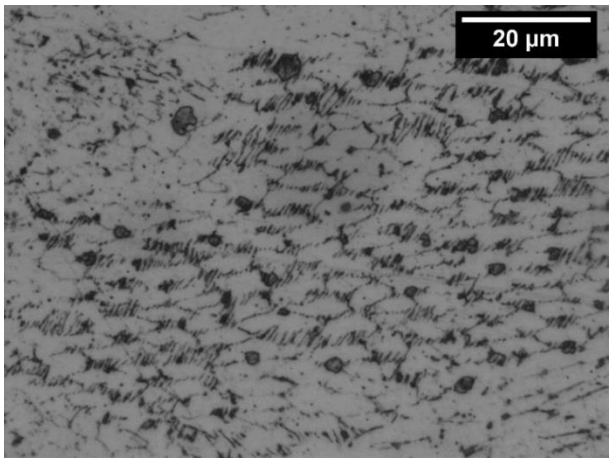

Figure 4.21: Optical micrograph of segregation within the melt pool at a magnification of 1000 X.

Even in the samples built by DED it have also been detected sub-micrometer features dispersed throughout the melt pool and present in all samples. An EDS analysis was carried out on these features and the result confirmed that these features of O, Si and Mn are present also in the samples, the same features with the same chemical composition of those found in the powders analyzed above. Furthermore this result was confirmed by Wang et al. [25] who found the same features rich in O, Si and Mn in L-PBF 316L, but they were much smaller (nanometric size) and observed along the cellular walls, within the ferritic phase (Figure 2.17).

Furthermore, analyzing the microstructure of the samples, particularly the surface, Chromium oxides have been identified, whose composition was confirmed by the result of an EDS analysis shown in Figure 4.22. It can be noticed that in the top region of the sample there is a layer rich in Cr and O, but poor in Fe and Ni. This is due to the fact that stainless steels like 316L contain sufficient chromium to undergo passivation in contact with the oxygen, forming a film of chromium oxide on the surface. This layer prevents further corrosion by stopping oxygen diffusion to the steel surface and blocks corrosion from spreading into the bulk of the metal.

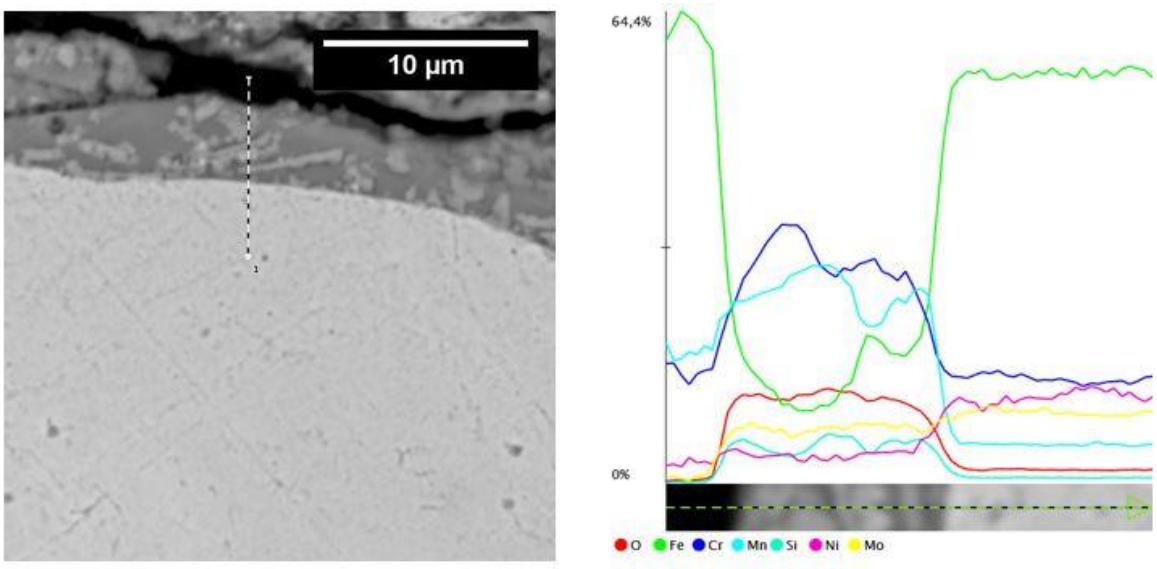

Figure 4.22: Linescan analysis and concentration of O, Fe, Cr, Mn, Si, Ni and Mo.

The effect of process parameters, such as laser power, and strategy on the samples microstructure was investigated in the discs. In particular, the size of the dendritic arm spacing (DAS) has been investigated and what was the effect of power and the strategy on it. Four samples (P3_1, P3_2, P3_3 and P3_4) have been analysed and for each sample three OM micrographs of the columnar dendritic area between the boundary and the centre of the melt pool were taken at a magnification of 1000 X (Figure 4.23).

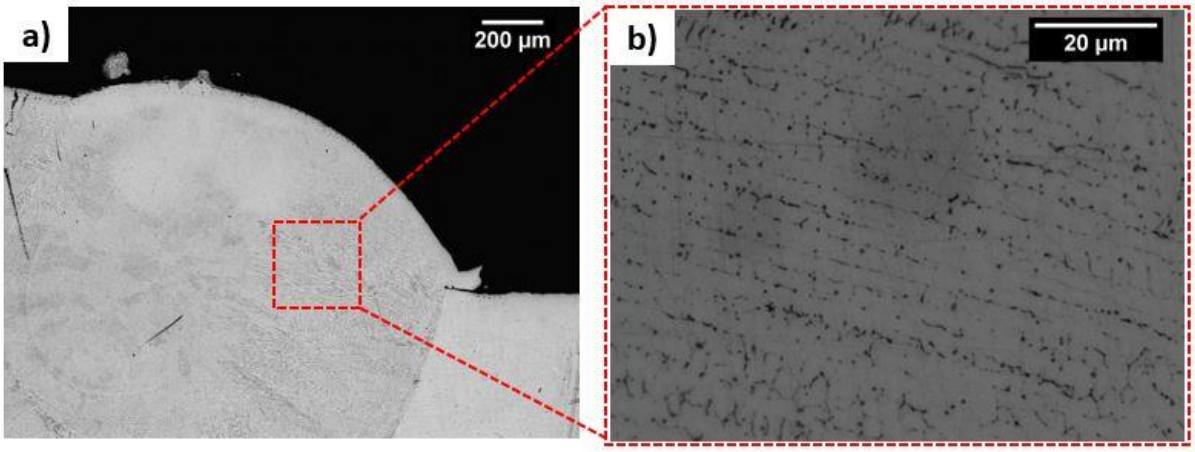

Figure 4.23: a) Columnar dendritic area between the boundary and the centre of the melt pool, 50 X and **b)** detail of the columnar dendritic area, 1000 X.

Then the DAS was calculated for each sample using the software Image J on the OM micrographs and the results are listed in Table 7. As shown in Figure 4.24, with the increase of laser power, the dendritic structures of the melt pool boundary change from thin (with an average value of 2 µm for samples built with a laser power of 300 W) to coarse (with an average value of 3 µm for samples built with a laser power of 600 W) gradually, which means that dendrite arm spacing (DAS) increases. This is due to the fact that the high heat energy provided by high power laser can make the melt pool deep and wide and can reduce the solidification velocity, giving the dendrites more time to grow coarse. In fact, the DAS of columnar structure is mainly affected by the cooling rate and the heat input [8]. For this reason, the higher cooling rate and the lower heat input tend to refine the dendrite arm spacing. If power has an important effect on the microstructure, choosing a strategy rather than another seems not to affect the size of the DAS.

Table 7: Dendritic arm spacing (DAS) measurement for samples P3_1, P3_2, P3_3 and P3_4.

	P3_1 : 300 W, S1	**P3_2 : 300 W, S2**	**P3_3 : 600 W, S1**	**P3_4 : 600 W, S2**
DAS (µm)	1,9 ± 0,3	2,1 ± 0,2	2.9 ± 0,4	3.0 ± 0,3

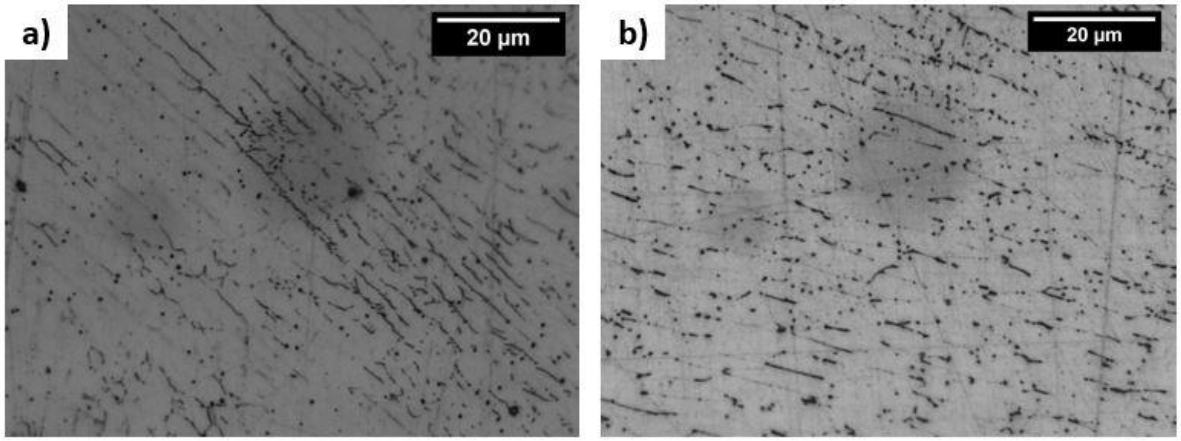

Figure 4.24: Optical micrographs of dendritic structures in **a)** sample P3_5 and **b)** sample P3_7, at 1000 X.

4.2.2 Effect of process parameters and strategy on the melt pool geometry and size

The chemical etching with Kalling No.2 solution has also allowed to calculate the size of melt pools. Comparing the micrographs of the melt pools of all the samples (Figure 4.25, 4.26, 4.27 and 4.28) obtained by observing them at the optical microscope, it can already be noted laser power, scanning strategy and overlap have a strong effect on the morphology of the layers.

As far as circles are concerned, it can be noticed that, as expected, the higher is the power the larger are the scans and that the scanning strategy (S1 and S2) doesn't have a strong influence on the melt pool size (Figure 4.25).

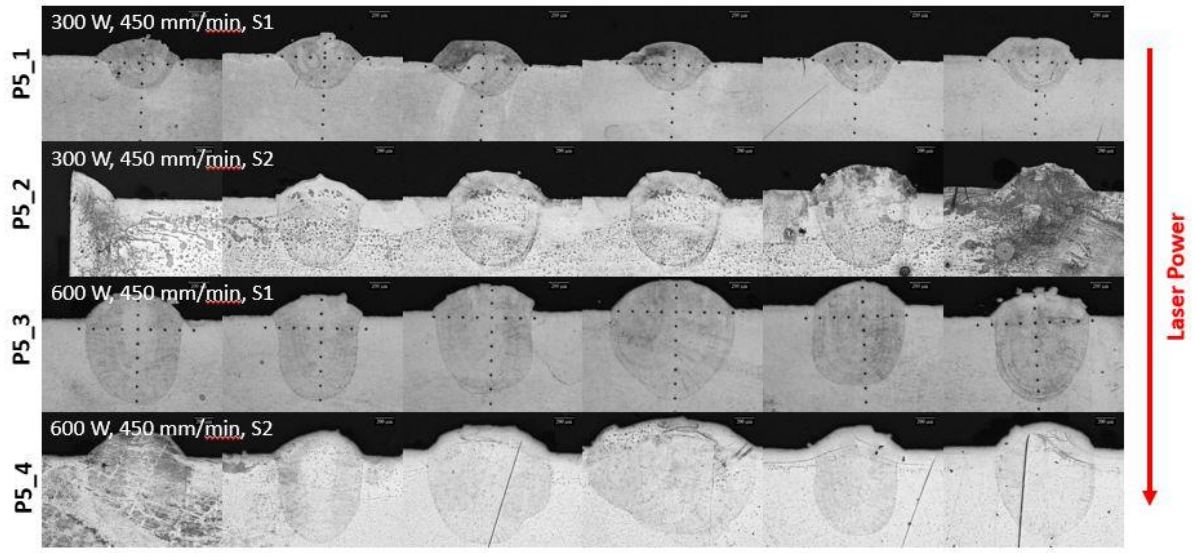

Figure 4.25: Optical micrographs at 50 X of cross sections of samples P5_1, P5_2, P5_3, P5_4 belonging to Baseplate 5.

Spirals morphology is strongly influenced by the laser power, however in this case, the choice of one strategy rather than the other can give a different shape to the whole scan (Figure 4.26, 4.27 and 4.28). In addition, increasing laser power also increases scan height, especially if the sample has a high overlap value (e.g. 50-70%).

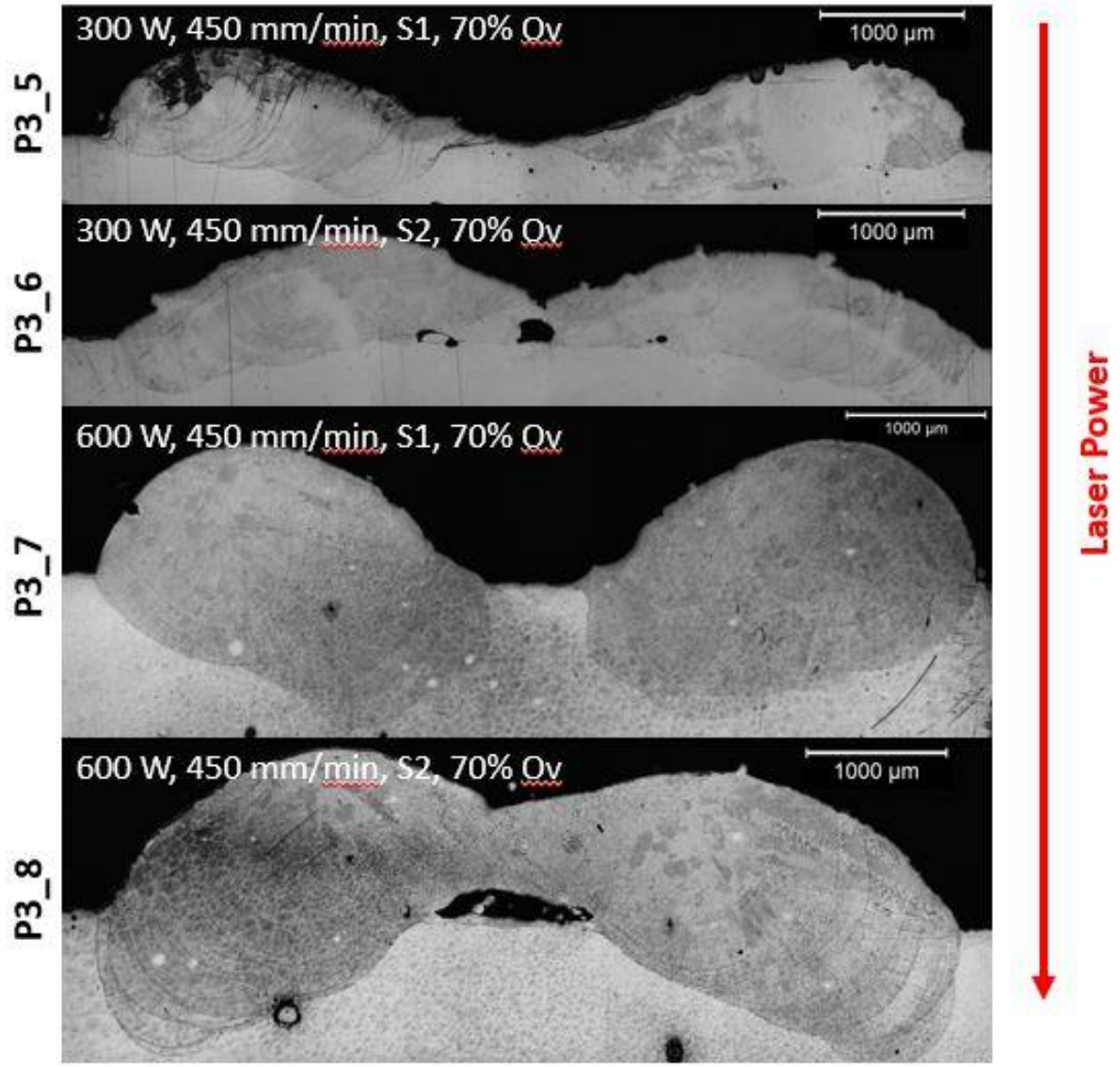

Figure 4.26: Optical micrographs at 50 X of cross sections of samples P3_5, P3_6, P3_7, and P3_8 belonging to Baseplate 3 (70 % overlap).

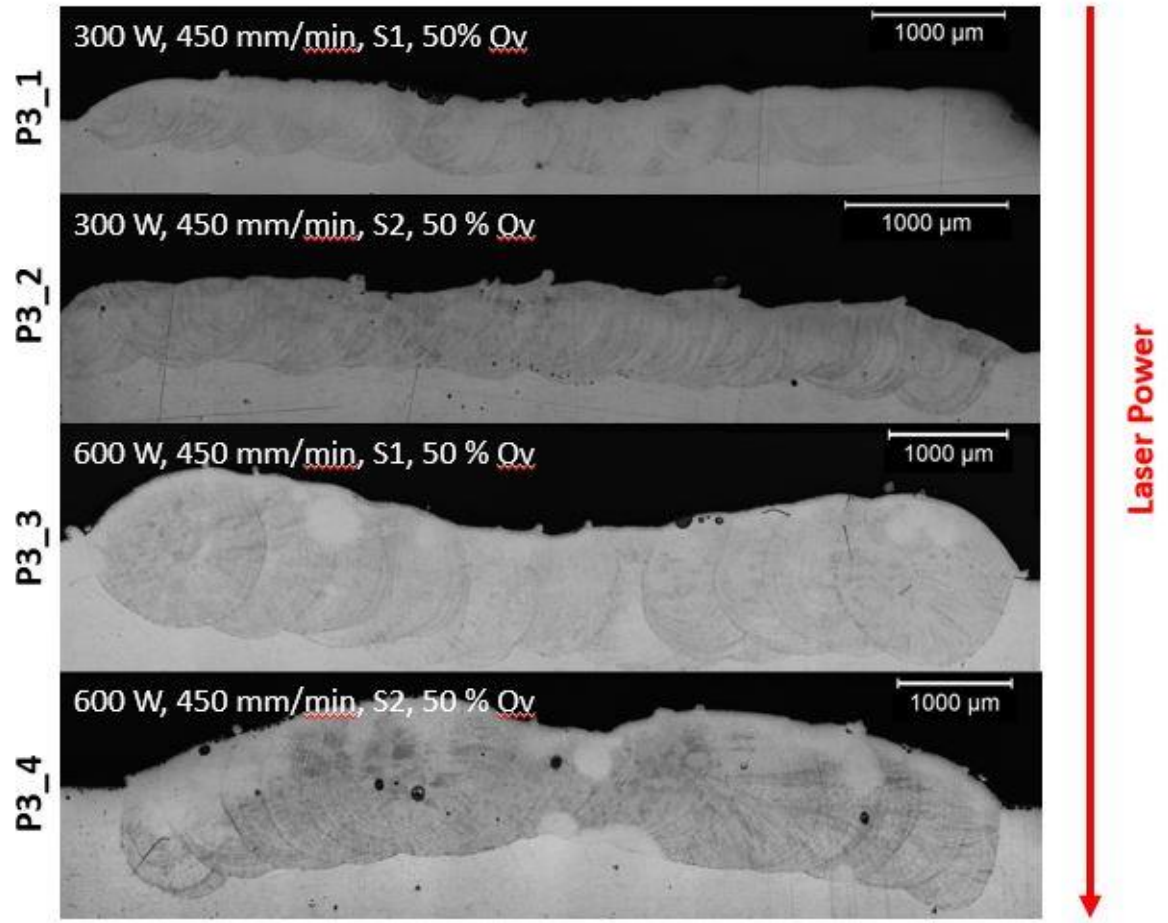

Figure 4.27: Optical micrographs at 50 X of cross sections of samples P3_1, P3_2, P3_3, and P3_4 belonging to Baseplate 3 (50 % overlap).

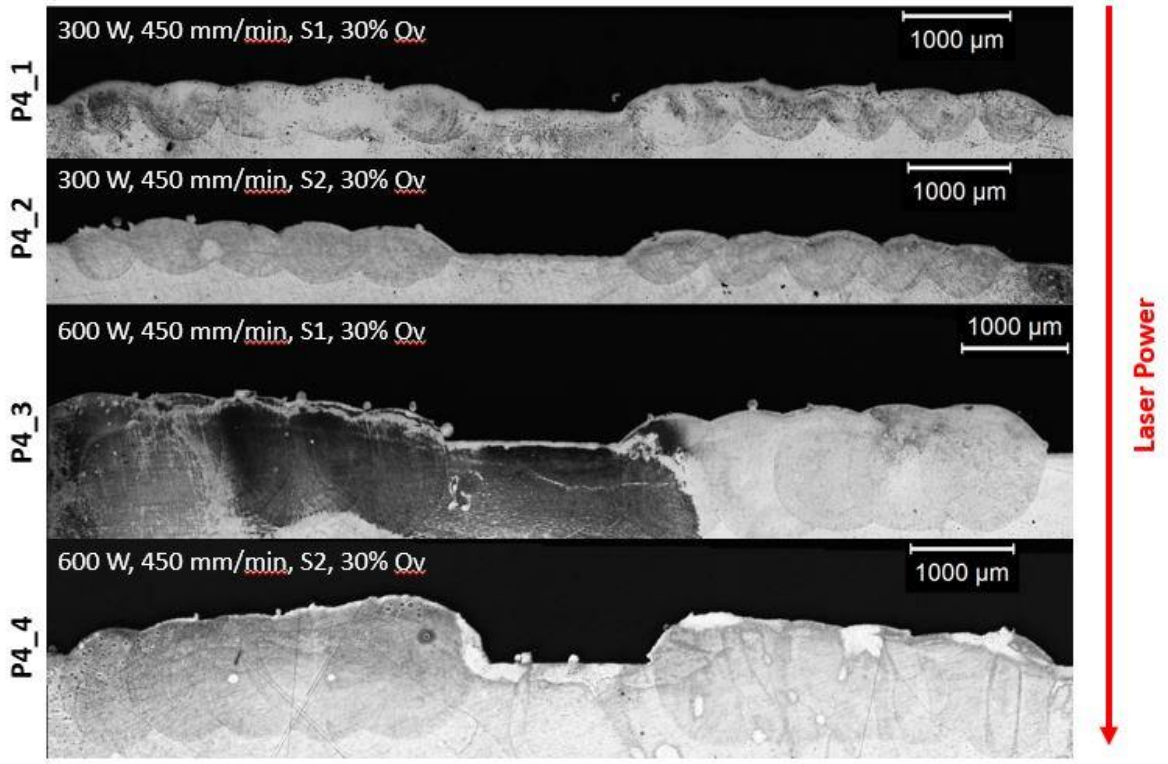

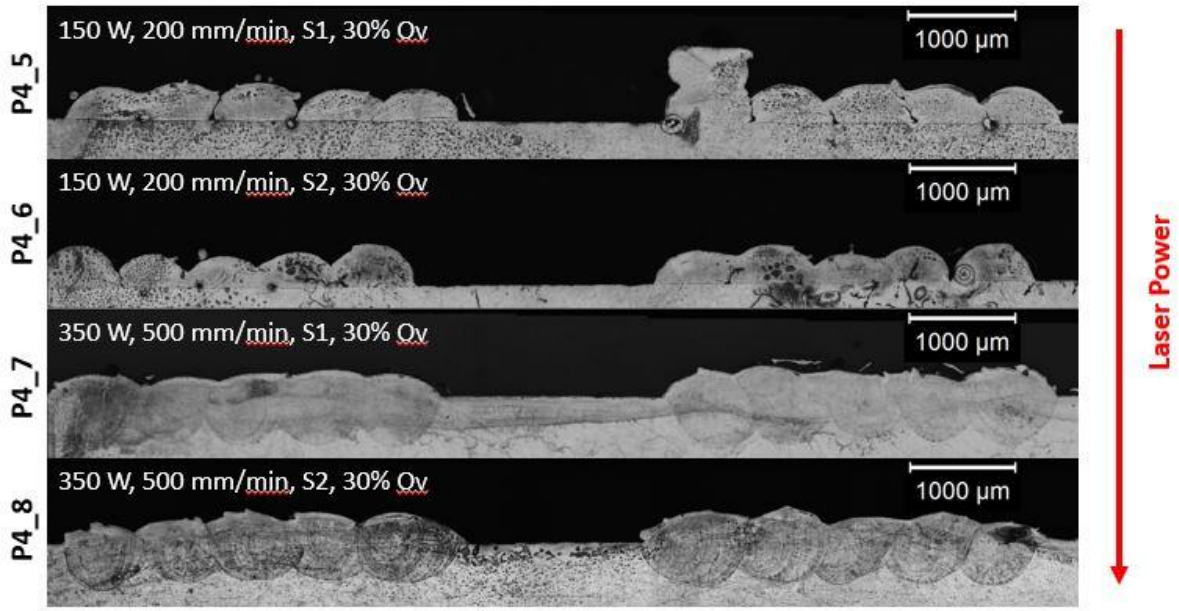

Figure 4.28: Optical micrographs at 50 X of cross sections of samples P4_1, P4_2, P4_3, P4_4; P4_5, P4_6, P4_7, P4_8 belonging to Baseplate 4.

These considerations have been confirmed by the results obtained by measuring the size of the melt pool using the Image J software. The following sections will treat separately the analysis conducted on the circles (Baseplate 5) and that conducted on the spirals (Baseplates 3 and 4).

Circles – Baseplate 5

The Figure 4.29 shows the geometric features of a scan that were measured for each sample using the Image J software in order to have a clear insight on the effect of the building parameters and the strategy on the morphology of the scan. In particular, W and H are the width and the height of the melt pool respectively, G is the growth and D is the depth. In addition, the G/H and G/D ratios and the Linear Energy Density (LED) parameter, e.g. $LED = P/(v \cdot 60)$, where P is the laser power and v is the laser scanning speed, were calculated. LED is a very important and useful parameter for quantifying a laser process and for seeing how the effects in terms of microstructure and properties of a part are related to process parameters.

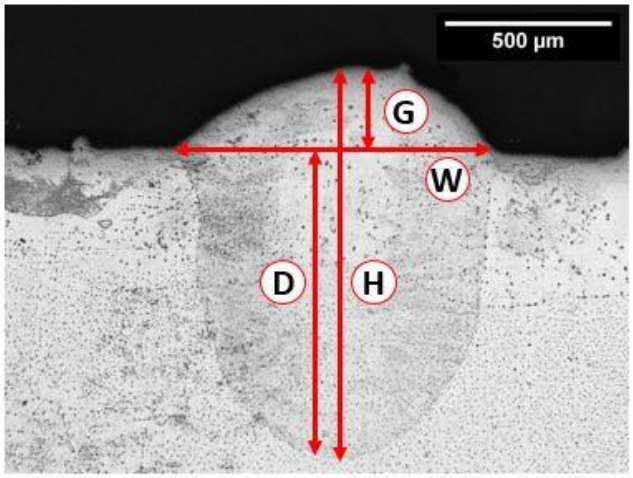

Figure 4.29: Geometric features that were measured for each sample using the Image J software.

As far as circles are concerned, the four samples P5_1, P5_2, P5_3 and P5_4 (whose process parameters are listed in Table 5) have been chosen, which have the same laser scanning speed (450 mm/min) but different laser powers (300 W and 600 W) and opposite strategies. The results are shown in the Figure 4.30 a), b), c) and d) below.

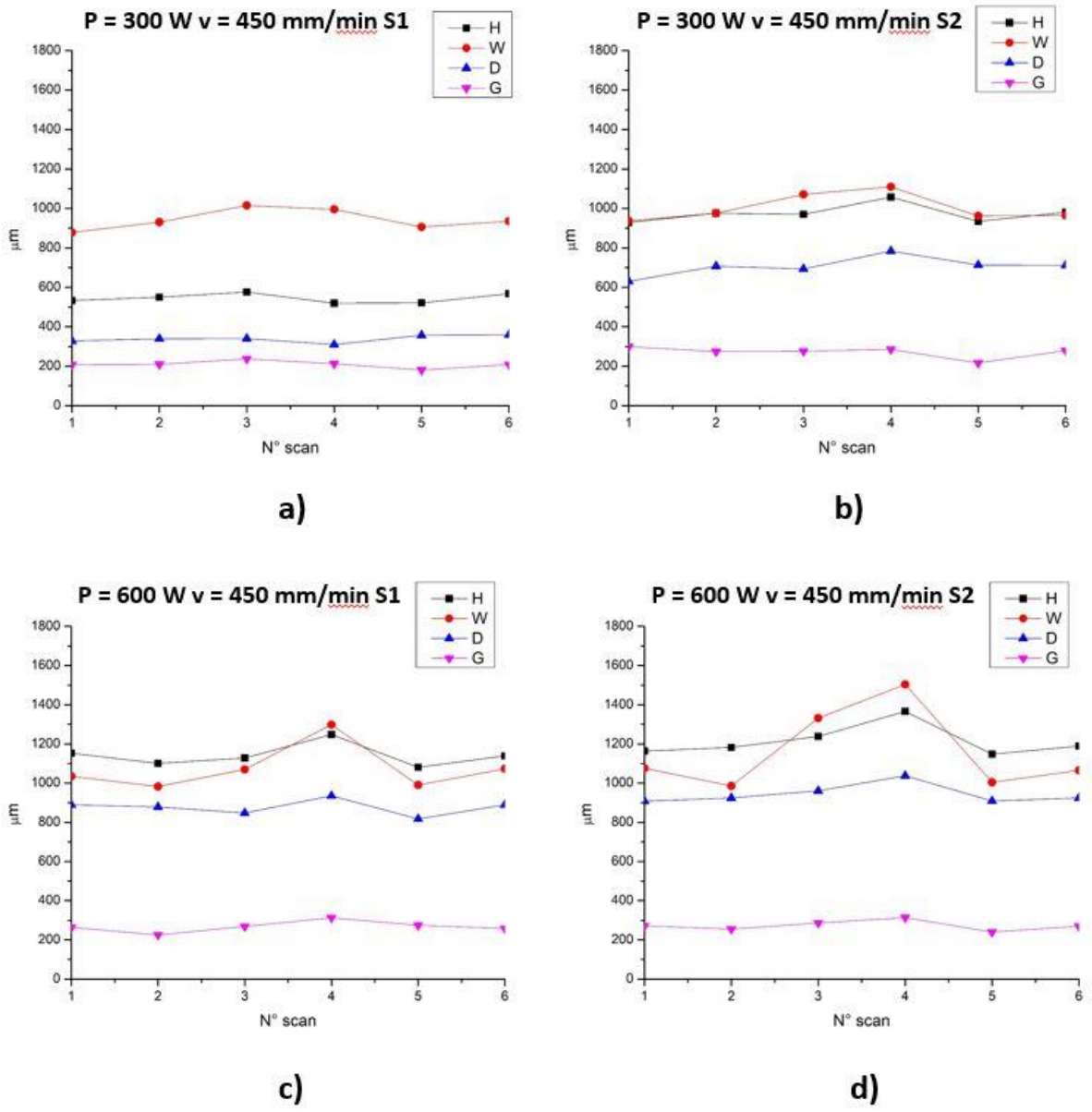

Figure 4.30: Measurement of the height (H), width (W), growth (G) and depth (D) of the melt pool of the samples **a)** P5_1, **b)** P5_2, **c)** P5_3 and **d)** P5_4.

Comparing the first two samples P5_1 and P5_2 with 300 W of laser power, regardless from the scanning strategy (S1 or S2), the melt pool width is always the same (about 900 µm) with the central scans that are larger than the external ones. This indicates that, because of the reduced radius of the internal circle, there is a heat accumulation effect that affects the morphology of the scan. The change of strategy instead affects the height of the melt pool that undergoes a sharp increase, from 500 µm with the S1 strategy to 900 µm with the S2 strategy. As the S2 strategy starts from the external circle and moves to the internal one, the heat

accumulated is higher and this leads to a higher height of the melt pool. Growth has the same value in both cases, so the strategy has no effect on it, while the strategy has an influence on depth that doubles (from 300 µm to 600 µm). Considering the two samples with 600 W of laser power, the height, width, growth and depth are the same for both samples. In fact, the height is about 1200 µm, the width is about 1100 µm reaching a peak in the central scan of 1500 µm; the depth and the growth are about 900 µm and 300 µm respectively. So when the process requires high powers such as 600 W, the effect of strategy change is exceeded by the particularly high process parameter and therefore there is no change in the melt pool geometry. Considering the same strategy and comparing the samples with different power (300 W and 600 W), it can be noticed that the height is drastically increased from 900 µm to almost 1200 µm, and the width increases slightly (from 900 µm to 1000 -1100 µm), the depth reaches 900 µm while growth is the only magnitude that remains constant in all samples. For this reason, it can be said that both the increase in laser power and the change of strategy mainly affect the height and the depth. If the main goal is to get an increase in width, it is needed just to increase the laser power without acting on the strategy. Moreover, since the growth is constant, if getting an effect on this geometric feature is required, it is not necessary to increase laser power or change strategy, because they have no effect on the growth of the melt pool.

As the growth has a fairly constant value while the height and the depth change with power gain and strategy change, charting G/H and G/D ratios for all four samples it can be noticed that doubling the power both ratios are lowered, almost halved, just because both the height and the depth increase (Figure 4.31).

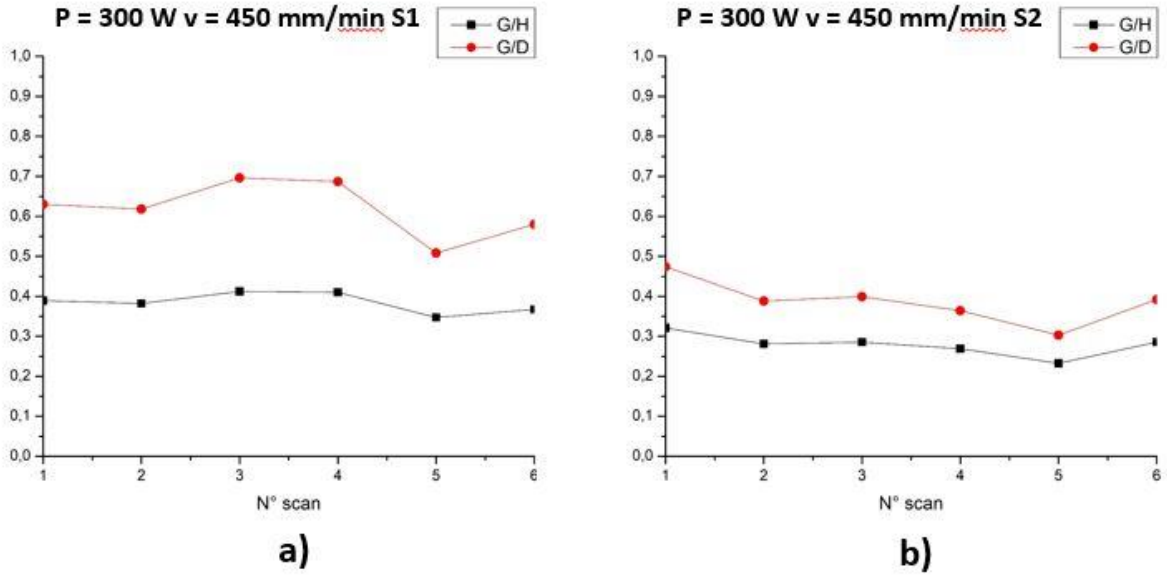

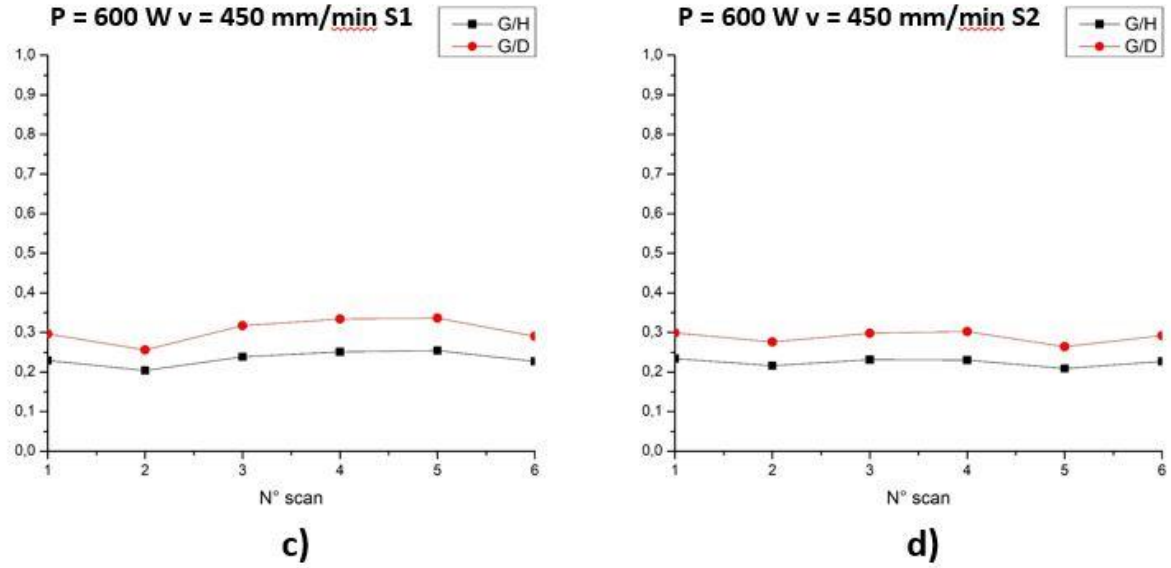

Figure 4.31: G/H and G/D ratios for the samples **a)** P5_1, **b)** P5_2, **c)** P5_3 and **d)** P5_4.

Using these geometric data, it was possible to calculate the powder efficiency P_e, e.g. $P_e = (A_c \cdot F \cdot \rho_p)/f$, for each sample, where A_c (mm^2) is the measured scan area, f (g/s) is the feeding rate, F (mm/min) is the scanning speed and ρ_p (g/cm^3) is the powder density. The powder efficiency was calculated for each scan of samples P5_1 (S1), P5_2 (S2), P5_3 (S1) and P5_4 (S2) that have a feeding rate of 0.0415 g/s, a scanning speed of 450 mm/min (building parameters in Table 5). The powder density is considered to be the theoretical 316L density: 7.99 g/cm^3. As shown in Figure 4.32, the area A_c has been approximated by considering the area of a triangle which base is the width of the melt pool W and as its high the growth of the melt pool G.

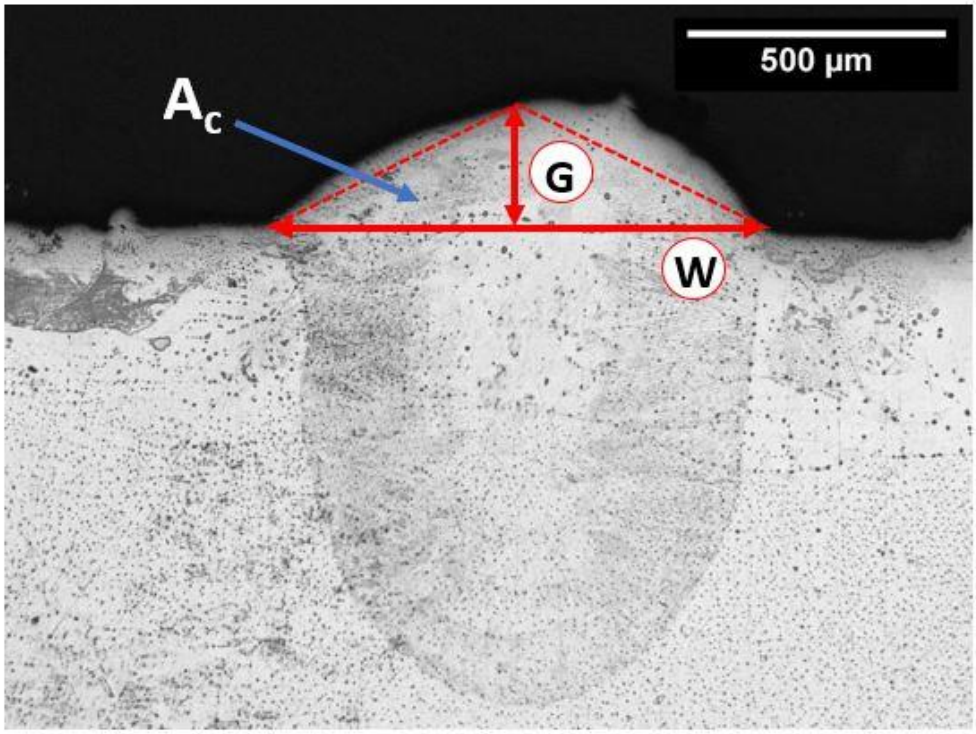

Figure 4.32: Measurement of area Ac.

The powder efficiency results of the four samples are reported in Figure 4.33.

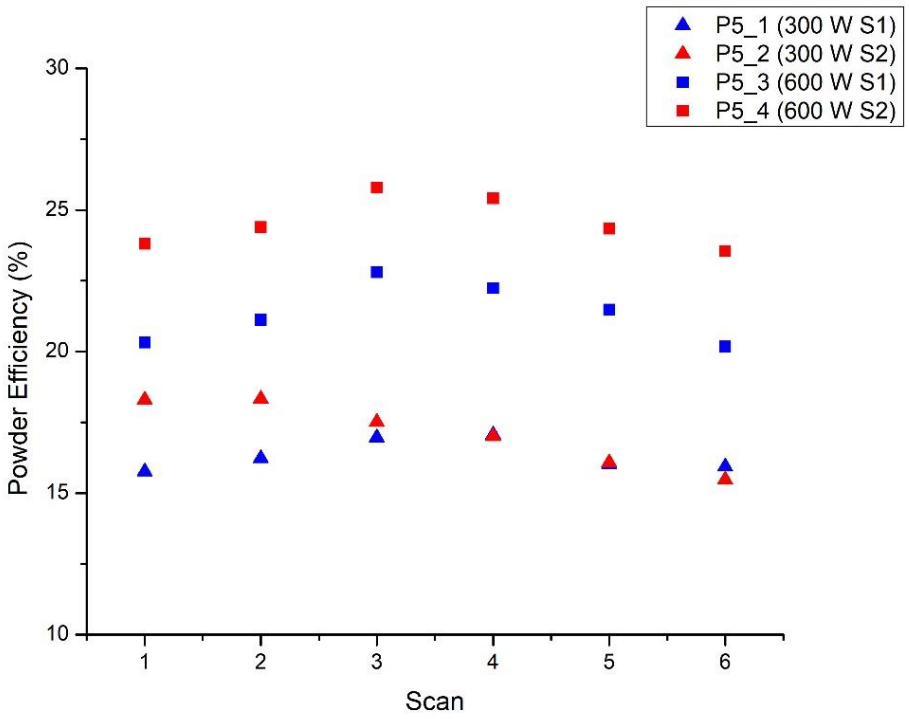

Figure 4.33: Powder efficiency of the samples P5_1, P5_2, P5_3 and P5_4.

From the measurements made on the four samples, it was noted that for samples P5_1 and P5_2 built with relatively low power (300 W), average powder efficiency values of about 17 % are obtained, while working with higher laser powers, such as 600 W, powder efficiency reaches values of 23 %. This result suggests that, as the overlap volume between the powder stream and laser irradiation area is constant, when low power values are used a larger fraction of particles crosses the laser beam and do not melt.

Moreover, the strategy seems to have an effect on the powder efficiency value. In fact, comparing the samples P5_1 and P5_2, they have a P_e value of 14 % and 19 %, respectively, while the samples P5_3 and P5_4 have a P_e value of 21 % and 24 %, respectively. For this reason, the S2 strategy (from the external to the internal) seems to be preferable if higher P_e values must be achieved. It is important, however, to underline that the DED process has in general low powder efficiency values, so this could lead to large amounts of recycled and 'scrapped' metallic powders. For this reason, it is very important to understand if the metallic powder that has already undergone a DED process can be reused, thus ensuring a raw material recycling and therefore a reduction in waste.

Spirals – Baseplates 3 and 4

As far as the spirals are concerned, the geometric features that were measured for each sample are shown in Figure 4.34. In particular, Wtot is the total width of five melt pools and W is the width of a single melt pool, H is the height of the melt pool, G is the growth and D is the depth. The Linear Energy Density (LED) parameter was calculated, as well as the overlap percentage (Ov) in order to study the overlap effect.

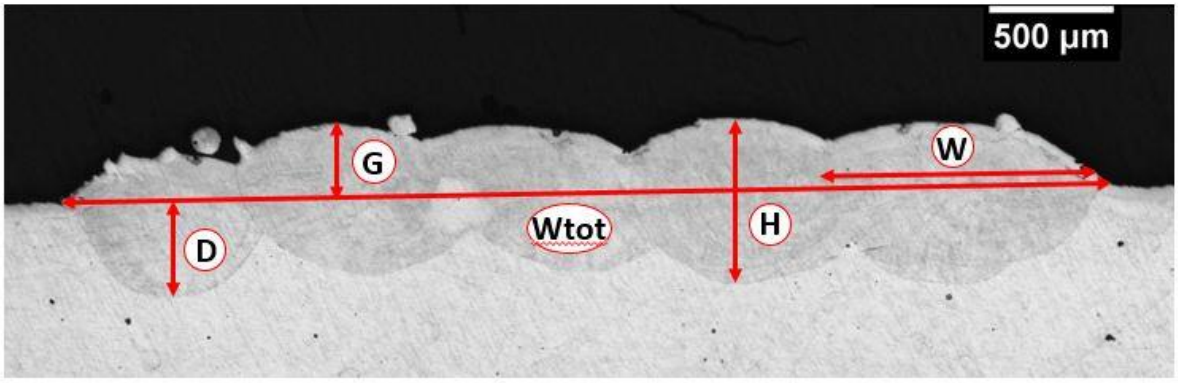

Figure 4.34: Geometric features measured for each sample using the Image J software.

The overlap percentage is related to the scanning space and directly influences the smoothness of the forming surface. An improper selection of the overlap degree could lead in fact to slope of the forming surface [30]. Referring to Table 4 in which the building parameters for spirals are listed, it is important to underline that the overlap has been established by SUPSI on a 1 mm large scan regardless from the building parameters. Therefore, all samples with an overlap of 50 % have 0.5 mm separated scans, while samples with an overlap of 70 % have a 0.3 mm separated scans.

The effect of the scanning strategy is clearly visible in Figure 4.35 where the micrographs of samples P3_3 and P3_4 are compared. In the sample built with the S1 scanning strategy (P3_3), the internal circle is covered by the external ones, while the contrary happens in the sample P3_4, built with the S2 scanning strategy. As shown in Figure 4.35, it can be noticed that it is not possible to define a clear border of the overlapping zone because, due to the remelting, the border of the first melt pool is not visible. For this reason, in S2 spirals the width W is calculated on the internal scan because, as discussed previously, the external melt pool is not completely visible, while in S1 spirals W is calculated on the external scan. This method of measurement chosen is clearly shown in Figure 4.36.

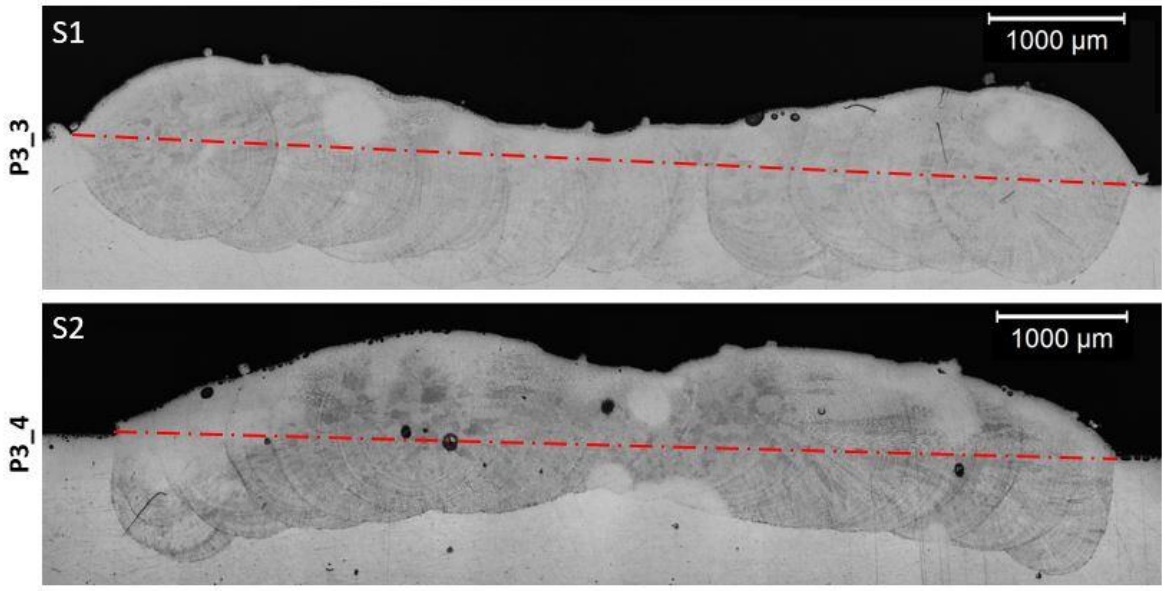

Figure 4.35: Optical micrographs at 50 X of cross sections of samples P3_3 and P3_4; the red dashes indicate the baseplate line.

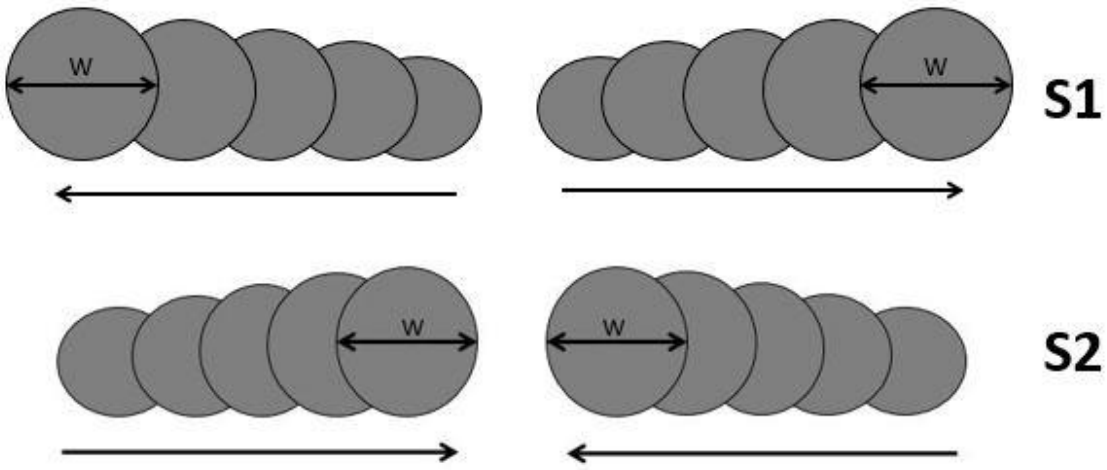

Figure 4.36: Schematic representation of width W measurement for both strategy, S1 and S2.

The overlap percentage (Ov) was therefore calculated based on the schematic representation reported in Figure 4.37, as:

$$Ov = -\frac{Wtot-5W}{4} \tag{4.2}$$

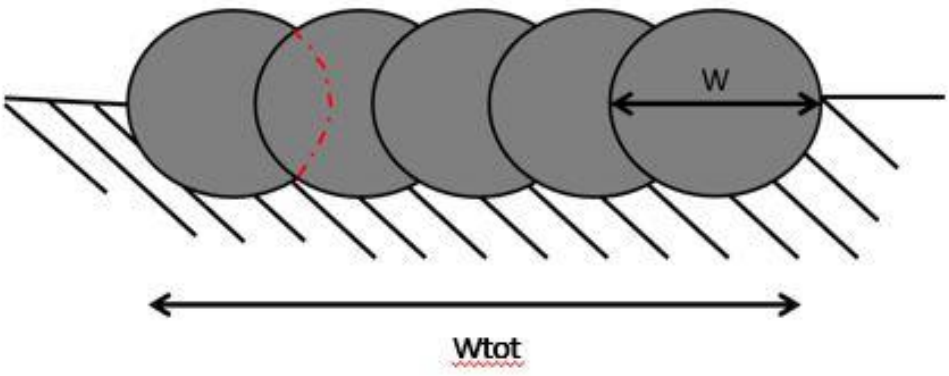

Figure 4.37: Schematic representation of one side of a spiral cross section (the red dashes represents the melt pool boundary, which is not visible by Optical Microscope)

The most interesting trends are plotted as a function of LED in Figure 4.38. It can be noticed that larger overlap values were observed in samples built with high LED. When low overlap values are chosen as building parameters (Figure 4.38 a), the comparison of the overlap values obtained with S1 and S2 scanning strategies shows that S2 strategies gives larger overlap when high LED are used. However, this difference might be related to the measurement issue, as explained in the previous paragraph. In S2 spirals the width (W) value is calculated on the internal scans and, as discussed in the comments to Figure 4.36, the internal scan are larger than the external ones because of the heat accumulation effect. It can be noticed also that when high laser powers are used (600 W), the overlap calculated is larger than the

nominal one. This is due to the fact that high laser powers lead to larger and deeper melt pools, so to bigger overlap values. For this reason, lower laser power values ensure the overlap percentage established at the project stage.

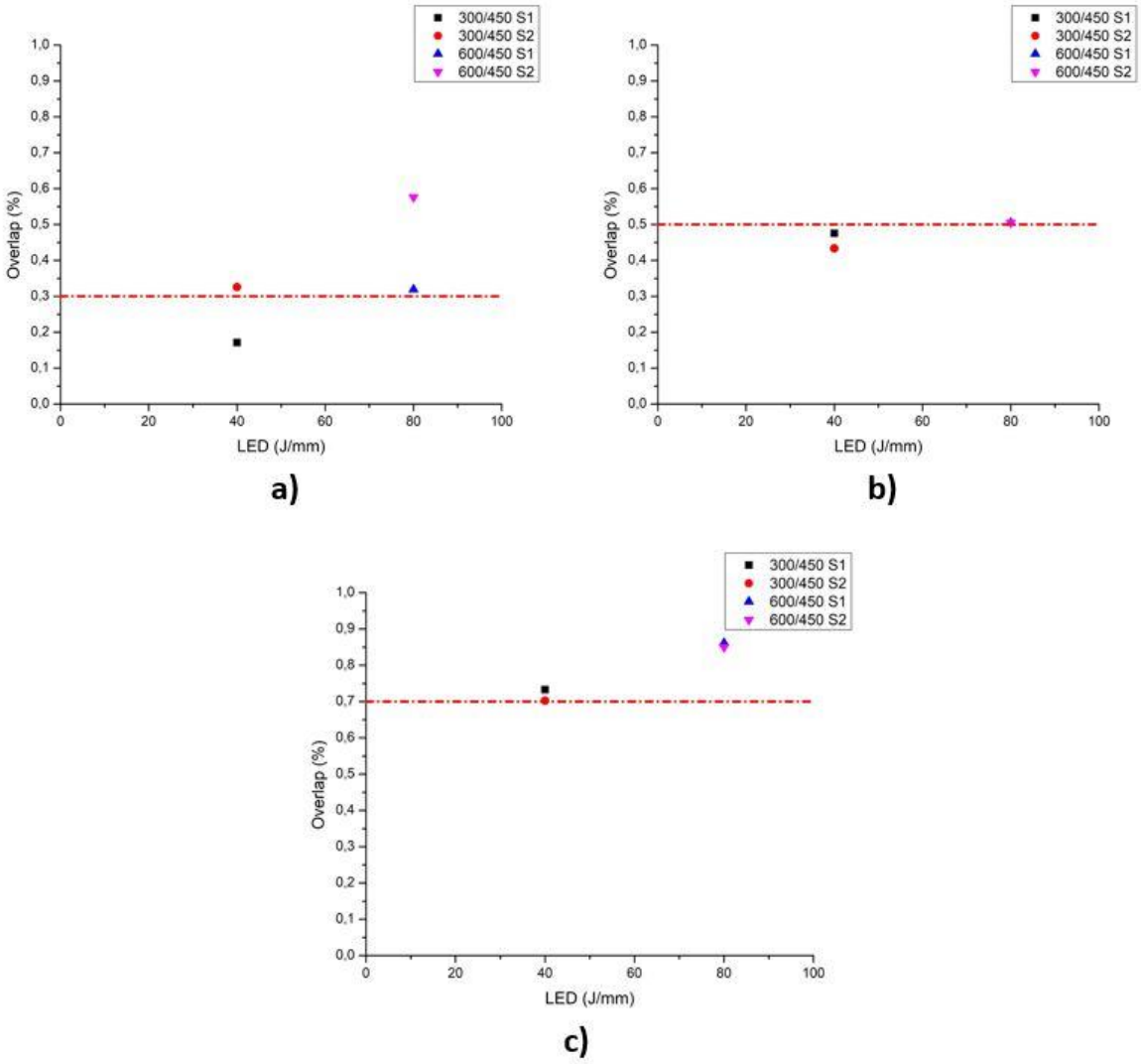

Figure 4.38: Overlap percentage of spirals built with different LED, **a)** 30 %, **b)** 50 %, **c)** 70 %.

In order to better understand the overlap effect, the total width (Wtot) of the five melt pool and the mean height (H mean) of the five scans have been plotted as a function of the overlap (Figure 4.39). It can be noticed that the total width decreases as the overlap increases, because the scans are more overlapped, so the total width will be smaller as shown in the schematic representation in Figure 4.40. Instead, the mean height increases almost linearly with the overlap because, if the overlap value is high, the heat accumulation is remarkable and this results in very high scan heights (Figure 4.40).

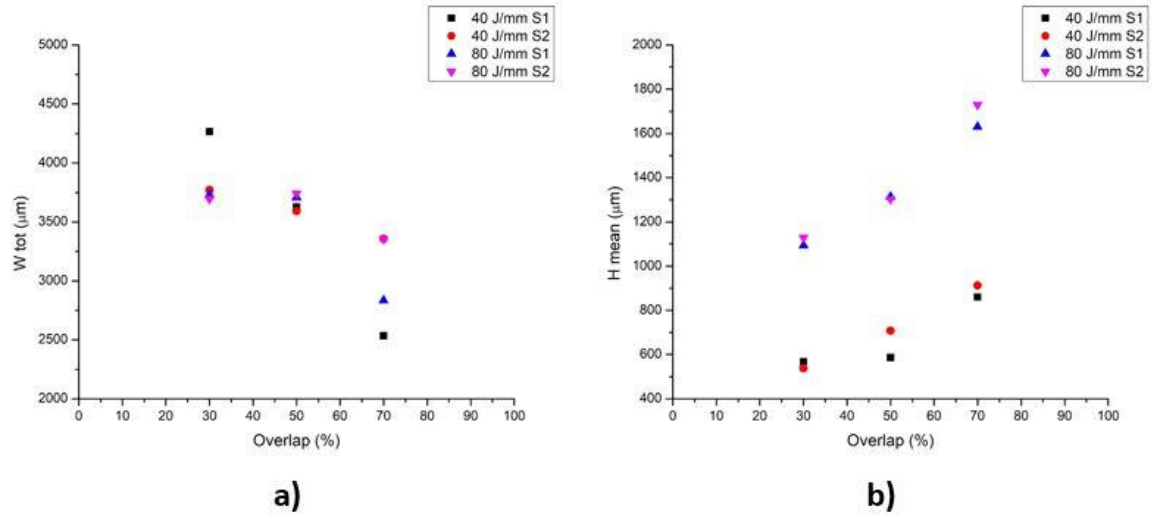

Figure 4.39: a) Total width and **b)** mean height as a function of the overlap.

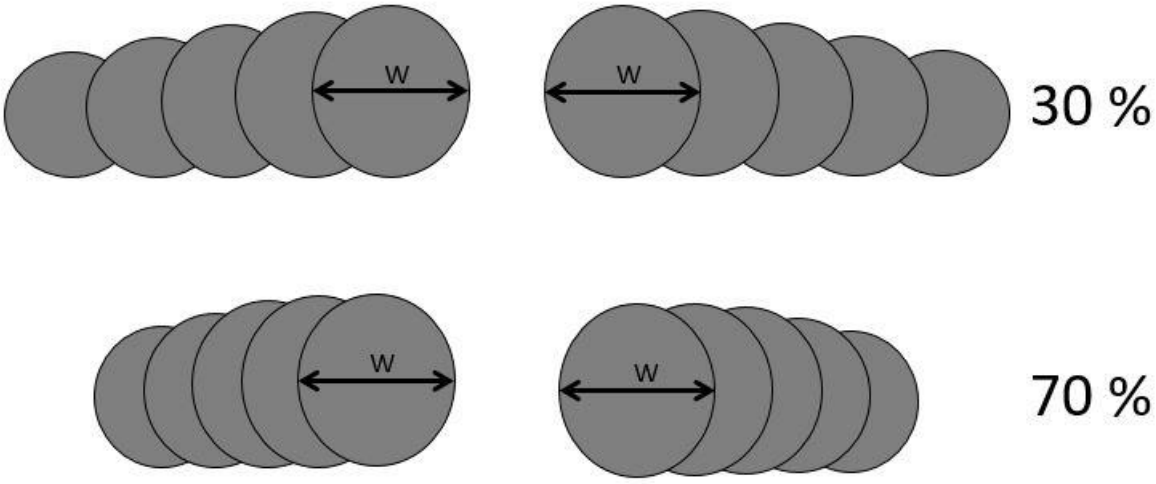

Figure 4.40: Schematic representation of overlap percentage (30 % and 70 %).

Considering high overlap values, the choice of a strategy has an important effect on scan height. In fact, as shown in the Figure 4.36, the use of the S1 strategy determines a higher external scan height than that of the most internal scan. This is because the S1 strategy starts from the internal circle and moves to the external one, so when the last scan is deposited this will go on the previous scan which is already in solidification phase, thus having a higher growth. This phenomenon is especially visible when high laser powers and high overlap values are used, as shown in Figure 4.41, while if low overlaps and low powers are used, this phenomenon is no longer visible.

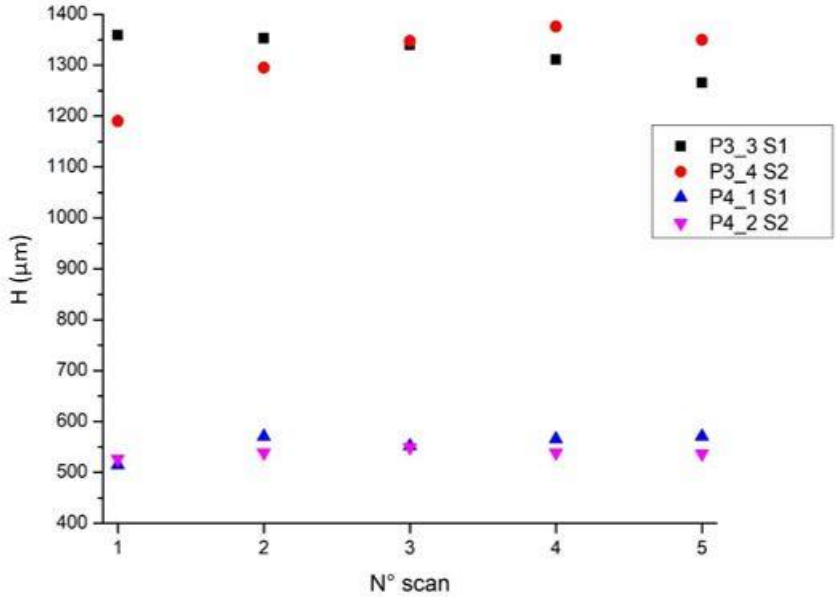

Figure 4.41: Scan height as a function of the scan number for samples P3_3 (600 W, 50 % Ov, S1), P3_4 (600 W, 50 % Ov, S2), P4_1 (300 W, 30 % Ov, S1), P4_2 (300 W, 30 % Ov, S2).

4.2.3 Micro-Vickers Hardness

The micro-Vickers hardness tests have been made on the cross section of the three samples P5_1, P5_3 and P5_4 belonging to the Baseplate 5 (whose building parameters are listed in Table 5). For each scan of the sample, a grid was created by making parallel and perpendicular indentations to the plate, ensuring a distance of 150 µm between one indentation and the other (Figure 4.42).

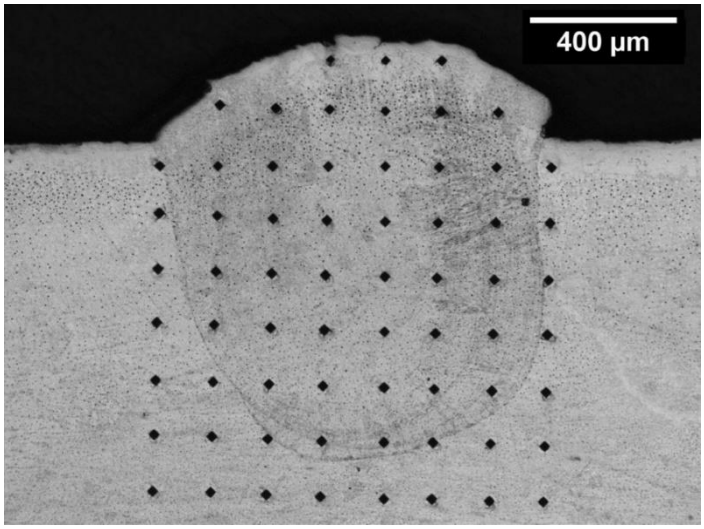

Figure 4.42: Grid of indentations.

Analyzing the first two samples P5_1 (300 W) and P5_3 (600 W), the effect of power on microhardness was evaluated, while analyzing the second sample P5_3 (S1, from the internal circle to the external one) with the third sample P5_4 (S2, from the external circle to the internal one) the analysis focused on the effect of the strategy. The results of the micro-Vickers hardness for the three samples and the resulting maps are given in Figure 4.43.

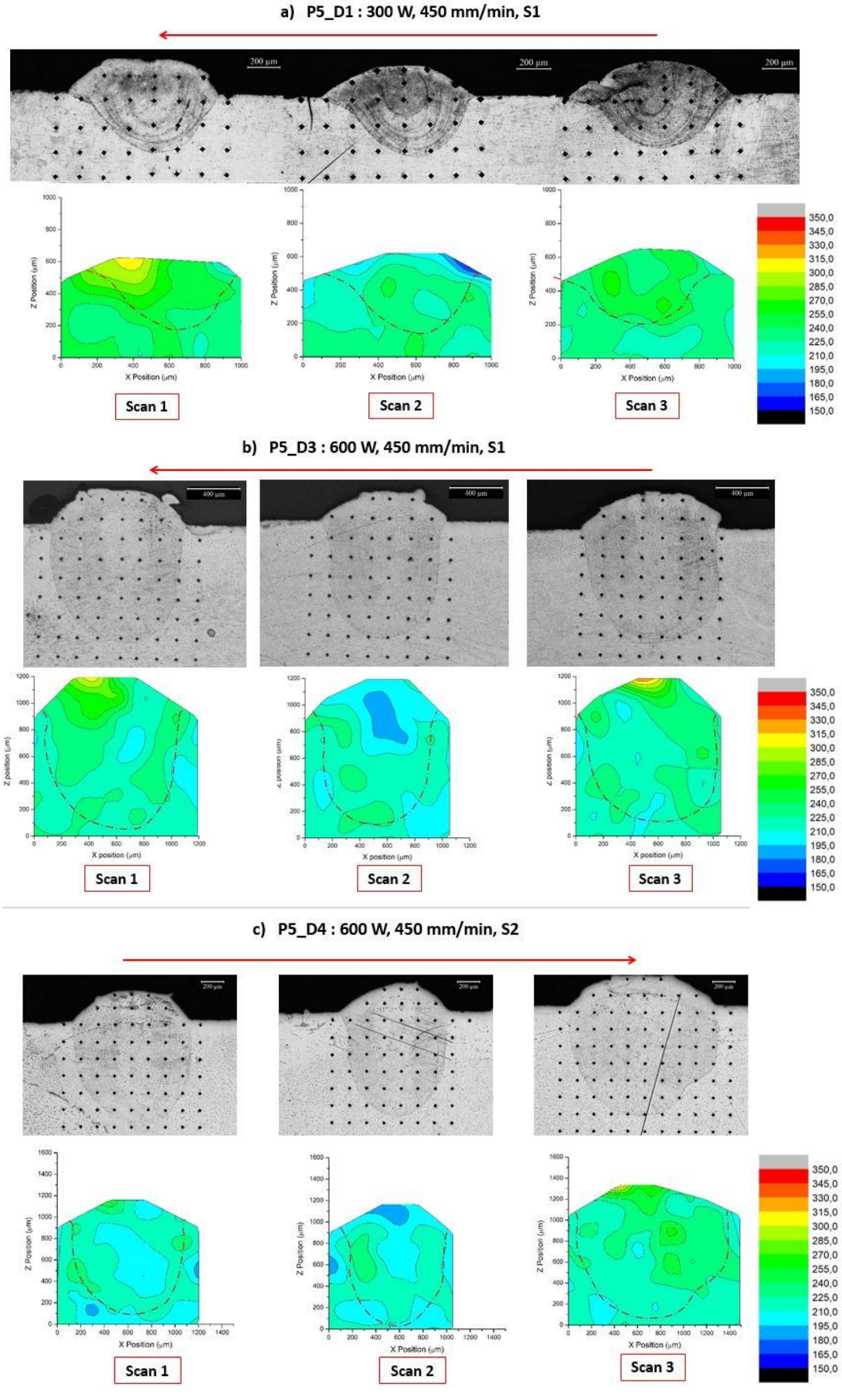

Figure 4.43: Grid of indentations and micro-Vickers hardness maps for sample **a)** P5_1, **b)** P5_3 and **c)** P5_4.

The result of micro-Vickers hardness obtained for the melt pools are little higher compared to the micro-hardness of the 316L baseplate. As shown in Figure 4.43, the micro-hardness is almost homogeneous throughout the melt pool to the 316L baseplate. As it gets closer to the centre of the melt pool, the micro-hardness slightly increases.

One thing in common for all three cases is that the external scan has a higher micro-hardness: in fact, it cools faster because it has a larger surface area, it is the fastest to solidify and at the end of the process has a finer structure that confers a higher hardness.

As shown in Figure 4.43, by increasing the laser power and focusing on the melt pool area, the sample P5_3 built with a power of 600 W has a lower hardness in all scans than that of the P5_1 sample built with a power of 300 W. This is due to the fact that if laser power increases, the melt pool solidifies more slowly and therefore assumes a coarse microstructure (as noted in Section 4.2.1 for the DAS calculation), that is a lower hardness than that given by a fine microstructure typical of the P5_1 sample that has a faster cooling rate.

As far as the effect of the strategy is concerned, using the S1 strategy the difference in the hardness of the first and third scan with the second is more visible than the case when the S2 strategy is used. In fact, when the S1 strategy is used, the first and third scans have a higher hardness in the melt pool area than the second scan, while using the S2 strategy the scans seem to have about the same average hardness value. Using S1 strategy, the first stored scan is the internal one, that in fact has a high hardness in the melt pool area; but also the external scan has high hardness because even if it is deposited last, and therefore it is affected by the heat accumulation due to the previous scans, it may be able to exchange more easily heat with the environment and then solidify rapidly and have a high hardness.

Another thing that can be noted is that in the case of sample built with a laser power of 300 W (P5_1), the baseplate and the melt pool have a higher hardness (green colour) than P5_3 and P5_4. Probably this is due to the fact that in sample P5_1 there is a wider heat affected zone (HAZ) than the case in which samples are built with a laser power of 600 W, but this phenomenon has to be analysed and investigated more.

4.2.4 Nanoindenter

Nanoindentation measurement was carried out on the cross section of the sample P5_2 of the Baseplate 5 (whose building parameters are listed in Table 5) in four different areas: the first measure was made at the top of the melt pool, the second on the left side of the melt pool boundary, the third on the right side and the fourth at the bottom of the melt pool (Figure 4.44).

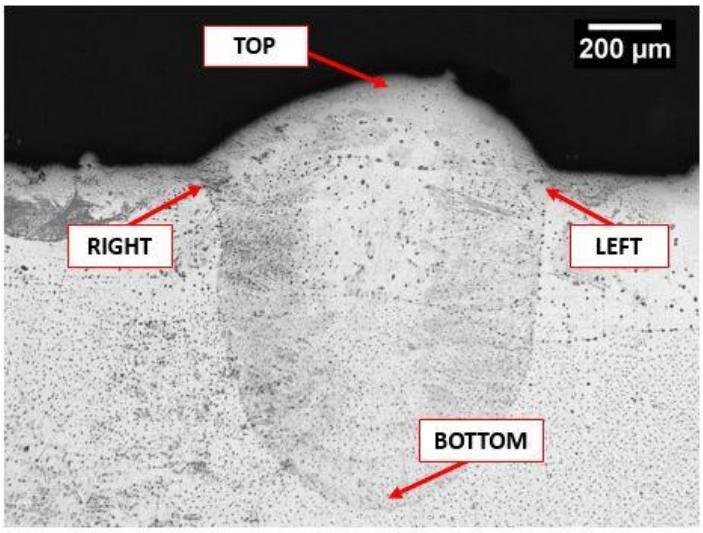

Figure 4.44: Four different areas where nanoindentation measurements were carried out.

The nanoindentation maps shown in Figure 4.45 confirm that the hardness is homogeneous also at a nanometric level within the melt pool. In particular, the top of the scan has a higher hardness because it cools faster having a larger surface area. Previous studies suggested in fact that the upper part of the scan is the fastest region of the melt pool to solidify and that at the end of the DED process it has a finer structure that confers a higher hardness. It is important to note that at the edges of the scan there are isolated areas with low hardness. However, it is necessary to investigate the effect of the strategy and the process parameters also in the massive baseplate, because probably the effect of the strategy on hardness is not visible in the first layer, but after a number of scans it could become.

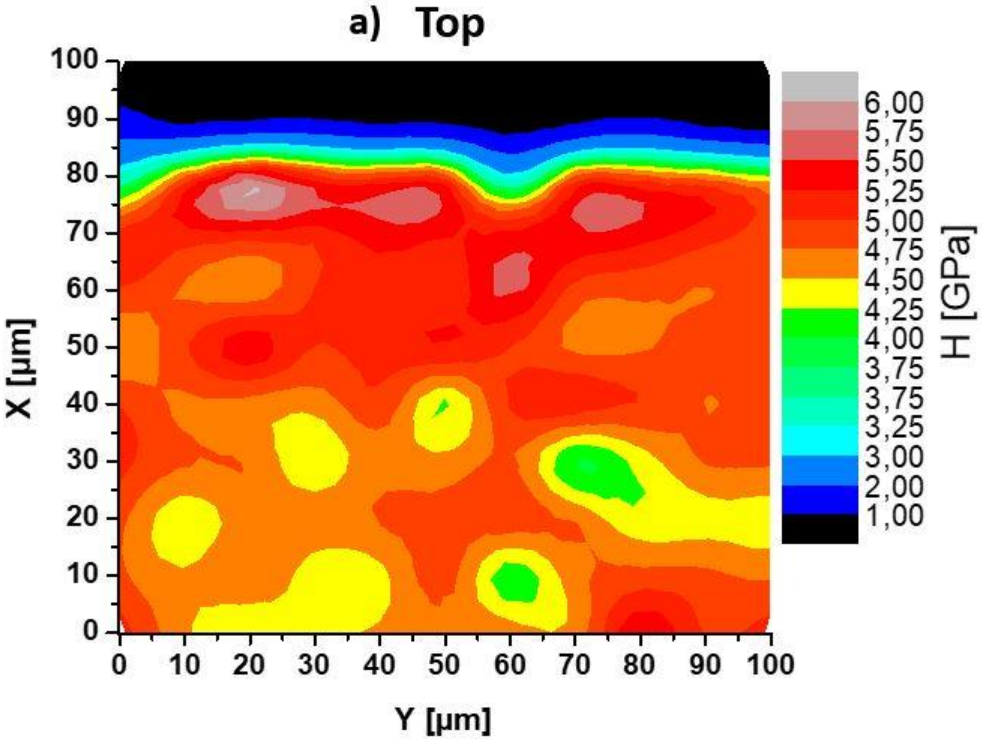

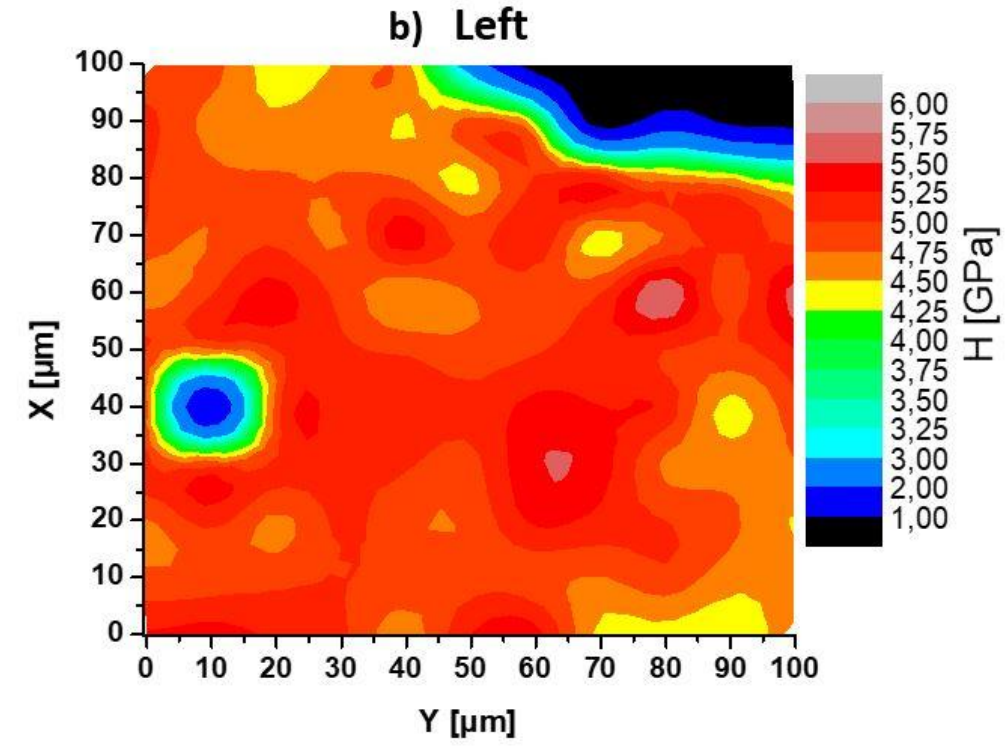
b) Left
X [µm]
Y [µm]
H [GPa]
6,00
5,75
5,50
5,25
5,00
4,75
4,50
4,25
4,00
3,75
3,50
3,25
3,00
2,00
1,00

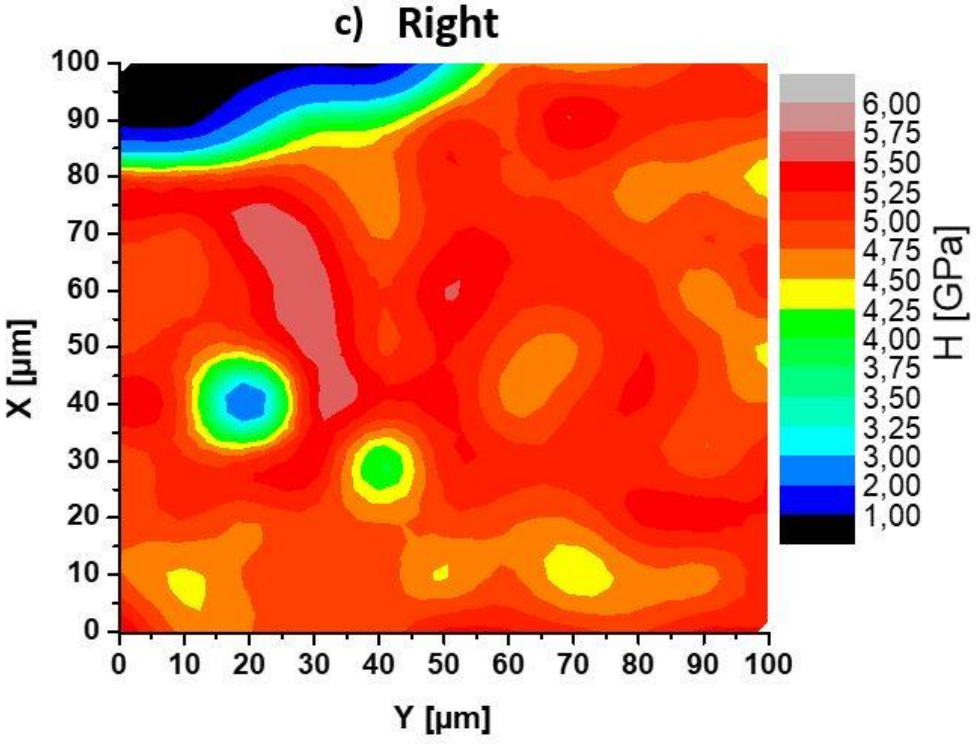
c) Right
X [µm]
Y [µm]
H [GPa]
6,00
5,75
5,50
5,25
5,00
4,75
4,50
4,25
4,00
3,75
3,50
3,25
3,00
2,00
1,00

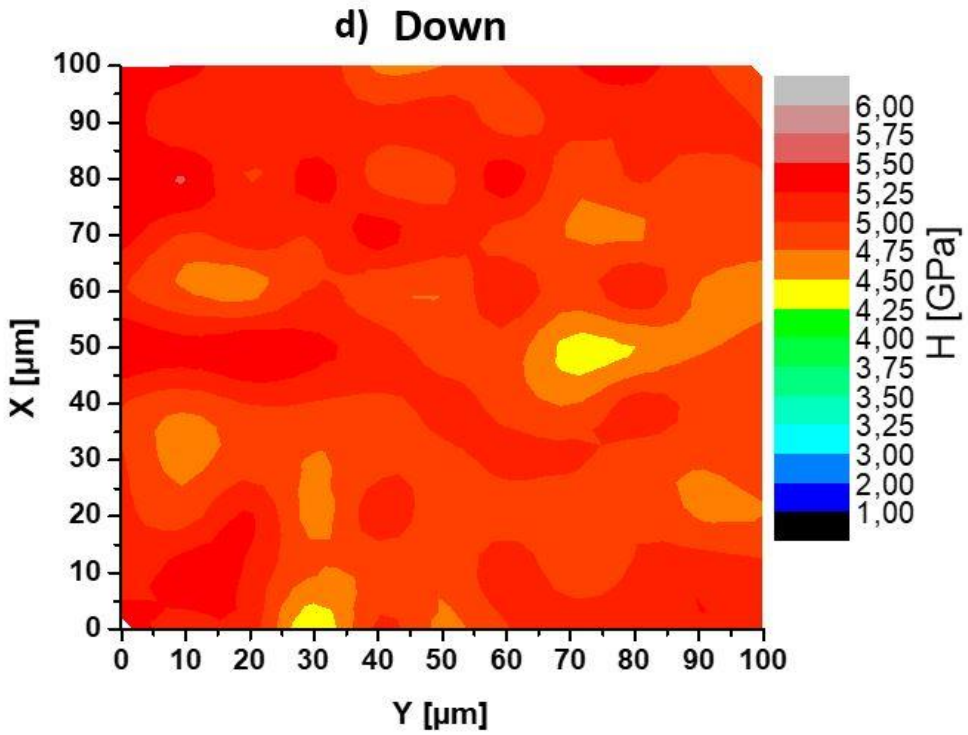

Figure 4.45: Nanoindentation maps of the **a)** top region, **b)** left side, **c)** right side and **d)** bottom region of the melt pool.

5. Conclusions

In this work, the effect of DED process parameters on the microstructural and geometrical features of the AISI 316L stainless steel scans was investigated. The analyzes were carried out tackling two different aspects of the process: the effect of the DED process both on powders and on the samples.

As far as the powders are concerned, the main goal was to determine if the 316L powders that have been introduced into a DED cycle could be effectively re-used, as the powder efficiency of the DED process is rather low (at max 25% working at high laser power) For this reason the possibility to reuse the powders is particularly appealing from an industrial point of view. On the base of the analyses carried out on the new powders and the ones used in a single DED cycle, it has been argued that the used powders have a more irregular shape, larger average dimensions and higher porosity level. Moreover, the average hardness of the powders that have undergone a DED cycle is lower than that of new powders of about 15%. From a microstructural point of view, XRD measurements demonstrated that the used powders is characterized by the presence of a new ferritic phase, not present in the original powders, but generally speaking the microstructure in both powders remains fine and homogeneous. From this point of view it is important to point out that X-rays have a detection limit of 5 %, so it is possible that ferrite is present also in the new powders. However, it can be certainly stated that the ferrite amount in new powders is lower than that in the used powders. The analyses by optical microscopy showed also that the used powder batch contains particles that are more prone to be etched than others. This aspect needs to be further addressed but it is a clue of the fact that used powders are less microstructurally homogeneous than new ones and may be therefore characterized by a different melting behaviour. This aspect needs further investigations in order to understand if this powder can be reliably re-used for following DED cycles, after having sieved the particles with the sizes acceptable for the process. Another aspect that has to be further investigated is the exact nature of the sub-micrometric features enriched in Si, O and Mn present mainly in the used powder but also in the DED samples. In particular it is necessary to understand the cause of their formation and whether they are distributed randomly or have sites that are preferred for their origin.

Now passing to the sample analysis, despite the fact that the samples have been built with two different geometries and process parameters, all the samples have the same microstructure within the melt pool. In particular, the top region of the melt pool has a fine structure as a consequence of the high cooling rate there applied, while the centre area has a coarser structure and the bottom of the melt pool sees columnar structures growth. Even in the samples, especially in the areas near the boundary of the melt pool, the ferritic phase was observed between interdendritic spaces and also the sub-micrometric features rich in O, Si and Mn were found analysing the cross section of the samples. Both these results were confirmed by several studies on AISI 316L obtained by AM that observed the same microstructural features in the melt pool.

Another aspect that was addressed within this work is the evaluation of the effect of process parameters and the scanning strategy on the microstructure and the geometry of melt pools. As far as the microstructure is concerned, it has been noted that increased laser power leads to an increase in DAS, thus a coarser dendritic structure is formed as a consequence of the high amount of generated heat that reduces the cooling rate and delays the solidification process. Instead, choosing a strategy rather than the other seems not to affect the dendritic structure. Now moving to the melt pool analysis, both the geometries of the samples, spirals

and circles were investigated. With regard to circles, central scans have a greater width than external ones due to a higher heat accumulation, regardless of the type of strategy is used. On the contrary, the choice of strategy affects the height of the scans that are higher when using the S2 strategy, probably because the heat is mainly concentrated inside the circle, and this leads to a higher heat accumulation. The increase in power leads to deeper and therefore higher melt pools, but the growth is the only magnitude that is always constant in all samples. Therefore, if the goal is to obtain scans with a higher growth value, it does not make sense to act on laser power or strategy, since acting on these two parameters affects only the depth and height of the scans.

As far as the spirals are concerned, the attention has been paid to the study of the effect of the tracks overlap. When low overlap values are selected as building parameters, the comparison of the overlapping values obtained with S1 and S2 scanning strategies shows that S2 strategy provides greater overlap when high LED parameters are used. In addition, when high laser powers are used, the overlap is greater than the nominal designed one because high laser powers lead to larger and deeper melt pools, thus to greater overlap values. For this reason, lower laser power values ensure the overlap percentage established at the design stage. Looking at the effect of process parameters on height and width, the total width decreases as the overlap increases, because the scans are more overlapped, so the total width will be smaller. Instead, the average height increases almost linearly with the overlap, because if the overlap value is high, the heat accumulation is remarkable and this results in very high scan heights. Considering the height of the scans, the change of strategy affects them because, depending on the direction of the deposition (from internal circle to external one (S1) or from the external circle to the internal one (S2)), the last scan has a higher height referring to the baseplate line, thus giving the sample a characteristic geometry depending on that the S1 or S2 strategy is used. This phenomenon is especially visible when high laser powers and high overlap values are used. Therefore, by comparing the results of both geometries, it can be said that the strategy has a limited influence on the size of the melt pool, while the variation of the laser power affects both the geometric magnitudes and, in the case of the spirals, also the value of the overlap has a definite effect on the shape of the scans. One aspect that would be interesting to further investigate is the effect of the variation of the scanning speed and feeding rate on the geometry of the melt pools, as in this work these two parameters had a constant value for all samples.

Finally, from a mechanical point of view, the hardness of the scans was evaluated for several samples with geometry of concentric circles both at the micro- and at the nano-level. In both cases, it has been noted that the hardness is almost homogeneous from the melt pool to the 316L baseplate. As it gets closer to the top / centre of the melt pool, the micro-hardness slightly increases because this region is that characterized by the higher solidification rate thus achieving the finest grains structure. By increasing the laser power and focusing on the melt pool area, the sample built with a higher power have a lower hardness in all scans than that of the samples built with a lower power. This is due to the fact that if the laser power increases, the melt pool solidifies more slowly and therefore assumes a coarser microstructure. As far as the impact of the strategy is concerned, using the S1 strategy, the difference in the hardness of the first and third scans with the second is more evident than in the case where S2 strategy is applied. Using S1 strategy, the first stored scan is the internal one, which in fact has a high hardness in the melt pool area; but also the external scan has high hardness because even if it is deposited last, and therefore it is affected by the heat accumulation due to the previous scans, it may be able to exchange more easily heat with the environment and then to solidify rapidly and to achieve a high hardness. One aspect that needs to be further investigated is the reason

why the baseplate in samples constructed with lower powers has a higher hardness than that of samples built with higher powers as this probably to be related to the presence of a heat affected zone (HAZ) surrounding the manufactured track.

6. Bibliography

[1] M. Ziętala *et al.*, "The microstructure, mechanical properties and corrosion resistance of 316 L stainless steel fabricated using laser engineered net shaping," *Mater. Sci. Eng. A*, vol. 677, pp. 1–10, 2016.

[2] N. Suutala and T. Takalo, "Ferritic-Austenitic Solidification Mode in Austenitic Stainless Steel Welds," vol. l, no. May, pp. 717–725, 1980.

[3] C. Pauzon, E. Hryha, P. Forêt, and L. Nyborg, "Effect of Argon and Nitrogen Atmospheres on the Properties of the As-Built 316L Stainless Steel Components by Laser Sintering," pp. 2–8.

[4] Y. Rong, G. Zhang, and Y. Huang, "Study on deformation and residual stress of laser welding 316L T-joint using 3D/shell finite element analysis and experiment verification," *Int. J. Adv. Manuf. Technol.*, vol. 89, no. 5–8, pp. 2077–2085, 2017.

[5] Y. Rong, Y. Huang, G. Zhang, G. Mi, and W. Shao, "Laser beam welding of 316L T-joint: microstructure, microhardness, distortion, and residual stress," *Int. J. Adv. Manuf. Technol.*, vol. 90, no. 5–8, pp. 2263–2270, 2017.

[6] N. Shamsaei, A. Yadollahi, L. Bian, and S. M. Thompson, "An overview of Direct Laser Deposition for additive manufacturing; Part II: Mechanical behavior, process parameter optimization and control," *Addit. Manuf.*, vol. 8, pp. 12–35, 2015.

[7] Z. Sun, X. Tan, S. B. Tor, and W. Y. Yeong, "Selective laser melting of stainless steel 316L with low porosity and high build rates," *Mater. Des.*, vol. 126, p. 359, 2017.

[8] S. M. Thompson, L. Bian, N. Shamsaei, and A. Yadollahi, "An overview of Direct Laser Deposition for additive manufacturing; Part I: Transport phenomena, modeling and diagnostics," *Addit. Manuf.*, vol. 8, pp. 36–62, 2015.

[9] A. Yadollahi, N. Shamsaei, S. M. Thompson, and D. W. Seely, "Effects of process time interval and heat treatment on the mechanical and microstructural properties of direct laser deposited 316L stainless steel," *Mater. Sci. Eng. A*, vol. 644, pp. 171–183, 2015.

[10] X. He and J. Mazumder, "Transport phenomena during direct metal deposition," *J. Appl. Phys.*, vol. 101, no. 5, 2007.

[11] F.-J. Kahlen and A. Kar, "Tensile Strengths for Laser-Fabricated Parts and Similarity Parameters for Rapid Manufacturing," *J. Manuf. Sci. Eng.*, vol. 123, no. 1, p. 38, 2001.

[12] L. Peng *et al.*, "Direct laser fabrication of nickel alloy samples," *Int. J. Mach. Tools Manuf.*, vol. 45, no. 11, pp. 1288–1294, 2005.

[13] U. de Oliveira, V. Ocelík, and J. T. M. De Hosson, "Analysis of coaxial laser cladding processing conditions," *Surf. Coatings Technol.*, vol. 197, no. 2–3, pp. 127–136, 2005.

[14] L. Wang and S. Felicelli, "Analysis of thermal phenomena in LENS™ deposition," *Mater. Sci. Eng. A*, vol. 435–436, pp. 625–631, 2006.

[15] M. Griffith, M. Schlienger, and L. Harwell, "Thermal behavior in the LENS process," *No. SAND--98-1850C; CONF-980826--. Sandia Natl. Labs., Albuquerque, NM (United States)*, 1998.

[16] L. Wang, S. D. Felicelli, and J. E. Craig, "Experimental and Numerical Study of the LENS Rapid Fabrication Process," *J. Manuf. Sci. Eng.*, vol. 131, no. 4, p. 41019, 2009.

[17] B. Zheng, Y. Zhou, J. E. Smugeresky, J. M. Schoenung, and E. J. Lavernia, "Thermal behavior and microstructural evolution during laser deposition with laser-engineered net shaping: Part I. Numerical calculations," *Metall. Mater. Trans. A Phys. Metall. Mater. Sci.*, vol. 39, no. 9, pp.

2228–2236, 2008.

[18] C. Selcuk, "Laser metal deposition for powder metallurgy parts," *Powder Metall.*, vol. 54, no. 2, pp. 94–99, 2011.

[19] H. Yin and S. D. Felicelli, "Dendrite growth simulation during solidification in the LENS process," *Acta Mater.*, vol. 58, no. 4, pp. 1455–1465, 2010.

[20] W. Liu and J. N. Dupont, "In-situ reactive processing of nickel aluminides by laser-engineered net shaping," *Metall. Mater. Trans. A*, vol. 34, no. 11, pp. 2633–2641, 2003.

[21] Y. Li, H. Yang, X. Lin, W. Huang, J. Li, and Y. Zhou, "The influences of processing parameters on forming characterizations during laser rapid forming," *Mater. Sci. Eng. A*, vol. 360, no. 1–2, pp. 18–25, 2003.

[22] J. Yu *et al.*, "Influence of laser deposition patterns on part distortion, interior quality and mechanical properties by laser solid forming (LSF)," *Mater. Sci. Eng. A*, vol. 528, no. 3, pp. 1094–1104, 2011.

[23] A. H. Nickel, D. M. Barnett, and F. B. Prinz, "Thermal stresses and deposition patterns in layered manufacturing," *Mater. Sci. Eng. A*, vol. 317, no. 1–2, pp. 59–64, 2001.

[24] A. Vasinonta, J. L. Beuth, and M. Griffith, "Process Maps for Predicting Residual Stress and Melt Pool Size in the Laser-Based Fabrication of Thin-Walled Structures," *J. Manuf. Sci. Eng.*, vol. 129, no. 1, p. 101, 2007.

[25] Y. M. Wang *et al.*, "Additively manufactured hierarchical stainless steels with high strength and ductility," *Nat. Mater.*, no. October, 2017.

[26] J. D. Majumdar, A. Pinkerton, Z. Liu, I. Manna, and L. Li, "Microstructure characterisation and process optimization of laser assisted rapid fabrication of 316L stainless steel," *Appl. Surf. Sci.*, vol. 247, no. 1–4, pp. 320–327, 2005.

[27] A. J. Pinkerton and L. Li, "An investigation of the effect of pulse frequency in laser multiple-layer cladding of stainless steel," *Appl. Surf. Sci.*, vol. 208–209, no. 1, pp. 405–410, 2003.

[28] T. M. Yue, J. K. Yu, and H. C. Man, "The effect of excimer laser surface treatment on pitting corrosion resistance of 316LS stainless steel," *Surf. Coatings Technol.*, vol. 137, no. 1, pp. 65–71, 2001.

[29] PrimaPower, "Brochure Laserdyne 430."

[30] K. Zhang, S. Wang, W. Liu, and X. Shang, "Characterization of stainless steel parts by Laser Metal Deposition Shaping," *Mater. Des.*, vol. 55, pp. 104–119, 2014.

Acknowledgement

The author would like to acknowledge the European research project belonging Horizon 2020 research and innovation programme Borealis—the 3A energy class Flexible Machine for the new Additive and Subtractive Manufacturing on next generation of complex 3D metal parts.

Ringraziamenti

Giunta al termine di questo percorso, vorrei ringraziare il Professore Daniele Ugues e la Professoressa Mariangela Lombardi per la loro disponibilità e per avermi permesso di lavorare su un argomento così interessante come l'Additive Manufacturing per materiali metallici.

Ringrazio Alberta. Sei una persona meravigliosa, oltre che una professionista eccezionale. Grazie per l'allegria e la grinta che mi hai trasmesso ogni giorno e che mi ha permesso di concludere al meglio questo percorso.

Ringrazio mio padre Alessandro, mia madre Giulia e mia sorella Ilaria. Siete e sarete sempre il motivo per il quale ogni giorno mi sveglio per cercare di fare qualcosa di buono e di giusto. Spero di avervi reso orgogliosi di me. Vi amo immensamente.

Ringrazio i miei bellissimi nonni per la saggezza, il calore e l'amore che mi donano in ogni telefonata e in ogni abbraccio una volta tornata a casa.

Ringrazio Valerio, un'anima pura che ho avuto la fortuna di incontrare, di amare e di rendere mia. Grazie per l'amore, la comprensione e il sostegno che mi regali ogni giorno. Grazie per aver scelto di guardare insieme a me verso lo stesso obiettivo. Questo è un piccolo passo per raggiungerlo. Sei la mia forza e la mia debolezza più bella.

Ringrazio Serena, non solo mia cugina ma anche mia sorella. Grazie per avermi donato il tifo che ogni studente sogna di avere e per essere, ogni giorno, la "medicina" ad ogni mia tristezza.

Ringrazio Marinetta. Non trovo le parole per esprimere quanto ti sono riconoscente. Sei stata la mia ancora in passato, lo sei oggi e, spero tanto, lo sarai in futuro. Tu sei l'essenziale.

Ringrazio Verdiana, Erika e Valentina. Grazie per avermi dato la possibilità di far parte di questo quartetto meraviglioso che mi regala ogni giorno tanti sorrisi e protezione. Siete speciali.

Ringrazio Gloria e Ilaria, per essere sempre il mio rifugio sicuro ogni volta che torno a casa. Siete così diverse ma così complementari che è sempre una gioia ritrovarvi e stringervi.

Ringrazio i miei coinquilini Cristina, Federica, Sergio, Michela, Lucrezia e Cecilia. Grazie per avermi fatto sentire a casa, quando la "vera" casa era lontana. Siete delle persone fantastiche.

Ringrazio Elisa, Erica e Luca, i miei amici e compagni di viaggio "materialisti. Grazie per le mille risate, confidenze, chiacchierate e pranzi condivisi insieme. Ognuno di voi è stato un colore che ha sostituito il grigio delle "giornate politecniche". Vi voglio bene e…W la fiotta!

Ringrazio la mia grande famiglia torinese. In particolare Leonardo, Piero, Matteo, Ornella, Domenico, Nazareno, Marco, Simone, Simona e Vincenzo. Mi sento così fortunata per avervi incontrato, conosciuto e vissuto. Avrete sempre un posto speciale nel mio cuore.

Infine, ringrazio me stessa. Ringrazio la mia tenacità, la mia forza di volontà, la mia fragilità e la mia voglia di imparare che mi hanno permesso di completare questo percorso meraviglioso. Soprattutto dai miei difetti più che dai miei pregi, ho imparato a sfidarmi ogni giorno e a credere sempre di più in me stessa.